Thèse n° 9679

Mass transport of water vapor and ions from Å-scale graphene nanopores

Présentée le 21 juillet 2022

Faculté des sciences de base
Chaire Gaznat en procédés de séparation avancés
Programme doctoral en chimie et génie chimique

pour l'obtention du grade de Docteur ès Sciences

par

Wan-Chi LEE

Acceptée sur proposition du jury

Prof. M. K. Nazeeruddin, président du jury
Prof. K. V. Agrawal, directeur de thèse
Prof. C.-J. Shih, rapporteur
Prof. J. Zhao, rapporteuse
Prof. K. Sivula, rapporteur

École
polytechnique
fédérale
de Lausanne

2022

Was mich nicht umbringt, macht mich stärker
-Friedrich Nietzsche

Acknowledgment

My supervisor, Prof. Kumar Varoon Agrawal, I would like to thank for his guidance and support throughout my doctoral career. He brought me to the world of graphene nanopores and graphene membranes and made me realize graphene is the best material ever in the world. His enthusiasm, passion, and attitude for science are admirable. I learned a lot from his way of approaching things and how he copes with things efficiently and effectively. It is Kumar and his lab that makes me an independent researcher.

This thesis involved many collaborators, and first, I would like to thank Prof. Guangwei He and Dr. Shiqi Huang, who helped me to start in LAS, and I learned most of my experimental skills about graphene from them. I would also like to thank Prof. K. Ganapathy Ayappa and Anshaj Ronghe from Indian Institute of Science, Bangalore, for their tremendous support in atomic simulation and our collaboration. Dr. Kangning Zhao is another person I would like to show my gratitude for all the discussions we had and the hard time we suffered together during the ion separation project.

I enjoyed doing research in LAS because we have the best colleagues ever. I would like to thank Dr. Shiqi Huang, Dr. Mostapha Dakhchoune, Dr. Luis Francisco Villalobos, Prof. Deepu J Babu, Prof. Guangwei He, and all other LAS members for those wonderful scientific discussions, although we were working on different materials and different projects. I always remember the gossip cakes and fun (insightful) conversations that we shared together, and the afterlab activities like board games, concerts and running.

I am grateful to several professors who gave me helpful advice in my career. Prof. Dun-Yen Kang and Prof. Chih-Jen Shih helped me a lot throughout my study in Switzerland. I appreciate Prof. Deepu J Babu's input on my career development. I did benefit a lot from their assistance. Also, I would like to express my gratitude to my jury members: Prof. Chih-Jen Shih, Prof. Jing Zhao, and Prof. Kevin Sivula.

Finally, I would like to thank my parents, my two elder brothers, and those friends outside science I met in Switzerland and Europe. Without your support, I could not complete this thesis.

Table of Content

Acknowledgment ii

Table of Content iii

List of Figures vi

List of Tables ix

Abstract x

Résumé xii

Chapter 1 Introduction 1

1.1 Hydrodynamics at the nanoscale: challenges and opportunities 1

1.2 Nanopores in single-layer graphene 3

- 1.2.1 Single-layer graphene 3
- 1.2.2 Graphene nanopores 4
  - 1.2.2.1 Bottom-up methods 5
  - 1.2.2.2 Top-down methods 5

1.3 Graphene nanopores for fluidic transport 8

- 1.3.1 Gas molecules 8
- 1.3.2 Water and organic solvents 10
- 1.3.3 Ionic species 12
- 1.3.4 Protons 14

1.4 Challenges and opportunities for graphene nanopores in studying mass transport at the nanoscale 15

1.5 Thesis outline 15

Chapter 2 Enhanced Water Evaporation From Å-scale Graphene Nanopores 17

Abstract 17

2.1 Introduction 18

2.2 Methods and materials 19

2.3 Results and discussion 24

    2.3.1 Fabrication and characterization of graphene nanopores 24
    2.3.2 Water vapor transport 30
    2.3.3 System details for molecular dynamics simulations 38
    2.3.4 Evaporation flux of water molecules........ 39
    2.3.5 Hydrogen bond analysis, rotational dynamics, and translational dynamics........ 41
    2.3.6 Potential of mean force and surface tension analysis........ 45

2.4 Conclusion 48

2.5 Appendix I........ 49

Chapter 3 Size-dependent Subcontinuum Ion Permeation Across Nanoporous Graphene Membranes .. 61

Abstract........ 61

3.1 Introduction........ 61

3.2 Methods and materials 63

3.3 Results and discussion 66

    3.3.1 Tailored graphene nanopores for selective ion transport........ 66
    3.3.2 Ion permeation across tailored graphene nanopores 70
    3.3.3 Adjustment of the molecular cutoff........ 75
    3.3.4 Modeling ion flux using continuum theory........ 76
    3.3.5 Mechanism of ion transport through graphene nanopores 79

3.4 Conclusion 82

Chapter 4 Centimeter-Scale Gas-Sieving Nanoporous Single-Layer Graphene Membrane........ 83

Abstract........ 83

4.1 Introduction........ 84

4.2. Methods and materials 85

4.3. Results and discussion 88

4.3.1 Fabrication of large-area graphene membrane 88
4.3.2 Crack-free centimeter-scale membranes 93
4.3.3 Centimeter-scale NSLG membranes for H_2/CO_2 and H_2/CH_4 separation 96
4.3.4 Analysis of the concentration of non-selective pores 99
4.3.5 Use of NPC-free MWNT layer to transfer graphene 102
4.4. Conclusion 103
4.5. Appendix I 104
Chapter 5 Summary and Perspectives 106
5.1 Summary 106
5.2 Perspectives 107
References 109
Curriculum Vitae 124

List of Figures

Chapter 1

Figure 1.1. Critical knowledge gaps in hydrodynamics at the nanoscale 2
Figure 1.2. Atomic structure of graphene and its synthesis methods 4
Figure 1.3. Graphene nanopores created using bottom-up methods. 6
Figure 1.4. Graphene nanopores created using top-down methods. 8
Figure 1.5. Gas transport across graphene nanopores 10
Figure 1.6. Water transport across graphene nanopores.. 12
Figure 1.7. Ion transport across graphene nanopores.. 14

Chapter 2

Figure 2.1. Raman characterization of O_2 plasma-treated nanoporous single-layer graphene (NSLG)... 24
Figure 2.2. XPS spectra of graphene samples. 26
Figure 2.3. Characterization of graphene nanopores used to probe water transport 27
Figure 2.4. Pore analysis by AC-HRTEM. 29
Figure 2.5. Pore size distribution analysis 30
Figure 2.6. Characterization of nanoporous graphene/support film. 31
Figure 2.7. Water vapor transport data of eight different nanoporous graphene samples made by 1, 2, and 3 s plasma 32
Figure 2.8. Characterization of HOPG/nanoporous graphene after evaporation. 35
Figure 2.9. The setup and raw data of water permeation tests. 34
Figure 2.10. Analysis of water evaporation rate, and H_2 flow rate per pore of different graphene films. 38
Figure 2.11. System details for MD simulations and evaporation flux from different FNPGs 40
Figure 2.12. HB analysis for the functional group (pore)–water (P–W) pair and water–water (W–W) pair along with rotational dynamics and translational dynamics of water molecules present in the ROI of different FNPGs 42
Figure 2.13. Interaction of water molecules with the functional groups and with other water molecules in the vicinity of the nanopore via HBs 43
Figure 2.14. Free energy calculations for evaporation of water molecules and surface tension at water-vapor interface for different FNPGs 46

Figure 2.15. Comparison of calculated water supply limit and the measured evaporation flux of all tested nanoporous graphene membranes at 22 °C.. 50
Figure 2.16. Different arrangements of H atoms and OH functional groups on the edge of type-1 nanopore to determine the FNPG with the lowest formation energy and the formation energies of optimized FNPGs with the arrangements of H atoms and OH functional groups on the edge of nanopore corresponding to the different configurations (A–J)... 51
Figure 2.17. Interaction potential between the carbon atom of the attractive wall and the oxygen atom of water molecule.. 53
Figure 2.18. System details and dimensions for simulation with FNPGs 54
Figure 2.19. Density profile of water molecules in the BLVI simulations.. 55
Figure 2.20. Cumulative number of evaporated water molecules 56

Chapter 3

Figure 3.1. Creation and characterization of graphene nanopores using a decoupled nucleation/expansion method... 68
Figure 3.2. STM analysis of graphene nanopores etched by CO_2. 69
Figure 3.3. Characterization of nanoporous graphene membranes used to study ion transport. 70
Figure 3.4. Setup for diffusion tests.. 71
Figure 3.5. Measurement of ion diffusion across graphene nanopores. 73
Figure 3.6. Ionic sieving in graphene nanopores and other materials. 76
Figure 3.7. Experimental energy barriers for K^+, Na^+, Li^+, and Mg^{2+}. 80

Chapter 4

Figure 4.1. Schematic of the fabrication of large-area NSLG membranes using the composite NPC/MWNT film as a reinforcing layer.. 88
Figure 4.2. SEM images of the NPC film.. 89
Figure 4.3. SEM image of sintered tungsten support.. 90
Figure 4.4. Characterization of the centimeter-scale graphene membrane.. 90
Figure 4.5. Morphology of the NSLG/NPC/MWNT film.. 92
Figure 4.6. Raman spectra of CVD graphene, NPC, MWNT, and graphene/NPC/MWNT films transferred on a Si/SiO_2 wafer using a 532 nm excitation source... 93
Figure 4.7. Characterization of the centimeter-scale reinforced membranes prepared using the as-synthesized SLG hosting intrinsic vacancy defects.. 94

Figure 4.8. Raman analysis of graphene membrane. 95
Figure 4.9. Schematic of the setup for gas permeation tests. 95
Figure 4.10. Characterization of the centimeter-scale reinforced graphene membranes prepared using the ozone-etched graphene 97
Figure 4.11. Raman analysis of ozone-etched graphene membrane.. 98
Figure 4.12. H_2 and CH_4 permeance of M5 as a function of temperature. 98
Figure 4.13. Modeling gas transport behavior in a graphene nanopore 101
Figure 4.14. Characterization of NSLG/ MWNT film.. 103

List of Tables

Chapter 2

Table 2.1. BLVI reported in the literatur and in this study. 36

Table 2.2. Effective pore diameter, d_{eff} and effective pore area, A_{eff} of each functionalizednanopore of the FNPGs shown in Figure 2.11a. 52

Table 2.3. Details for evaluation of evaporation flux, j. 57

Table 2.4. Free energy difference (kJ/mol) between different regions. 59

Table 2.5. Surface tension values at water-vapor interface for different FNPG systems andBLVI. 60

Chapter 3

Table 3.1. Experimental hydration free energy and hydrated diameter of different ions. 79

Chapter 4

Table 4.1. Gas permeation data of M2 at 25 and 100 °C, single-component measurement. 104

Table 4.2. Gas permeation data of M5 at 25 and 100 °C, single-component measurement. 104

Table 4.3. Comparison of the single-component versus mixture permeation data from M2. 104

Table 4.4. Comparison of the single-component versus mixture permeation data from M5. 104

Table 4.5. Comparison of the single-component versus mixture permeation data from M5. 104

Table 4.6. Comparison of gas separation performance between our work and other CVD graphene-based membranes. 105

Table 4.7. Permeance and selectivity of MWNT film and graphene membrane prepared by using MWNT reinforcement (without NPC film) at a feed pressure 1.5 bar at 25 °C. 105

Abstract

Hydrodynamics at the nanoscale involves both fundamental study and application of fluid and mass transport phenomena in nanometer-sized confinements. Nanopores in single-layer graphene can be highly attractive for exploring the molecular transport of gas and water molecules and hydrated ions at the ultimate scales of pore size and pore length. However, the experimental data is limited, and the state-of-the-art artificial nanopores still underperform compared to biological channels in cellular membranes.

This dissertation focuses on developing ultimate graphene nanopore devices to study mass transport phenomena under controlled spatial confinement. We first investigated the kinetics of liquid–vapor transport from nanoscale confinements which is attractive for novel evaporation and separation applications; however, it is not explored at the ultimate confinement limit, i.e., at the atomic-thick and Å-scale nanopore placed at the liquid–vapor interface. We show that the evaporation flux from such nanopores increases with decreasing pore size by up to one order of magnitude relative to the bare liquid–vapor interface. Molecular dynamics simulations reveal that oxygen-functionalized nanopores render rapid rotational and translational dynamics to water molecules by reducing and shortening the lifetime of water–water hydrogen bonds.

Graphene nanopores also enable the study of ion transport across sub-nanometer-scale 2D confinements. We produce tailor-made nanopores approaching the size of hydrated ions by decoupling the pore nucleation and expansion. Monovalent metal ions are efficiently sieved from divalent ions, with K^+/Mg^{2+} selectivity up to 70 and Li^+/Mg^{2+} selectivity up to 50, corresponding to a sieving resolution of 1 Å. Mitigating the non-selective pore formation further enhance the ion-sieving performance, reaching K^+/Mg^{2+} selectivity up to 350 and Li^+/Mg^{2+} selectivity up to 260. The pore size and structure allow adjusting the diffusion of ions across the nanopores, suggesting that the sterically induced partial dehydration process may play an important role in the observed cation selectivities. These selectivities were realized from centimeter-scale suspended graphene membranes, prepared in crack-free fashion by using dual layer reinforcement strategy where the first layer is 200-nm-thick nanoporous carbon (NPC) film hosting 20 nm pores which ensures a conformal contact and reinforcement of the graphene film and the second (top) layer is Nafion.

Finally, a dual layer reinforcement is also demonstrated for preparing crack-free centimeter-scale gas separation membranes to utilize the full potential of graphene nanopores for energy-efficient applications.

The bottom layer of the composite film is NPC film while the top layer is made of a 500-nm thick multi-walled carbon nanotube (MWNT) film with a pore size ranging from 200 to 300 nm. The obtained selectivities from crack-free centimeter-scale graphene membranes for H_2/CH_4 and H_2/CO_2 are 11–23 and 5–8, respectively, which is significantly higher than the corresponding Knudsen selectivities.

Overall, this dissertation presents a graphene nanopore toolkit for studying fluid mechanics at the ultimate scales. The findings of enhanced water evaporation rate and ion selectivity using the nanopore platform could enrich our understanding of mass transport under extreme confinement and open new opportunities for a range of separation applications.

Keywords: graphene nanopores, water evaporation, evaporation kinetics, ion transport, membrane,

Résumé

L'hydrodynamique à l'échelle nanométrique implique à la fois l'étude fondamentale et l'application des phénomènes de transport de fluides et de masse dans des confinements de taille nanométrique. Les nanopores dans le graphène monocouche peuvent être très attractifs pour explorer le transport moléculaire des molécules de gaz et d'eau et des ions hydratés à des échelles nanométrique. Cependant, l'apport expérimental est limité, et les nanopores artificiels sont toujours moins performantes que les canaux biologiques des membranes cellulaires.

Cette thèse porte sur le développement de dispositifs nanométrique de nanopores de graphène pour étudier les phénomènes de transport de masse sous confinement spatial contrôlé. Nous avons d'abord étudié la cinétique du transport liquide–vapeur à partir de confinements à l'échelle nanométrique, un phénomène fondamentalement moins exploré mais attrayant pour de nouvelles applications d'évaporation et de séparation. Le flux d'évaporation à partir de nanopores à l'échelle de l'angström augmente avec la diminution de la taille des pores d'un ordre de grandeur par rapport à l'interface liquide–vapeur. Les simulations de dynamique moléculaire révèlent que les nanopores fonctionnalisés à l'oxygène confèrent une dynamique de rotation et de translation rapide aux molécules d'eau en réduisant et en raccourcissant la durée de vie des liaisons hydrogène eau–eau.

Les nanopores de graphène permettent également d'étudier le transport des ions à travers des confinements 2D à l'échelle sub-nanométrique. Nous produisons des nanopores sur mesure dont la taille est proche de celle des ions hydratés en découplant la nucléation et l'expansion des pores. Les ions métalliques monovalents sont efficacement tamisés par rapport aux ions divalents, avec une sélectivité K^+/Mg^{2+} allant jusqu'à 70 et une sélectivité Li^+/Mg^{2+} allant jusqu'à 50, correspondant à une résolution de tamisage moléculaire d'un an. L'atténuation de la formation de pores non sélectifs améliore encore les performances de tamisage des ions, atteignant une sélectivité K^+/Mg^{2+} jusqu'à 350 et une sélectivité Li^+/Mg^{2+} jusqu'à 260. La taille et la structure des pores permettent d'ajuster la diffusion des ions à travers les nanopores, ce qui suggère que le processus de déshydratation partielle induit stériquement peut jouer un rôle important dans les sélectivités de cations observées.

Enfin, nous proposons un procédé de fabrication de membranes de grande surface sans fissures afin d'utiliser tout le potentiel des nanopores de graphène pour des applications à haut rendement énergétique. Nous présentons une méthode pour renforcer mécaniquement le graphène nanoporeux à l'échelle centimétrique en utilisant un film de carbone composite à deux couches. La couche inférieure du film composite est composée d'un film de carbone nanoporeux (NPC) de 100 nm d'épaisseur, tandis que la couche supérieure était constituée d'un film de nanotubes de carbone multiparois (MWNT) de 500 nm d'épaisseur avec une taille de pores allant de 200 à 300 nm. Les sélectivités obtenues à partir de membranes de graphène à l'échelle centimétrique sans fissures pour H_2/CH_4 et H_2/CO_2 sont respectivement de 11–23 et 5–8, ce qui est nettement supérieur aux sélectivités de Knudsen correspondantes.

Dans l'ensemble, cette thèse présente une boîte à outils de nanopores de graphène pour étudier la mécanique des fluides à l'échelle nanométrique. Les résultats de l'amélioration du taux d'évaporation de l'eau et de la sélectivité des ions en utilisant la plateforme de nanopores pourraient enrichir notre compréhension du transport de masse sous confinement extrême et ouvrir de nouvelles opportunités pour une gamme d'applications de séparation.

Mots clés: graphène nanoporeux, évaporation de l'eau, cinétique d'évaporation, transport d'ions, membrane

Chapter 1 Introduction

1.1 Hydrodynamics at the nanoscale: challenges and opportunities

Hydrodynamics at the nanoscale involves both fundamental study and application of fluid and mass transport phenomena in nanometer-sized confinement, where they behave differently compared to their counterparts in the bulk phase. It is a powerful tool in a wide range of fields, such as thermodynamics, quantum physics [1], nanofluidics [2–4], and biophysics [5]. Hydrodynamics at the nanoscale has revived in the past few years, and recent experimental studies revealed that the classical continuum model fails to describe the behavior of water molecules and ionic fluids under extreme confinements [6,7]. These findings also suggest knowledge gaps of nanoscale hydrodynamics, which are classified into several subgroups [8], as shown in **Figure 1.1**. These knowledge gaps have raised a need for next-generation approaches to address and soundly understand those topics while providing opportunities for new technologies. Nowadays, the goal is to fabricate artificial nanochannels/nanopores that would reproduce the complexity of biological channels for understanding the fluid mechanics at the ultimate scales. Examples of such platforms include carbon nanotubes (CNTs) [9–11], graphene oxide (GO) laminates [12–14], solid-state nanopores [15,16], and nanochannels made from polymeric [17] or inorganic building blocks [18]. In a nutshell, CNTs, with their well-defined diameter and atomical smoothness, are used as model systems to study slip flow enhancement in hydrophobic confinements [10]. They are also used to study fluid phase transition under extreme confinements below 2 nm [11], which was also demonstrated in nanoporous silica [19]. GO laminates, on the other hand, were explored to investigate the correlated transport and the desolvation process between water/ions and the functional groups inside the nanochannels [20,21]. Further efforts are made to reveal the geometry-dependent kinetic evaporation under confinement using solid-state nanoconduits and nanopores [15,16]. In addition, nanopores in two-dimensional materials, such as molybdenum disulfide (MoS_2) [22,23], graphene, or hexagonal boron nitride (hBN) [2,24], were developed to understand the confinement-induced transport behavior of water, solvent molecules, or ions.

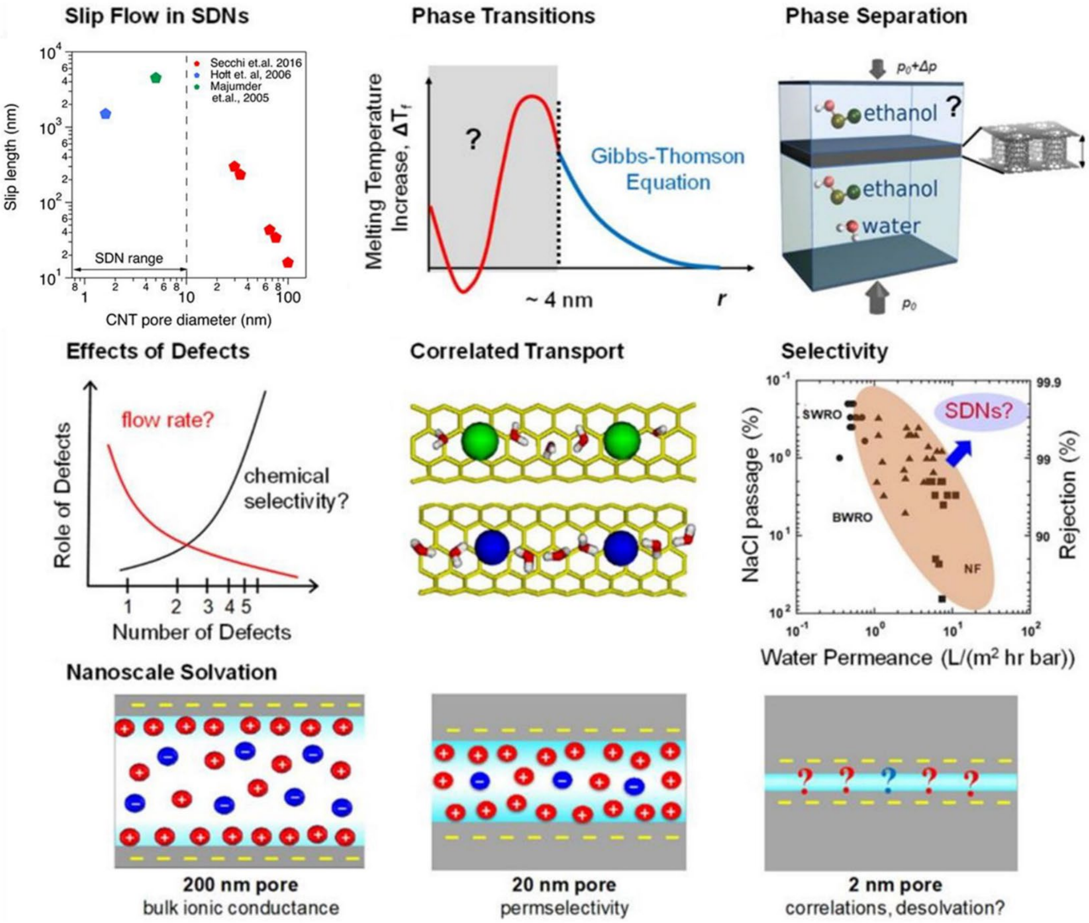
Slip Flow in SDNs
Secchi et.al. 2016
Holt et. al, 2006
Majumder et.al., 2005
Slip length (nm)
SDN range
CNT pore diameter (nm)
Phase Transitions
Melting Temperature Increase, ΔT_f
?
Gibbs-Thomson Equation
~ 4 nm
r
Phase Separation
p₀+Δp
ethanol
?
ethanol
water
p₀
Effects of Defects
flow rate?
chemical selectivity?
Role of Defects
Number of Defects
Correlated Transport
Selectivity
SWRO
BWRO
NF
SDNs?
NaCl passage (%)
Rejection (%)
Water Permeance (L/(m² hr bar))
Nanoscale Solvation
200 nm pore
bulk ionic conductance
20 nm pore
permselectivity
2 nm pore
correlations, desolvation?

Figure 1.1. Critical knowledge gaps in hydrodynamics at the nanoscale. Note: Seven topics in the study of fluid mechanics under confinement (< 10 nm) are not well-understood. They include 1) the slip length in nanopore diameter, 2) the phase behavior of fluids under confinement, 3) enhanced phase separation by nanoconfinement, 4) impact of defects at the nanoscale, 5) transport of ions and their interaction with confining cavity, 6) enhanced molecular and ionic selectivities, and 7) the solvation and desolvation in confinement. Adapted with permission from [8]. Copyright © 2019, American Chemical Society.

Nanoscale fluids have been intensively examined using atomic simulations; however, the experimental input is little due to the inherent difficulty of the nanoconfinement fabrication and analytical techniques to probe the ultrasmall systems. Indeed, it is challenging to precisely create a confining geometry with controlled sub-nanometer dimensions. The state-of-art micro- and nanofabrication enable solid-state nanopores and nanosteps down to a few nanometers but may result in a rough-etched morphology [25]. In addition, current experiment efforts using such techniques focus on nanostructures 20–100 nm in size, which cannot reveal the actual behavior of fluid to its limit, i.e., under confinement approaching the size of molecules. A prominent strategy to address these issues is to exploit novel two-dimensional materials, such as single-layer graphene, which provides atomic flatness and enhances nanopore characterization while avoiding structural complexity seen in other materials [26–28]. This thesis pursues employing graphene nanopores for investigating the water vaporization and ion transport under confinements approaching the size of a water molecule or a hydrated ion. The nanopore platform also enables probing a novel transport regime that allows separation and sensing applications.

1.2 Nanopores in single-layer graphene

1.2.1 Single-layer graphene

Since the first experimental discovery by Novoselov et al. [29], who were later awarded Nobel Prize in physics in 2010, graphene has attracted considerable attention as a "super material." Graphene comprises a single layer of carbon atoms arranged in a honeycomb lattice connected with sp^2 hybridization (**Figure 1.2a and b**). It is one-atom-thick (~3.4 Å), highly flexible, and shows extraordinary mechanical [30] and thermal stability[31,32]. The Young's modulus for single-layer graphene reaches 1 TPa [33], and single-layer graphene also shows a high thermal conductivity of 5000 W mK^{-1} t and can withstand temperatures up to 2600 K [34]. Furthermore, graphene is known as "semi-metal," neither semiconductor nor metal, and can have electron mobility as high as 2 $x10^5$ cm^2/Vs [35].

Different approaches to producing graphene were investigated after the demonstration of mechanical graphene exfoliation from graphite flakes using "scotch tape" [29]. Various routes for graphene production fall into two groups: the top-down approach and the bottom-up approach. Exfoliation is a typical top-down approach with several derivatives depending on the force/energy involved in the process, e.g., exfoliation by liquid-phase sonication [36,37], sticky tape, or electrochemistry (**Figure 1.2c**) [38]. The most significant advantage of top-down approaches is the synthesis of transfer-free graphene which facilitates the placement of target substrates. However, the resolution of configurational structures is often sacrificed in this case. On the other hand, growing single-layer graphene on catalytic metal substrates by chemical vapor deposition (CVD), a bottom-up approach, has attracted great attention because of its versatile potential to integrate into the well-established semiconductor industry. The first demonstration of CVD-grown single-layer polycrystalline graphene film which could be successfully transferred to another substrate was reported in 2009 by Ruoff's group [39] with CH_4 as the carbon source and copper (Cu) as the catalyst (**Figure 1.2d**). Nowadays, this method allows the synthesis of exclusive single-layer coverage (> 98%) of graphene due to the low carbon solubility of Cu [40]. High-throughput production of single-layer graphene can also be achieved via CVD-integrated roll-to-roll processes (**Figure 1.2e**) [41–43]. In this thesis, CVD-based single-layer graphene was employed as a base for the nanopore platform owing to its versatility, scalability, and accessibility.

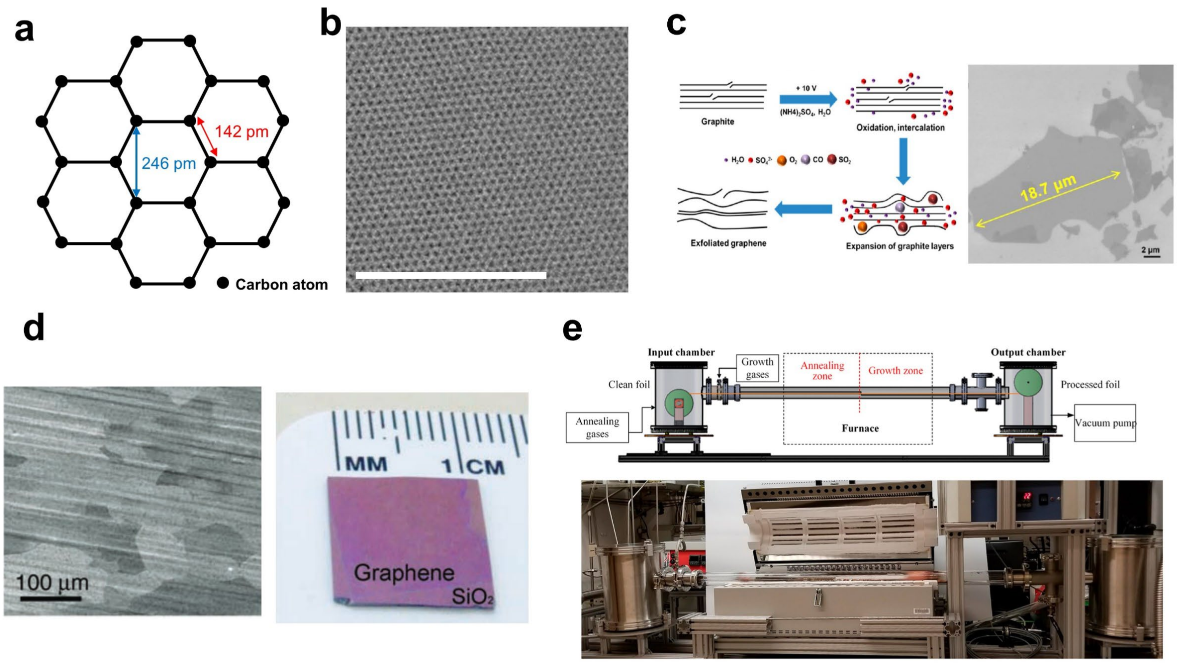
a
142 pm
246 pm
Carbon atom
b
c
Graphite
+ 10 V
$(NH4)_2SO_4$, H_2O
Oxidation, intercalation
H_2O SO_4^{2-} O_2 CO SO_2
Exfoliated graphene
Expansion of graphite layers
18.7 µm
2 µm
d
100 µm
MM 1 CM
Graphene
SiO_2
e
Input chamber
Growth gases
Annealing zone
Growth zone
Output chamber
Clean foil
Processed foil
Annealing gases
Furnace
Vacuum pump

Figure 1.2. Atomic structure of graphene and its synthesis methods. (a) Schematic of graphene honeycomb lattice connected through sp^2 hybridization. (b) Aberration-corrected high-resolution transmission electron microscopy (AC-HRTEM) image of the hexagon structure of single-layer graphene. The scale bar is 5 nm. (c) Graphene prepared by mechanical exfoliation in the liquid phase. Adapted with permission from [36], Copyright © 2014, American Chemical Society. (d) A centimeter-scale single layer produced by chemical vapor deposition (CVD). Reprinted with permission from [39], Copyright © 2009, The American Association for the Advancement of Science (AAAS). (e) Schematic and a photograph of the roll-to-roll graphene CVD reactor. Adapted with permission from [41], Copyright © 2018, American Chemical Society.

1.2.2 Graphene nanopores

Along with its exceptional properties, graphene is also considered to be a promising material for making the shortest solid-state nanopores that enable molecular transport [44–47] and DNA translocation [26]. Generally, pristine graphene lattice does not allow even the smallest gas molecule, helium [12], to permeate due to the close-packed electron density of the carbon atoms. Therefore, nanopores in graphene are formed as intrinsic defects, or can be created by focused electron and ion irradiation [48,49], energetic plasma [50–52], or chemical etching [44,53,54], which are the top-down routes of the pore creation. On the other hand, the direct bottom-up synthesis of graphene hosting sub-nanometer-sized apertures is desirable as it avoids post-synthetic lattice etching, which may complicate pore formation.

1.2.2.1 Bottom-up methods

Bottom-up synthesis of nanoporous graphene can be achieved by engineering the catalytic substrates or self-assembling the graphitic building blocks. Perforated graphene can be obtained by assembling an ordered array of graphene nanoribbons (**Figure 1.3a**) [55]. Also, nanoparticle-assisted CVD has been reported to render the synthesis of perforated graphene [56,57]. Since graphene is only absent in the region where the nanoparticles are on the catalytic substrate, the generated pore size is largely limited by the size of the nanoparticles, and they are generally 20–200 nm in size (**Figure 1.3b**). Another promising method is the direct incorporation of intrinsic vacancy defects into the graphene lattice by manipulating the precipitation and crystallization of carbon atoms during the synthesis. For instance, nanocrystalline graphene hosting molecular-sieving apertures was achieved by promoting the growth of small, misoriented grains, which eventually constituted the porous lattice structure (**Figure 1.3c**) [58]. The formation of intrinsic defects in graphene lattice can also be modulated by tuning the growth temperature, which affects the dissociation and precipitation of carbon precursors on the catalytic substrate (**Figure 1.3d**) [59]. The one-step synthesis of nanoporous graphene seems to be efficient; however, these methods require high-end pretreatments and can only result in nanometer-scale pores.

1.2.2.2 Top-down methods

Engineering nanopores in graphene using an ion beam reveals that a high-energy electron beam facilitates the knockout of the carbon atoms on the basal plane and thus the vacancy defect formation. Pores 2–40 nm in diameter were observed on graphene lattice via electron beam bombardment with an accelerating voltage of 200–300 kV [26,60]. Apart from the high-energy electron beam, focused ion beam (FIB) using He^+, and Ga^+ as the ion source was reported to be efficient in drilling nanopores in graphene lattice (**Figure 1.4a**) [48,49]. The principle behind ion bombardment is very similar to that behind the electron beam: the energy is transferred by the collision between charged particles and carbon atoms, resulting in breaking carbon–carbon bonds. Despite the advantages of simultaneous nanopore formation and imaging, both methods require sophisticated instrumentation. In addition, the size of resulting nanopores is limited by the beam size, making it hard to fabricate nanopores with a resolution comparable to small molecules like water and metal ions.

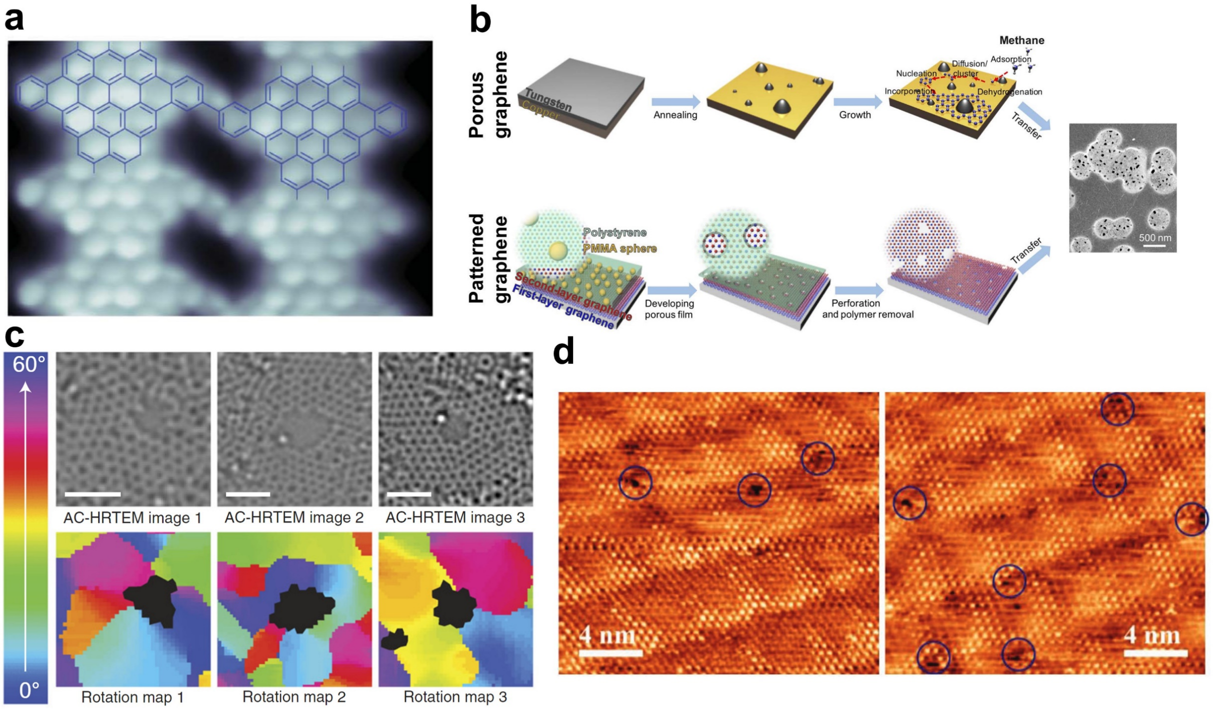
a
b
Porous graphene
Tungsten
Copper
Annealing
Growth
Methane
Adsorption
Diffusion/cluster
Nucleation
Incorporation
Dehydrogenation
Transfer
500 nm
Patterned graphene
Polystyrene
PMMA sphere
Second-layer graphene
First-layer graphene
Developing porous film
Perforation and polymer removal
Transfer
c
60°
0°
AC-HRTEM image 1
AC-HRTEM image 2
AC-HRTEM image 3
Rotation map 1
Rotation map 2
Rotation map 3
d
4 nm
4 nm

Figure 1.3. Graphene nanopores created using bottom-up methods. (a) Nanometer-size nanoporous graphene synthesized by cross-linking an ordered array of pores separated by ribbons. Reprinted with permission from [55]. Copyright © 2018, AAAS. (b) Schematic of single-layer porous graphene grown on tungsten nanoparticle / polymeric nanoparticles-patterned catalytic substrates. Reprinted with permission from [56]. Copyright © 2018 under a Creative Commons Attribution NonCommercial License 4.0 (CC BY-NC). (c) Quantitative orientation maps of the nanoporous graphene formed by misoriented grains at the edge of a pore. Reprinted with permission from [58]. Copyright © 2021 under CC BY-NC. Proceedings of the National Academy of Sciences of the United States of America (PNAS). (d) Atomic-resolution scanning tunneling microscope (STM) images of intrinsic defects in graphene on Cu foil synthesized via CVD at 900 °C. Reprinted with permission from [59]. Copyright © 2018 WILEY-VCH Verlag GmbH & Co. KGaA, Weinheim.

Energetic plasma created from gaseous species also serves as an efficient tool to etch nanopores in graphene lattice. This technique allows pore formation via direct knockout of the carbon atoms from the lattice using energetic radicals and enables tailoring the size of graphene nanopores. Such gases as Ar [61], H_2 [62], and O_2 [51,63] are often involved in the plasma etching process of graphene lattices. Among them, O_2 plasma provides the fastest etching and is proven sufficient to create sub-nanometer-sized pores showing the transport of water and small gas molecules (**Figure 1.4b**). The etching mechanism of O_2 plasma in graphene lattice is complex and still not well-understood, but generally, it is believed that the charged oxygen ions (O_2^+) may coexist with the atomic oxygen (O) once the plasma is generated [63]. They perform both physical bombardment (caused by O_2^+) and chemical etching (caused by O) depending on the pressure and plasma sources. In this thesis, we use O_2 plasma to create angstrom-scale graphene nanopores to study water evaporation under confinement.

On the other hand, the lattice of graphene can be also engineered using reactive etchants including O_3 (**Figure 1.4c**), UV/O_3 [53], O_2 [44,64,65], NO [65,66], or CO_2 [54]. NO, CO_2, and O_2 are most likely to expand the pre-existing defects (e.g., ~ 127 kJ/mol for O_2 and ~ 266 kJ/mol for CO_2) instead of making new nucleation sites in the graphene lattice due to the high energy barrier (167 kJ/mol, 200 kJ/mol, and 433 kJ/mol for NO, O_2, and CO_2, respectively) [54,65]. For instance, by exposing graphene hosting pre-etched pores created by ion irradiation to O_2 at 300 °C, one can tune the size of graphene nanopores and obtain H_2 sieving nanopores. Furthermore, nanometer-sized vacancy defects in graphene lattice have been achieved by the post-synthetic etching of graphene with Å-scale pores using CO_2 at high temperatures. In contrast, highly reactive O_3 or UV/O_3 can initiate pore nucleation in a pristine graphene lattice. In the case of UV/O_3, the presence of UV facilitates the dissociation of O_2 into atomic oxygen, O, and the generation of O_3. Both of them have lower energy barriers for pore nucleation in graphene lattice than ozone (~10 kJ/mol for O and ~80 kJ/mol for O_3) [67,68]. The combination of O and O_3 is proven effective in fast nanopore etching in graphene. O_3 etching at high temperatures in the absence of O is also promising for creating nanopores with angstrom precision that enable CO_2/N_2 separation [44,53]. According to the literature, chemisorbed epoxy groups are formed in the first stage of O_3 etching, followed by the diffusion of the species and then ether cluster formation. This ends up with the C–C bond breaking because of the buckling strain acting on the lattice. Overall, chemical etching methods enable tailor-made nanopores in graphene lattice and can be combined with other pore etching techniques because of their versatility and flexibility. In this thesis, we employ O_3 (for pore nucleation) and CO_2 (for pore expansion) as etchants to achieve nanopores with sizes approaching those of hydrated ions.

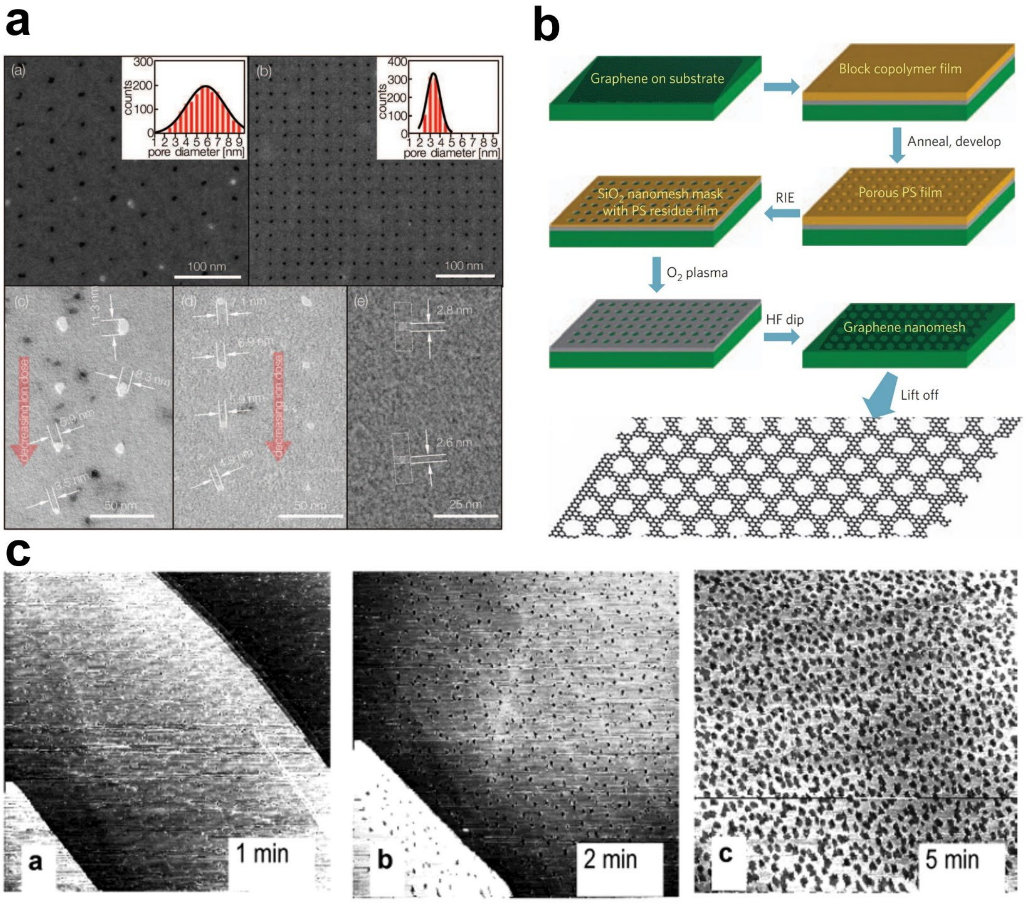
a
(a)
300
200
100
0
counts
1 2 3 4 5 6 7 8 9
pore diameter [nm]
100 nm
(b)
400
300
200
100
0
counts
1 2 3 4 5 6 7 8 9
pore diameter [nm]
100 nm
(c)
11.3 nm
8.3 nm
5.9 nm
3.5 nm
decreasing ion dose
50 nm
(d)
7.1 nm
6.9 nm
5.9 nm
4.9 nm
decreasing ion dose
50 nm
(e)
2.8 nm
2.6 nm
25 nm
b
Graphene on substrate
Block copolymer film
Anneal, develop
Porous PS film
RIE
SiO$_2$ nanomesh mask with PS residue film
O$_2$ plasma
HF dip
Graphene nanomesh
Lift off
c
a
1 min
b
2 min
c
5 min

Figure 1.4. Graphene nanopores created using top-down methods. (a) Scanning electron microscope (SEM) images of nanometer-sized graphene pores made via focused ion beam (FIB) milling. Reproduced from [48] with permission from the Royal Society of Chemistry. (b) Schematic of the fabrication of a graphene nanomesh using a SiO$_2$ template and O$_2$ plasma. Reproduced with permission from [52]. Copyright © 2010, Nature Publishing Group. (c) SEM images of ozone etching on graphite. Reprinted with permission from [68]. Copyright © 2003, American Chemical Society.

1.3 Graphene nanopores for fluidic transport

The stability, atomic thickness, and electrical tunability of graphene nanopores enable molecular transport in a new regime. The transport of confined gas, liquid, and ionic species in graphene nanopores has been intensively studied from both theoretical and experimental perspectives in the literature.

1.3.1 Gas molecules

Theoretically, the gas transport through a single graphene nanopore comprises direct gas diffusion, surface adsorption, and pore translocation (**Figure 1.5a**) [45,69,70]. It was suggested that the direct gas diffusion from the bulk phase to the vicinity of nanopores could be described by the classical kinetic theory of gas, while the surface adsorption on graphene lattice and the pore translocation steps are reaction kinetics models derived from the transition-state approach. In this regard, density functional theory (DFT) is used to calculate the energy barrier for pore translocation [71,72]. Gas permeation can also be simply modeled by considering only the steric effect in molecule–pore interactions. In this context, gas molecules are assumed to behave like hard spheres with known sizes, and only those having negligible adsorption (e.g., He and H_2) onto graphene lattice are considered [73]. On the other hand, molecular dynamics (MD) enable the direct calculation of gas permeation from graphene nanopores with more insights into the interaction between the molecules and the surface, pore edge, or functional groups (**Figure 1.5b**) [71,74,75].

Experimentally, Koenig *et al.* reported selective transport of small gas molecules (i.e., H_2 and CO_2) over other larger N_2 and CH_4 molecules in extremely small pores (~3.4 Å pores) in a bi-layer graphene balloon, showing that the size-exclusion effect governed the permeation (**Figure 1.5c**). Permeance decreased with the increasing kinetic diameter of gas molecules in the single-layer graphene nanopores with an exception for such gases as CO_2 and N_2O, which have a strong interaction with graphene lattice/pore edges (functional groups) resulting in enhanced transport [76]. He *et al.* also showed selective CO_2 permeation by engineering the properties of the surface and pore edge with a CO_2-philic polymer layer. In contrast, the gas transport in larger graphene pores (> 5 nm) follows the effusion theory [49], where the transport rate is inversely proportional to the mass of a species; however, the gas permeances from those pores are much higher than from the existing polymeric membranes (**Figure 1.5d**). This could be attributed to the atomic thinness of graphene that enables almost resistance-free transport [12].

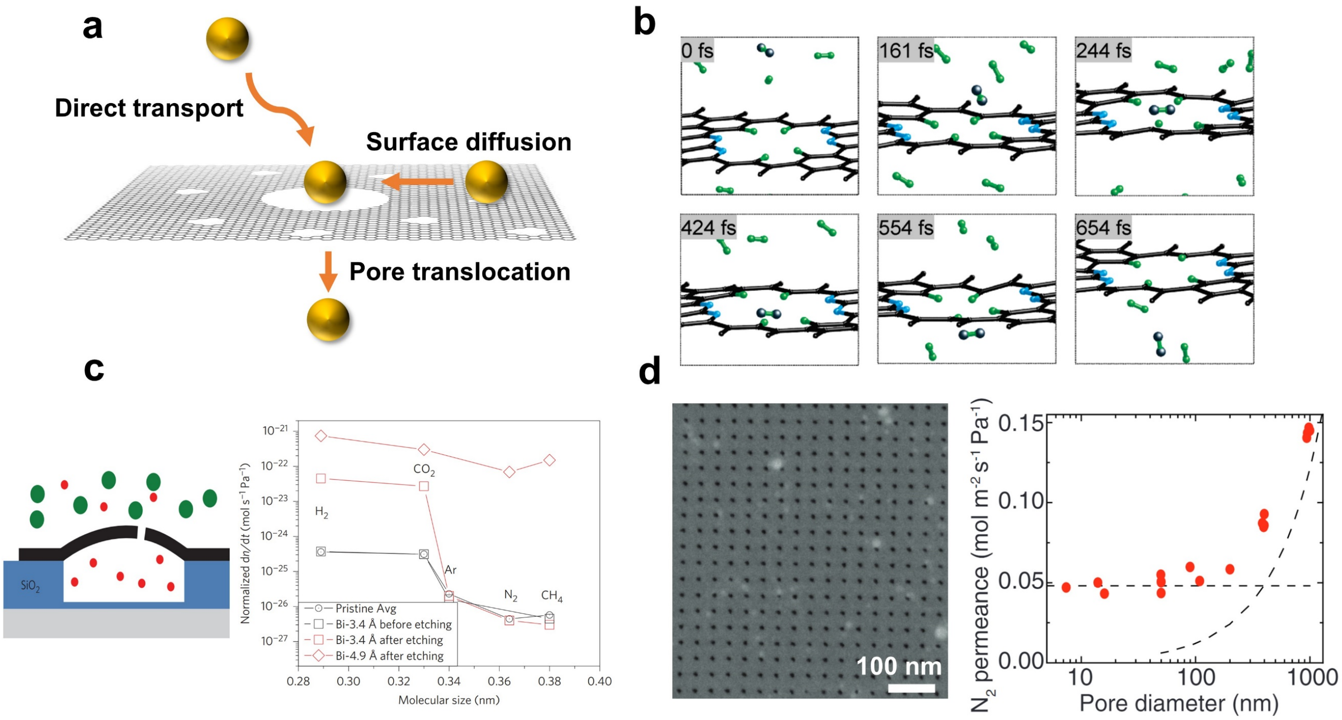

Figure 1.5. Gas transport across graphene nanopores. (a) Schematic of the gas molecule transport mechanism through nanoporous graphene. (b) Snapshots of H_2 diffusing through the nitrogen-functionalized graphene nanopore from first principles molecular dynamics simulations. Reprinted with permission from [75]. Copyright © 2009, American Chemical Society. (c) Schematic of a microscopic graphene membrane on a 5-μm SiO_2 substrate and the transport rates of different gases through a UV-ozone etched nanoporous graphene. Reprinted with permission from [53]. Copyright © 2012, Nature Publishing Group. (d) Scanning electron microscope (SEM) image of graphene nanopores drilled using Ga focused ion beam (FIB) and N_2 permeances per pore through different-diameter apertures (red circles) compared with predictions of the effusion theory (horizontal dashed line) and modified Sampson's model (dashed curve). Reprinted with permission from [49]. Copyright © 2014, AAAS.

1.3.2 Water and organic solvents

Water transport across graphene nanopores has been intensively studied using simulations due to the emerging demands for energy-efficient water purification technologies. In previous studies, water (~ 2.65 Å) [77] showed a strong geometry- and functional-group-dependent ultrafast permeation when the pore size was below 2 nm [78–81]. The water network structure and the hydrogen dynamics near the pore mouth dominate the water permeability. It was shown that water could permeate through pores larger than 3 Å with a small energy barrier [79]. However, in the presence of hydrogen-terminated pores, water molecules tend to form an ordered arrangement in the vicinity of the pore mouth, and this ordering slows down the hydrogen bond dynamics between the water and the pore, resulting in less probability of water permeation across the nanopores (**Figure 1.6a**) [82]. In contrast, pores with hydrophilic functional groups allow water transport with a low entropic barrier and thus faster water permeation across the nanopores. Another study suggested that the enhanced hydrogen-bond dynamics between pore edges and water molecules would boost the water evaporation across the liquid–vapor interface of graphene nanopores [83]. Similar to CNT, single-file water configuration has been observed when permeating across the smallest nanopore only accommodating one water molecule (**Figure 1.6b**) [84]. Besides, the movement of water molecules passing through the nanopores becomes discrete rather than continuous with decreasing pore sizes [85], indicating the need for a new theory or correction to the classical theory to explain hydrodynamics at the nanometer scale [86]. Experimental evidence of ultrafast water flow rate from O_2-plasma-etched graphene nanopores (pore diameter < 1 nm) showed tremendously high values (three water molecules per pore per second) exceeding those through biological channels (**Figure 1.6c**) [51]. This finding was attributed to a unique low-friction flow of water permeating through a one-atom-thick nanoporous graphene sheet, similarly to the ultrahigh water flow rate observed in graphene oxide laminates. On the other hand, water transport in larger graphene pores can be captured by the modified Sampson's model, but the permeation rate is still high compared to commercial membranes due to the ultrathinness of the material (**Figure 1.6d**) [49]. For instance, the water vapor transmission rate for a bi-layer graphene with 400-nm pores has demonstrated values two orders of magnitude higher than waterproof yet breathable textile membranes in the market.

Although being much less explored, non-aqueous liquids, such as common organic solvents, passing through nanopores and nanochannels have shown a great potential for energy-efficient separation technologies beneficial to chemical and pharmaceutical industries. Owing to its chemical and thermal stability, single-layer graphene enables a nanopore platform for this kind of study. Similar to water, the permeation of organic solvents is largely determined by pore size, pore structure, and functional groups. Recent studies uncovered that some common organic solvents exhibit subcontinuum geometry-dependent flow through sub-nanometer pores [86]. A combination of Sampson's model with pore size distribution modeled by Monte Carlo simulations well describes the permeance of the solvents [87]. It was also found that the solvent molecules pass through the pores with certain preferential configurations, potentially allowing selective isomer separations. The high permeance of organic molecules through nanoporous graphene membranes [88,89] may open opportunities for industrial applications, but the transport mechanism details require further investigation.

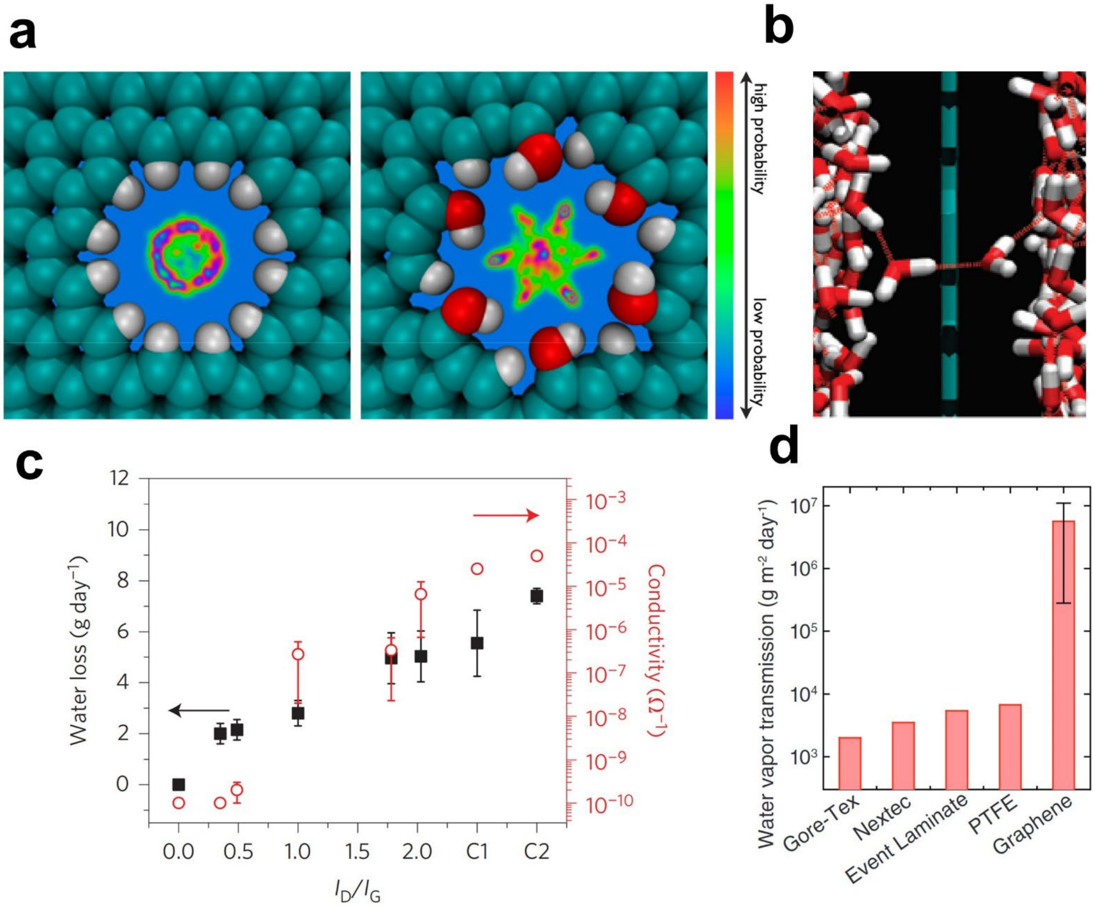

Figure 1.6. Water transport across graphene nanopores. (a) Distribution of oxygen-water inside a hydrogenated (left) and a hydroxylated nanopore (right). Reprinted with permission from [82]. Copyright © 2012, American Chemical Society. (b) Single-file water configuration across a graphene nanopore from molecular dynamics simulations. Reprinted with permission from [84]. Copyright © 2010, American Chemical Society. (c) Water transport rate from O_2-plasma-etched nanoporous graphene membrane suspended on a 5-μm SiNx substrate as a function of I_D/I_G ratio (i.e. plasma exposure time). C1 and C2 are controls with tears or broken graphene membranes, respectively. Reprinted with permission from [51]. Copyright © 2015, Nature Publishing Group. (d) Water vapor transmission rate from 400-nm porous graphene membranes compared with commercial textile membranes. Reprinted with permission from [49]. Copyright © 2014, AAAS.

1.3.3 Ionic species

Ion channels are extremely complex, and many questions remain unanswered. Molecular dynamics has been intensively utilized in understanding the principle behind ionic channels in proteins that show high ion-selective permeability [90–92]. The mechanism of ion transport under nanoconfinement includes steric hindrance, electrostatic attraction/repulsion, dielectric effects (i.e., partial dehydration), and van der Waals (vdW) interaction [93]. In the case of diffusion in a long pore channel, the frictional effect and the liquid's viscosity also play important roles in ion transport. The first hydration shell diameters of alkali metal ions span within 6.6–7.6 Å, whereas those of Mg^{2+} and Ca^{2+} are 8.56 and 8.24 Å, respectively. Thus, the effective pore size shall exceed ~8 Å for those ions' transport without losing the hydration shell (**Figure 1.7a**) [79]. In this regard, the smallest hydrated ion (i.e., K^+) permeates through a neutral nanopore faster than other ions. However, when the pore is smaller than the size of the hydrated ions, partial dehydration occurs, and extra energy is required for ions to pass through the pore [92,94]. The energy barriers not only depend on the pore size but also the dehydration energy of ions, making the mechanism behind ion transport in nanopores less straightforward compared to gas transport [95,96]. For instance, Li *et al.* [95] reported that the selectivities of K^+/Li^+ were higher through neutral pores with diameters of 4.1 Å, whereas an opposite trend was observed in pores with a larger diameter (5 Å) under a certain applied voltage. They concluded that the behavior of ions in pores smaller than their hydrated diameter is determined by both size exclusion and hydration water exchange. They explained that Li^+ tends to pass through 5 Å pores with an intact hydration shell due to its higher dehydration energy, whereas K^+ loses one associated water molecule, resulting in a higher energy barrier of K^+ across the pore compared to Li^+ (**Figure 1.7b**). On the other hand, things become much more complicated in charged nanopores. The charges at the pore edges normally come from the functional groups or oxidation during the pore formation [47,97]. The charges influence the water molecule shedding from the hydration shell and electrostatics between the nanopore and the target ions [90]. For instance, negatively charged pores facilitated the transport of K^+ while repelling Cl^- in a graphene pore > 2 nm, giving rise to K^+/Cl^- selectivity over 100 [47].

Functional groups that show coordinative interactions with ions also play an important role in the selective permeation of ion species with the same valence electron. A reported example with iminodiacetate-functionalized polymeric nanochannels showed that ion-functional groups' binding energies affect membrane permeabilities of Cu^{2+}, Ni^{2+}, Zn^{2+}, Co^{2+}, and Mg^{2+} [98]. Weaker binding species had higher entrance resistance compared to stronger binding species, so their partitioning into the channel was hindered. Despite many efforts and conjectures made using simulations about artificial ion-selective nanopores/nanochannels mimicking their biological counterparts, there is no comprehensive understanding of the transport mechanism under nanoconfinement, especially from the experimental perspective. For example, Esfandiar *et al.* [24] suggested that ion mobility measured from angstrom-sized slits is dominated by the dehydration of each ion species (**Figure 1.7c**). In contrast, Rollings *et al.* observed that the pore conductance among monovalent cations follows the trend of $K^+ > Na^+ > Cs^+ > Li^+$ in graphene nanopores with sizes spanning over 2–23 nm (**Figure 1.7d**) [47]. The latter finding cannot be simply explained by steric effect or dehydration energy as Cs^+ has the smallest hydrated diameter while K^+ has the lowest dehydration energy. The experimental data for ion transport in sub-nanometer-scale graphene nanopores is limited, and a detailed investigation is needed urgently.

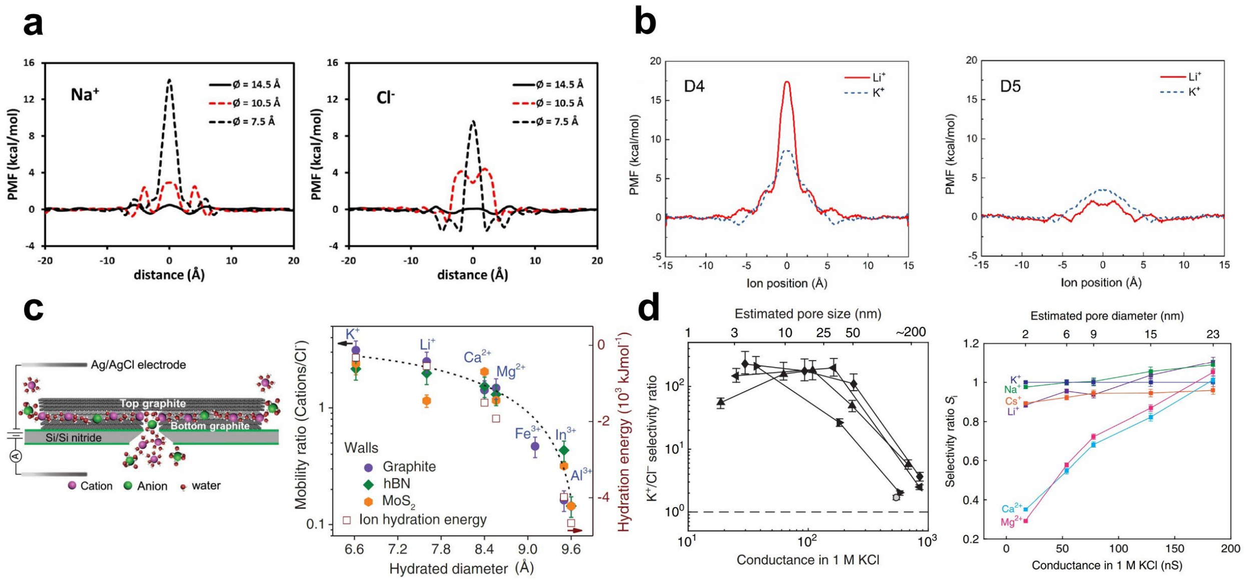

Figure 1.7. Ion transport across graphene nanopores. (a) The one-dimensional potential of mean force (PMF) profiles of Na^+ and Cl^- passing through nanopores of different sizes. Adapted with permission from [79]. Copyright © 2013, American Chemical Society. (b) PMF profiles of K^+ and Li^+ of D4 (diameter: 4.1 Å) and D5 (diameter: 5.0 Å) pores. K^+ experiences a lower energy barrier compared to Li^+ across D4 while the trend is opposite for D5. Adapted with permission from [95]. Copyright © 2021 Elsevier B.V. All rights reserved. (c) A schematic of ion transport through angstrom-scale graphene slits and the measured ion mobility. It shows hydration-energy-dependent ion transport behaviors. Adapted with permission from [24]. Copyright © 2017, AAAS. (d) K^+/Cl^- selectivity measured from graphene nanopores of different sizes and relative pore conductance for several cations as functions of pore size. Reprinted with permission from [47]. Distributed under the terms of CC BY license, Nature Publishing Group.

1.3.4 Protons

Proton shows a different transport behavior compared to ions and water. The early studies done by Hu *et al.* reported that mechanically exfoliated graphene allows the transport of protons while rejecting He [99,100]. The pristine graphene also showed a high selectivity of protons over deuterons [99,101], promising for difficult isotope separations. Interestingly, monolayer h-BN demonstrated similar properties while it was not observed in MoS_2 [100]. Pristine graphene can be further engineered by post-treatments (e.g. pore etching, doping etc.) to enhance the proton permeance. For instance, N-doped porous graphene via N_2 plasma provided high proton permeance along with high H^+/Cl^-. The fast proton transport was assisted by the presence of N atoms in the graphene lattice inspired by the design of biological protein channels [102]. Although the experimental data only provide limited insights to date, efforts are increasingly made to study proton transport through graphene nanopores due to the high demand for hydrogen-based energy applications, particularly fuel cells.

1.4 Challenges and opportunities for graphene nanopores in studying mass transport at the nanoscale

As discussed above, graphene nanopores demonstrate great potential as a platform for studying fluidic dynamics at the nanoscale; however, the experimental input is limited, and conflicting conclusions are often made by those few research groups who succeed. Furthermore, artificial nanopores are designed to mimic the high permeance and selectivity of their biological counterparts, but they are still far from the expectation. Graphene nanopores for both fundamental study and high-performance applications are yet to be achieved, and reaching the pore size close to the target species size remains challenging. For instance, the kinetic diameter of a water molecule and a K^+ ion are 2.65 Å and 6.62 Å [77], respectively, and only very few studies are focused on the scale close to these values. In addition, a system that shows stability and integrity (i.e., crack-free) in harsh conditions (e.g., pressurization, high salinity, high temperature, etc.) is important to succeed in such a study and wide range of applications.

1.5 Thesis outline

The introduction, **Chapter 1**, reviews the background of hydrodynamics at the nanoscale, properties, current state of affairs, and challenges with graphene nanopores.

Chapter 2 presents the study of enhanced water evaporation from angstrom-scale graphene nanopores, which is the first experimental report focusing on water evaporation under the ultimate confinement. This chapter describes the design, fabrication of the nanoporous graphene devices, and the water evaporation enhancement from those nanopores. The mechanism behind the phenomena is explained based on molecular dynamics simulation which is performed by collaborators (Anshaj Ronghe and Prof. K. Ganapathy Ayappa at IISC Bangalore, India).

Chapter 3 reveals the monovalent and divalent ion transport across graphene nanopores in the sub-nanometer regime. Nanopores tailor-made using a decouple pore nucleation/expansion method show efficient metal ion sieving of K^+ and Li^+ over Mg^{2+}. The pore size and structure can adjust the diffusion of ions across the nanopores, suggesting that the sterically induced partial dehydration may play an important role in the observed monovalent/divalent cation selectivity.

The interesting transport properties of water and ions discussed in **Chapters 2** and **3** are promising for energy-efficient water purification or metal ion extraction applications. Therefore, to utilize the potential of graphene nanopores, **Chapter 4** demonstrates the fabrication of large-area nanoporous graphene membranes, a step further toward industrial application. It reports a centimeter-scale gas-sieving nanoporous graphene film on a commercial low-cost stainless-steel nonwoven mesh where the mechanical reinforcement is provided from a two-layer composite carbon film.

Finally, **Chapter 5** gives an overview of all achievements covered in this thesis, perspectives on developing graphene nanopore platforms, new opportunities for graphene nanopores in fluidics dynamics, and more.

Chapter 2 Enhanced Water Evaporation From Å-scale Graphene Nanopores

Adapted with permission from Wan-Chi Lee, Anshaj Ronghe, Luis Francisco Villalobos, Shiqi Huang, Mostapha Dakhchoune, Mounir Mensi, Kuang-Jung Hsu1, K. Ganapathy Ayappa and Kumar Varoon Agrawal1*, Enhanced Water Evaporation from Å-scale Graphene Nanopores, a manuscript in submission.*

Wan-Chi Lee designed and performed the membrane fabrication, the permeation tests, and the characterization, analyzed the data, and wrote the paper with other authors. The simulation work was performed by Anshaj Ronghe and K. Ganapathy Ayappa from Indian Institute of Science, Bangalore.

Abstract

Enhancing the kinetics of liquid-vapor transition from nanoscale confinements is an attractive strategy for developing novel evaporation and separation applications. The ultimate limit of confinement for evaporation is an atomic-thick interface hosting angstrom-scale nanopores; however, this has not been studied so far. Herein, we report highly enhanced water evaporation rates when angstrom-sized oxygen-functionalized graphene nanopores are placed at the liquid-vapor interface. Evaporation flux increase for the smaller nanopores with enhancement up to 35-fold with respect to the bare liquid-vapor interface. Molecular dynamics simulations reveal that oxygen-functionalized nanopores render rapid rotational and translational dynamics to the water molecules due to a reduced and short-lived water-water hydrogen bonding. Potential of mean forces (PMF) analysis demonstrates that the free energy barrier for water crossover decreases in the presence of nanopores at the atomically thin interface, which further explains the enhancement in evaporation flux. These findings can enable the development of energy-efficient technologies relying on water evaporation.

2.1 Introduction

The unusual effect of nanoscale confinement of water on its properties, including phase transition behavior, is of fundamental scientific interest [103–106]. Classical explanations such as those based on Hertz-Knudsen (HK) relationship [107,108] describing the evaporation of water from bulk surfaces break down for water confined in nanoscale pores and channels, and enhanced evaporation fluxes have been predicted [15,109]. An enhancement in the evaporation flux is attractive for applications such as energy-efficient steam generation [110], cooling [111], and desalination technologies [112] for potable water. An enhancement in the evaporation flux with the decreasing dimensions in nanochannels or a single nanopore has been attributed to several effects. These include the formation of an extended meniscus outside the pore entrance [113], gap-dependent line tension between water and confining container [109], surface roughness [106], and surface charge induced concentration change of hydronium ions [114]. The validity of the HK relationship has been questioned while studying liquids in nanoscale confinement where additional complications due to density inhomogeneities and disjoining pressure effects must be considered [115].

Molecular dynamics (MD) simulations have been widely used to provide molecular insights into evaporation from a bare liquid-vapor interface (BLVI) [116–118]. Due to reduced hydrogen bonds (HBs) at the liquid-vapor interface, water molecules exhibit faster translational [119] and rotational dynamics [120] than the water molecules present in the bulk phase. Yet, only a few studies have focused on the evaporation from nanoscale pores [83] and channels [109,121,122], which are two distinct pore topologies. Enhanced evaporation of water through nanoporous graphene [83] has been attributed to the lowering of the local interfacial free energy and reduced HB networks, while in contrast, modulated capillary and interfacial wetting effects play a role in nanochannels [121,123]. The ultimate limit of a nanoscale evaporation conduit is a two-dimensional (2D) nanopore with a size commensurate to the water molecule [124]. In this topology, water molecules exiting the nanopore are in contact with only an atomically thick layer of edge atoms. At this limit, HB network of water molecules is disrupted [125–127], affecting their translational dynamics [104] which in the past has led to interesting phenomena when water is confined at this length-scale, e.g., rapid transport of liquid water inside carbon nanotubes [104,128,129]. The interplay of entropic- and enthalpic-stabilized states of confined water, depending on the extent of hydrogen bonding, has led to the observation of diameter-dependent depression and the elevation in the freezing transition of water leading to the formation of ice nanotubes at unexpectedly high temperatures

[11]. The 2D nanopore, the subject of this communication, is in sharp contrast to other pore topologies realized in recent experiments where exiting water molecules are in contact with extended surfaces depending on the pore geometry [16].

Currently, there is no available experimental data on water evaporation from 2D nanopores commensurate with the size of the water molecule. A challenging factor in such a study is to ensure that the evaporation flux is neither controlled by the external mass transfer of the water vapor nor by the rate of supply of the liquid water to the evaporation front [16,56]. Herein, we address these issues by placing liquid water on a 2D evaporation front composed of single-layer graphene hosting angstrom-sized pores. Evaporation was carried out in vacuum in order to diminish the external mass transfer resistance. We observed rapid evaporation from the nanoporous graphene interface with fluxes that were significantly larger than that from the BLVI. The enhancement in the evaporation rate, defined as the ratio of evaporation flux from graphene nanopores to that from BLVI, increased for the ensemble of nanopores with a smaller pore size with enhancement up to 35-fold for the smallest pores. Molecular insights into the enhanced evaporation are obtained with extensive atomistic MD simulations with edge-functionalized nanopores. The presence of nanopores at the liquid-vapor interface increases the translational and rotational dynamics of water molecules in the liquid phase, reduces the number of HBs per molecule next to the interface, and reduces the free energy barrier for water molecules to cross the liquid-vapor interface.

2.2 Methods and materials

2.2.1 Synthesis of single-layer graphene by low-pressure chemical vapor deposition (LPCVD)

Single-layer graphene was synthesized by the LPCVD process using a pre-annealed copper foil (50 μm thick, 99.9% purity, Stream). Briefly, the foil was subjected to CO_2 and H_2 atmosphere at 1000 °C for 30 minutes, respectively. Subsequently, 24 sccm of CH_4 and 8 sccm of H_2 were introduced into the reactor at a total pressure of 460 mTorr for 30 minutes. The reactor was then rapidly cooled down to room temperature once the synthesis was done.

2.2.2 Generation of pores in graphene using O_2 plasma

Incorporating nanopores in the graphene lattice was done by radiofrequency powered O_2 plasma. Briefly, the as-synthesized graphene on a copper foil was placed in the chamber of a plasma generator (MTI, EQ-PCE-3, 13.56 MHz, 18 W). Afterward, the chamber was first evacuated and then maintained at a total pressure of 80 mTorr under a continuous O_2 flow. Following this, plasma was initiated for 1–3 s to generate nanopores.

2.2.3 Fabrication of porous support film on graphene

The fabrication of porous support film on graphene was carried out by following a method reported before [130]. Briefly, the precursor of NPC was prepared by dissolving 0.1g poly(styrene-*b*-4-vinyl pyridine) and 0.2 g turanose in 2 g N,N-dimethylformamide. Subsequently, the solution was heated at 180 °C for 3 h. The NPC film was obtained by spin coating the solution on porous graphene resting on a Cu foil followed by pyrolysis at 500 °C in a H_2/Ar atmosphere for 1 hour. The resulting graphene film, now supported by NPC film, was then placed in a $Na_2S_2O_8$ bath to remove the Cu foil. After that, the floating graphene/NPC film was rinsed in deionized water several times and then was transferred onto a macroporous tungsten foil hosting an array of 5 μm pores.

2.2.4 Aberration corrected high resolution transmission microscopy (AC-HRTEM) imaging

The samples for AC-HRTEM were prepared by transferring porous graphene to 400 mesh Au TEM grids using a porous polymer-assisted transfer method reported elsewhere [131]. Briefly, a thin porous polybenzimidazole copolymer (fumion® AM provided by FUMATECH BWT GmbH, Germany) film was first prepared on top of a Cu foil by the nonsolvent-induced phase separation. This film acts as a lacey support for the transfer of graphene from Cu to the TEM grid. The polymer film was then wet-transferred on the porous graphene sample and pyrolyzed at 500 °C in the flow of H_2/Ar leading to reinforcement of porous graphene with lacey carbon film. The Cu foil below the graphene film was then etched in an etchant bath, and the resulting reinforced graphene film floating on water was transferred to the TEM grid. Before imaging, the reinforced nanoporous graphene samples were cleaned inside activated carbon at 900 °C for one hour in the presence of H_2 to remove contaminations covering the nanopores.

AC-HRTEM was performed using a double-corrected Titan Themis 60–300 (FEI) equipped with a Wein-type monochromator. An 80 keV incident electron beam was used for all experiments to reduce the electron radiation damage. The incident electron beam was monochromated (“rainbow” mode illumination) to reduce the effects of chromatic aberration, and a negative Cs of $\sim$ 17–21 μm with slight over-focus were used to give a “bright atom” contrast in the images. In addition, a slit was used to expose only the area of the sample being imaged to the electron beam. The images were processed using average and bandpass filters.

2.2.5 Other characterization

Scanning electron microscope (SEM) images were obtained by using FEI Teneo scanning electron microscope at 1.0–5.0 kV and working distances of 2.5–5.0 mm. No conductive coating was applied to the substrates before SEM. TEM imaging and selected area electron diffraction (SAED) of the composite graphene film were conducted by FEI Tecnai G2 Spirit Twin transmission electron microscope with a 120 kV incident electron beam. Raman measurement was carried on graphene on a Cu foil right after the synthesis and pore etching using 457 nm excitation and Renishaw micro-Raman spectroscope with 100× objective. The obtained Raman data was analyzed using a MATLAB script. For the calculation of the *D* and the *G* peak heights, the background was subtracted from the Raman data using the least-squares curve fitting tool (lsqnonlin). X-ray photoelectron spectroscopy (XPS) measurements on O_2 plasma-treated nanoporous graphene (NSLG) resting on a Cu foil were carried out on Axis Supra (Kratos Analytical) using the monochromated Kα X-ray line of an aluminum anode. The pass energy was set to 20 eV, and the step size was set to 0.1 eV. The peak fitting was performed using CasaXPS, and Shirley method was used for background subtraction.

2.2.6 Hydrogen transport

The measurement of hydrogen transport through porous graphene was carried out in a homemade permeation cell. The mass flow controllers (MKS) were pre-calibrated using a bubble flow meter, delivering a pre-determined amount of H_2 to the feed side. The permeate side was swept with Ar at 1 bar. The permeate was connected to a pre-calibrated mass spectrometer allowing real-time analysis of the permeation rate. The absolute pressure difference between the feed and the permeate sides was kept at 1–1.5 bar. The nanoporous graphene on a tungsten support was sealed in a VCR-based module using two metal gaskets. The gas flux was calculated once the steady state was reached. The permeance, J_i, of the gas was calculated according to **Equation 2.1**:

$$J_{H_2} = \frac{X}{A\Delta P} \qquad \textbf{(Equation 2.1)}$$

where X is the flow rate of H_2, A is the area of the nanoporous graphene film, and ΔP is the pressure difference between the feed and the permeate sides for H_2.

2.2.7 Water evaporation measurements

Water evaporation experiments were performed using a constant volume/variable pressure test method similar to the literature [132]. Briefly, nanoporous graphene on tungsten supports was sealed in a stainless-steel VCR-based module using two metal gaskets. The feed side (support film side) was filled with liquid water (Mili-Q water). The permeate side had a constant volume chamber which was evacuated to 500–600 mTorr using a scroll pump. The measurement was initiated once the valve connected to the pump was closed, isolating the permeate side from the vacuum pump, and the valve connected to VCR module hosting nanoporous graphene was opened, allowing the collection of water vapor in the constant volume chamber. The corresponding pressure rise in the constant volume chamber was then measured using a pressure transducer (Omega engineering, PX409-USBH). The entire setup was carefully sealed to ensure a leak-free operation. The water evaporation flux was calculated using the ideal gas equation. The volume of the chamber was 5.9 mL in the measurement of graphene film and the support films .

The evaporation flux from the BLVI was measured using the same setup and evaporation conditions with one modification. In this case, a perforated W foil without membrane on top was placed in the VCR module filled with Mili-Q water. The volume of the chamber was 184 mL in the measurement of BLVI.

2.2.8 Density functional theory (DFT) calculations

Quantum ESPRESSO [133] was used to carry out DFT calculations [134,135] to investigate the optimal structure of functionalized graphene nanopore. The plane-wave basis sets were used. Cutoffs of 50 and 500 Rydbergs were employed for the wave function and charge density, respectively, for the electronic wave function expansion. Perdew–Bruke–Ernzerhof functional [136] was used to describe the exchange-correlation. Ultrasoft pseudopotentials [137] were employed for the interactions between the ionic core and valence electrons. A vacuum of 2 nm was used to avoid interactions between the periodic images along the direction normal to the functionalized nanoporous graphenes' (FNPGs) surface. Due to the large supercell, the Brillouin zone sampling was restricted to the Γ point. Broyden–Fletcher–Goldfar–Shanno scheme was employed to perform structural relaxation until the Hellmann–Feynman forces were less than 0.001 Ry/bohr. London dispersion corrections were described using DFT-D2 functional [138]. The relaxed unit cells were replicated in *x*-*y* plane to generate FNPGs with four functionalized nanopores.

2.2.9 Charge calculations

Partial atomic charges of the relaxed FNPGs were obtained by doing charge calculations based on CHELPG scheme [139] on the level of the Hartree–Fock/6-31G* basis set using Gaussian09 software [140]. The charges on the complete unit cell of the FNPGs are available upon request.

2.2.10 Molecular dynamics (MD) simulations

All MD simulations were performed using GROMACS 5.1.4 simulation package [141,142]. For all cases, the attractive wall, the FNPG, and the piston were located perpendicular to the *z*-axis. Owing to the hexagonal lattice of graphene, a parallelepiped simulation box was used.

For water evaporation simulations through FNPGs, a water box with 8290 water molecules was equilibrated at 25 °C (298 K) and pressure of 1 bar. The dimensions of the water box after equilibration were $a = 6.4064$ nm, $b = 6.4064$ nm and $c = 7$ nm. This water box was subsequently enclosed along the *z* axis with the FNPG and a piston to create the water reservoir for evaporation studies. An attractive wall was placed at a distance of 8 nm from the FNPG in the vapor space. A vacuum region was then extended beyond the attractive wall and the piston to ensure sufficient space between periodic images of the system along the *z*-direction. Periodic boundary conditions were applied in all three directions. The final dimensions of the simulation box were $a = 6.4064$ nm, $b = 6.4064$ nm, and $c = 150$ nm.

For studying the evaporation of water molecules from a BLVI, initially, a box with 42650 water molecules was equilibrated to a temperature of 25 °C (298 K) and pressure of 1 bar. The dimensions of this water box after equilibration were $a = 6.4064$ nm, $b = 6.4064$ nm and $c = 36$ nm. The longest dimension of this water box was then extended by 10 nm on both sides of the water film and attractive walls were placed at the two ends of this box. A vacuum region was then extended beyond the attractive walls and the dimensions of the simulation box periodically repeated in three directions are $a = 6.4064$ nm, $b = 6.4064$ nm and $c = 500$ nm.

All atoms of the FNPGs except the functional groups terminating the nanopores were fixed in their respective atomic positions throughout the simulation. All our simulations were carried out with the TIP4P-Ew [143] water model since it captures a broad range of properties of water, significant to our study. SHAKE [144] algorithm was used to fix the bond angle and bond lengths of the water molecules. All-atom optimized potentials for liquid simulation [145] parameters were used for the FNPGs along with the computed charges. Nonbonded interactions were modeled by using dispersive and electrostatic forces. Van der Waals interactions were modeled using Lennard–Jones potential with a cutoff of 1.2 nm. Interaction parameters between the carbon atoms of the FNPGs and water molecules were adopted by Werder *et al.* [146] to reproduce the macroscopic contact angle of a water droplet on a graphite sheet. Lorentz–Berthelot mixing rules were applied for the cross-interaction parameters for the Lennard–Jones potential between other unlike pairs. Particle-particle particle-mesh (PPPM) algorithm [147] was used to compute the long-range electrostatic interactions with a cutoff of 1.0 nm for real space force calculations. Leap frog algorithm was employed to integrate the equations of motion with a timestep of 1 fs. The temperature was maintained at 298 K (25 °C) using the Nose–Hoover thermostat with the time constant of 0.1 ps. First, the system was equilibrated for 10 ns, and then the production run was done for 500 ns. The trajectories of water molecules were stored at every 2 fs to analyze various structural and dynamical properties.

2.3 Results and discussion

2.3.1 Fabrication and characterization of graphene nanopores

Graphene was synthesized by chemical vapor deposition (CVD) of methane on an annealed Cu foil [39]. Raman spectroscopy on the as-synthesized graphene confirmed that it was a single-layer film (I_{2D}/I_G ratio of 2.7±0.1; **Figure 2.1**). The density of intrinsic defects in graphene was low (I_{2D}/I_G ratio of 0.08±0.03) [148]. Since the defect-free graphene is not permeable to water [149], we incorporated vacancy defects by exposing as-synthesized films to radiofrequency (RF) O_2 plasma for exposure periods of 1, 2, and 3 s. O_2 plasma generates energetic radicals that graft the graphene lattice with oxygen functional groups eventually leading to pore formation. In some cases, pore formation is also accelerated by directly knocking out the carbon atoms from the lattice [150]. Exposure to O_2 plasma at room temperature for a short time (1 s) is sufficient to incorporate Å-scale vacancy defects (or nanopores) allowing the transport of water molecules as well as light gas molecules [45,50,51]. Increasing the exposure time to plasma enlarges the pore size [45,50]. Therefore, nanopores created by plasma are interesting for studying water evaporation as a function of the nanopore size.

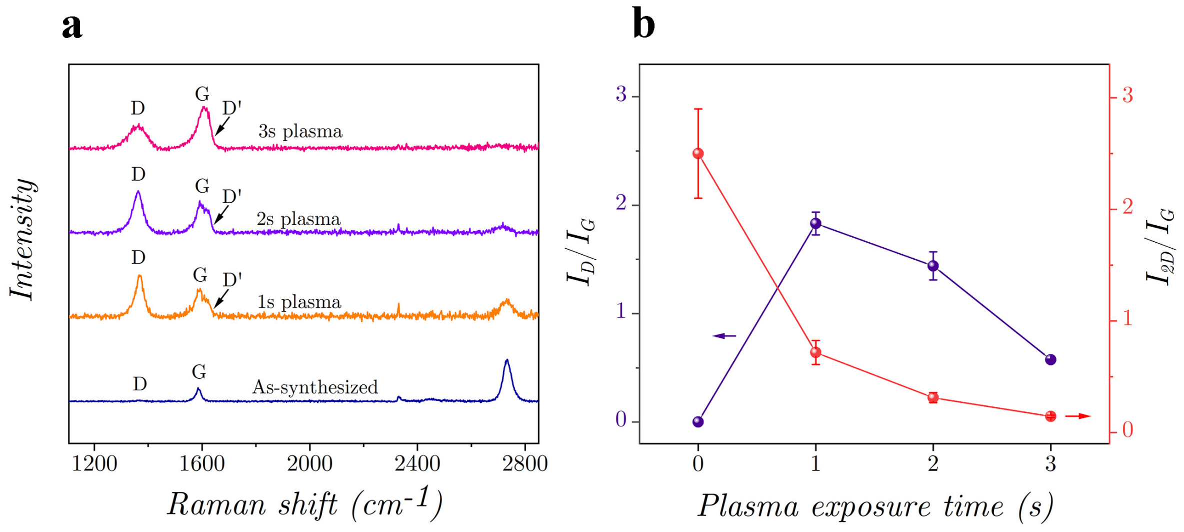

Figure 2.1. Raman characterization of O_2 plasma-treated nanoporous single-layer graphene (NSLG). (a) Raman spectra

of as-synthesized single-layer graphene and nanoporous single-layer graphene. (b) A plot of I_D/I_G AND I_{2D}/I_G as a function of plasma time.

Raman spectroscopy of plasma-treated graphene reveals the presence of significant D (at 1360 cm^{-1}) and D' (at 1620 cm^{-1}) peaks, known to be activated in the presence of defects in the graphene lattice (**Figure 2.1**). In particular, a low D/D' intensity ratio observed here (< 7) is associated with the incorporation of vacancy defects in the graphene lattice [151], which is further confirmed by the direct visualization of the porous lattice by aberration-corrected high-resolution transmission electron microscopy (AC-HRTEM, see discussion later). Since nanopores created by oxidative treatment involve oxygen functionalization [44,97,152], the pore edges are expected to be decorated with oxygen-functional groups. However, determining the exact nature of these functional groups has proven challenging. Given the importance of the pore edge functional groups in potentially influencing the water transport, we used X-ray photoelectron spectroscopy (XPS) to probe the functional groups in nanoporous graphene. The measurement was carried out after thermally annealing the plasma-treated graphene inside the XPS chamber to desorb the physisorbed ions and contaminants such as hydrocarbons and water. As a control, we also measured XPS data from the as-synthesized graphene without the plasma treatment. As expected, the as-synthesized graphene did not have any oxygen-functional group (**Figure 2.2**). In contrast, we could deconvolute the C1s peak in the plasma-treated sample (3s plasma, **Figure 2.3a**) where the positions of the deconvoluted peaks are consistent with the presence of ether/epoxy (C–O, 286 eV) and semiquinone (C=O, 288.3 eV) groups [153]. Based on the peak intensity, the overall concentration of functional groups was 6.7%. The relative composition of these functional groups can be analyzed by the O1s peak. However, it was challenging to deconvolute O1s because of the contribution from copper oxide from the catalytic Cu substrate for CVD, formed by the oxidation of Cu during the plasma treatment. To resolve this, we carried out the plasma treatment on freshly cleaved highly oriented pyrolytic graphite (HOPG) where the atmospheric contaminants were removed by annealing the samples inside the XPS chamber. Deconvolution of the resulting spectra indicates 31% ether, 62% epoxy, and 7% semiquinone (**Figure 2.3b**), which renders the overall composition of ether, epoxy, and semiquinone groups on the graphene lattice as 2.1%, 4.2%, and 0.5%, respectively.

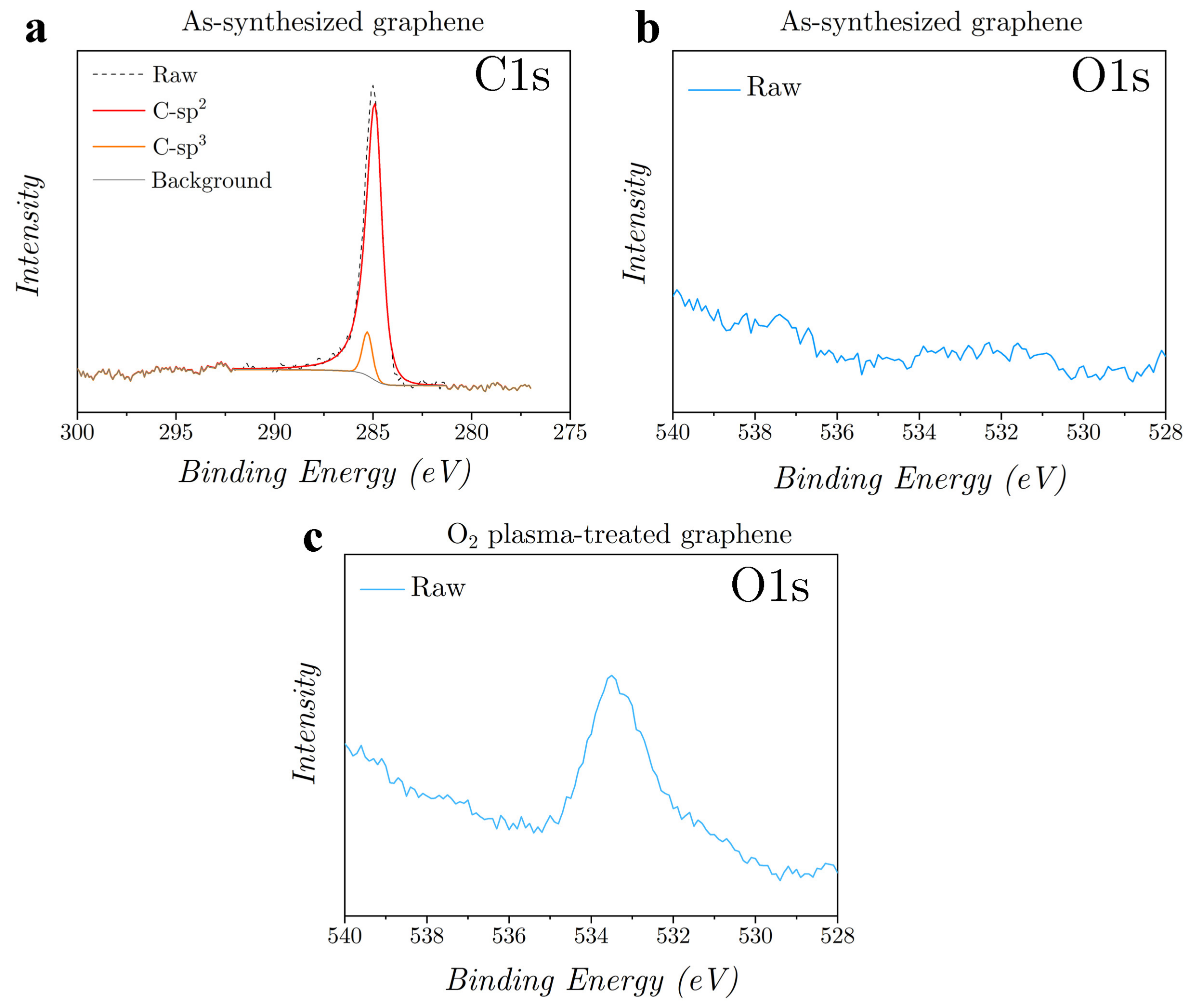

Figure 2.2. XPS spectra of graphene samples. (a) C1s spectrum of as-synthesized single-layer graphene. (b) O1s spectrum of as-synthesized single-layer graphene. (c) O1s spectrum of 3 s-oxygen-plasma-treated single-layer graphene.

Mechanistic studies on the evolution of defects in graphene indicate that semiquinone groups are generated as a result of C–C bond cleavage [154,155]. These groups are exclusively present at the pore edge. Based on the density of vacancy defects estimated by AC-HRTEM imaging ($\rho_{vacancies}$) and the concentration of semiquinone groups calculated by XPS (θ_{SQ}), one can estimate the number of semiquinone groups per pore, n_{SQ}, as follows:

$$n_{SQ} = \theta_{SQ} \times \frac{\rho_C}{\rho_{vacancies}} \qquad \textbf{(Equation 2.2)}$$

where ρ_C is the density of carbon atoms in the graphene lattice. Using **Equation 2.2**, for the 3 s plasma sample, n_{SQ} equals 7, confirming our previous assertion that a pair of semiquinone groups are created on the pore edge by the oxidative cleavage of C–C bond.

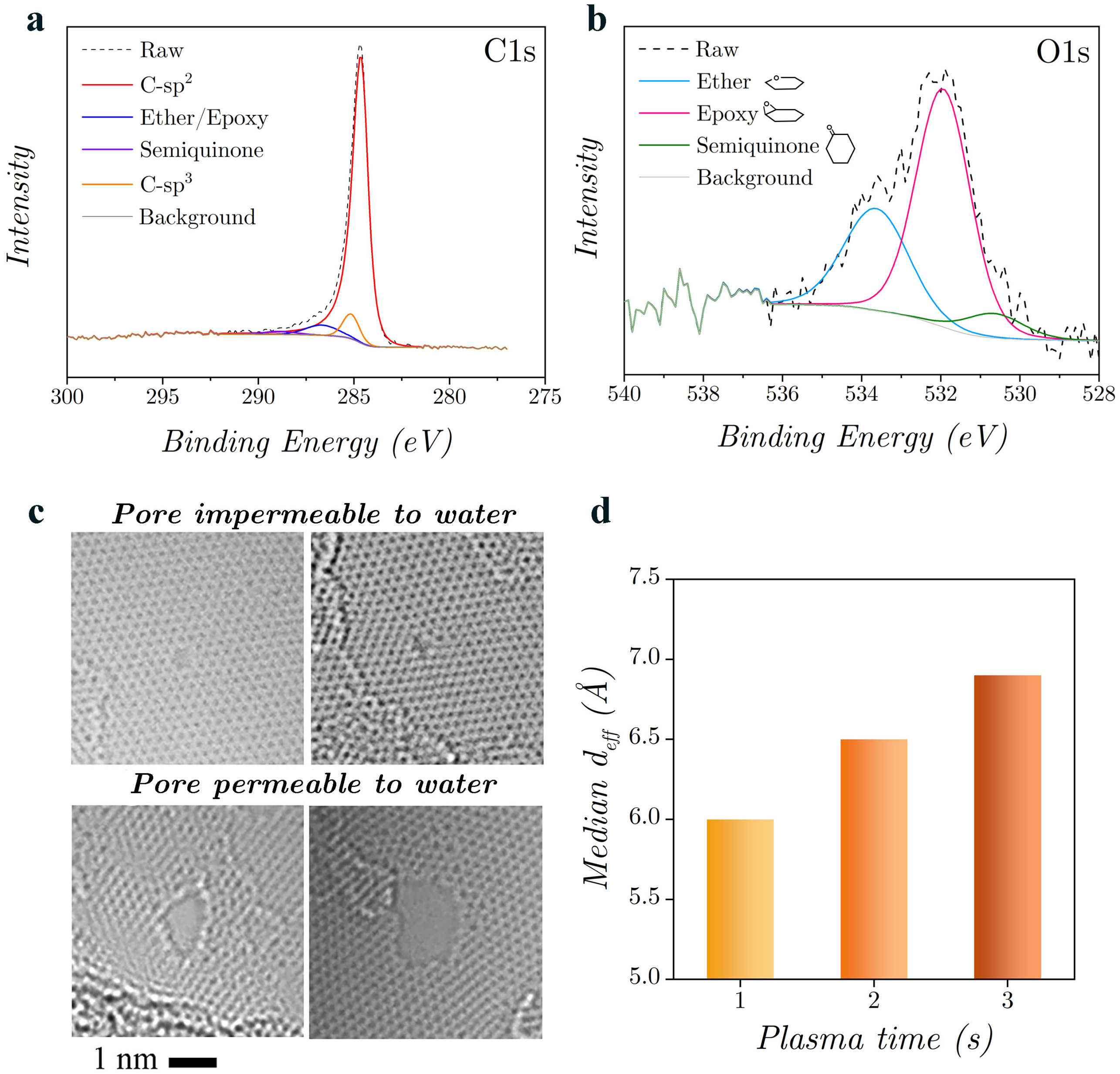

Figure 2.3. Characterization of graphene nanopores used to probe water transport. (a) C1s XPS spectra from graphene treated with 3 s O_2 plasma. (b) O1s XPS spectra of HOPG treated with 3 s O_2 plasma. (c) AC-HRTEM images of nanopores categorized as water-impermeable and -permeable pores. Scale bar: 1 nm. (d) Median d_{eff} of 1, 2, and 3 s plasma-treated graphene.

Aberration corrected high resolution transmission microscopy (AC-HRTEM) of graphene films treated with plasma was carried out to understand the density and size distribution of the carbon vacancies. It is extremely challenging to determine the precise structure of functionalized vacancy defects because (i) atmospheric, and graphene transfer-related contaminants tend to cover the defects, and (ii) electron beam tends to gasify oxygen functional groups. We recently showed that transferring graphene using a lacey carbon film followed by annealing at 900 °C in a reducing atmosphere inside an activated carbon bed is effective in removing the contaminants for imaging vacancy defects in HRTEM [131]. However, the high-temperature annealing treatment gasifies the oxygen functional groups. As a result, only bare nanopores devoid of functional groups could be visualized (**Figure 2.3c**). The removal of the functional groups also tends to coalesce nearby pores. Therefore, we note that pore size and porosity estimated by AC-HRTEM are an overestimate. Therefore, water vapor flux (vapor flow rate normalized to open area in graphene for evaporation where the open area is estimated by AC-HRTEM study), and corresponding enhancement reported in this study are underestimated.

Using AC-HRTEM, we analyzed the gap in the vacancy defects large enough for water transport by an effective pore diameter, d_{eff}, and the pore density of the plasma-treated samples (**Figure 2.4a**). The pore size was calculated by fitting the graphene lattice into the HRTEM images to count the number of missing carbon atoms as well as the largest possible circle inside the nanopores (**Figure 2.4b** and **Figure 2.5a**). The effective pore size available for the transport of water and small gas molecules (**Figure 2.4c**) was calculated by subtracting the effective van der Waals diameter of a carbon atom and the bond length of the semiquinone group at the pore edge using **Equation 2.3** and **2.4**,

$$d_{eff} = d_{HRTEM} - 2bl_{C=O} - \frac{r_{C,vdw}}{\sqrt{2}} \qquad \textbf{(Equation 2.3)}$$

$$d_{HRTEM} = \sqrt{\frac{4A}{\pi}} = \sqrt{\frac{4N_C}{\pi\rho_C}} \qquad \textbf{(Equation 2.4)}$$

where N_C is the number of missing carbon atoms as determined by AC-HRTEM images, $bl_{C=O}$ is the bond length of the semiquinone group (1.2 Å), and $r_{c,vdw}$ is the van der Waals radius of carbon (~2.4 Å) [77].

We observe nanopores that are both smaller and larger than the size of the water molecule which has a kinetic diameter of 2.65 Å (**Figure 2.5b**) [156]. In this study, we only consider pores that are bigger than water molecules as smaller nanopores are impermeable to water. The distribution of d_{eff} is skewed to the right, which is expected when one generates nanopores by oxidative treatment where nucleation and pore expansion are concomitant [157]. However, a clear trend in d_{eff} can be observed; the median d_{eff} increases for the longer plasma time (6.0, 6.5, and 6.9 Å for 1, 2, and 3 s, plasma, respectively), consistent with the extended pore expansion with the longer plasma time (**Figure 2.3d**).

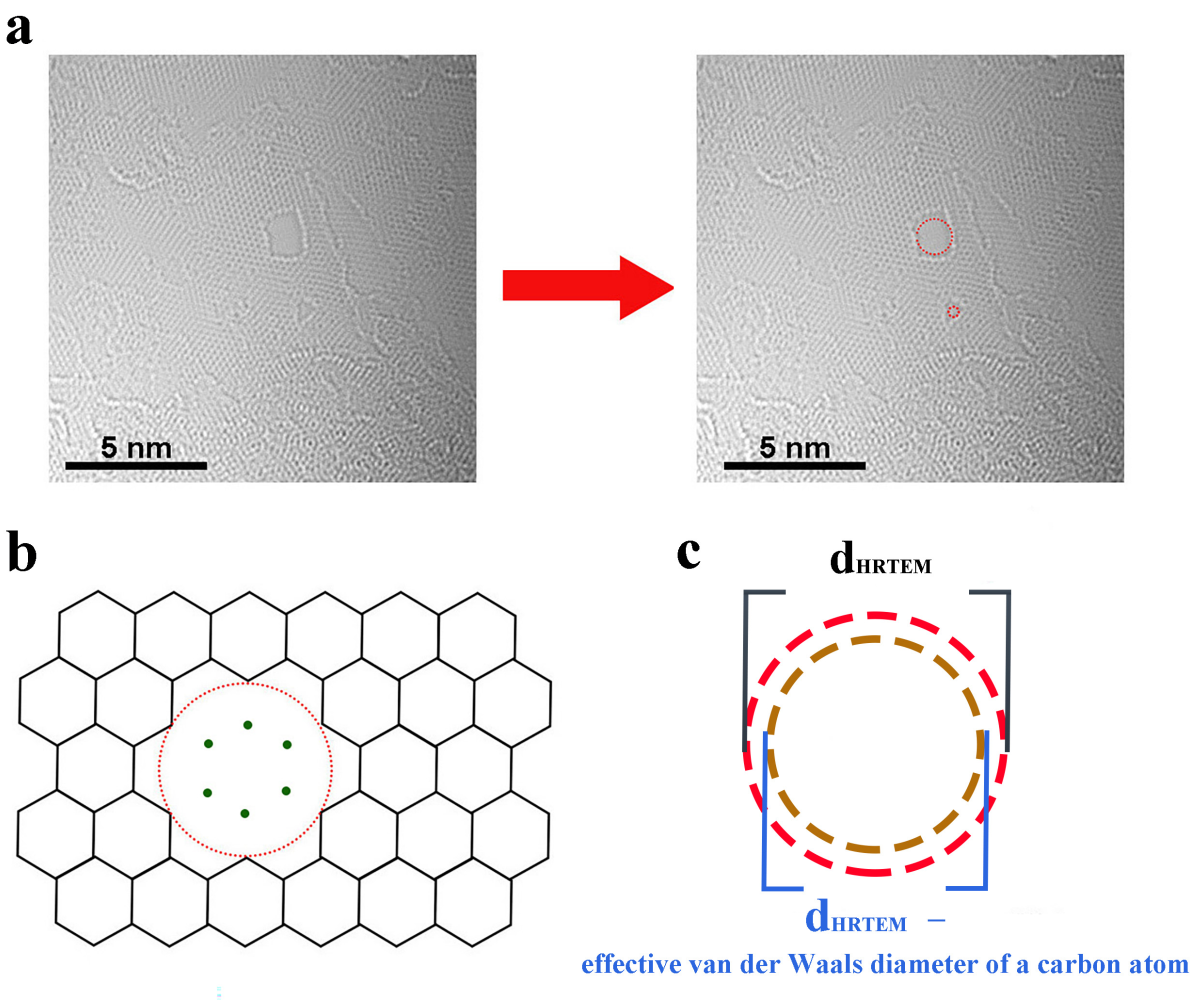
a
5 nm
5 nm
b
c
d_HRTEM
d_HRTEM −
effective van der Waals diameter of a carbon atom

Figure 2.4. Pore analysis by AC-HRTEM. An example of (a) AC-HRTEM image showing nanopores and its counterpart after (b) counting the number of missing carbon atoms (green dots), fitting the biggest possible circle in the nanopores, and (c) a schematic explaining the difference between the measured pore size from HRTEM images and the effective gap for water transport.

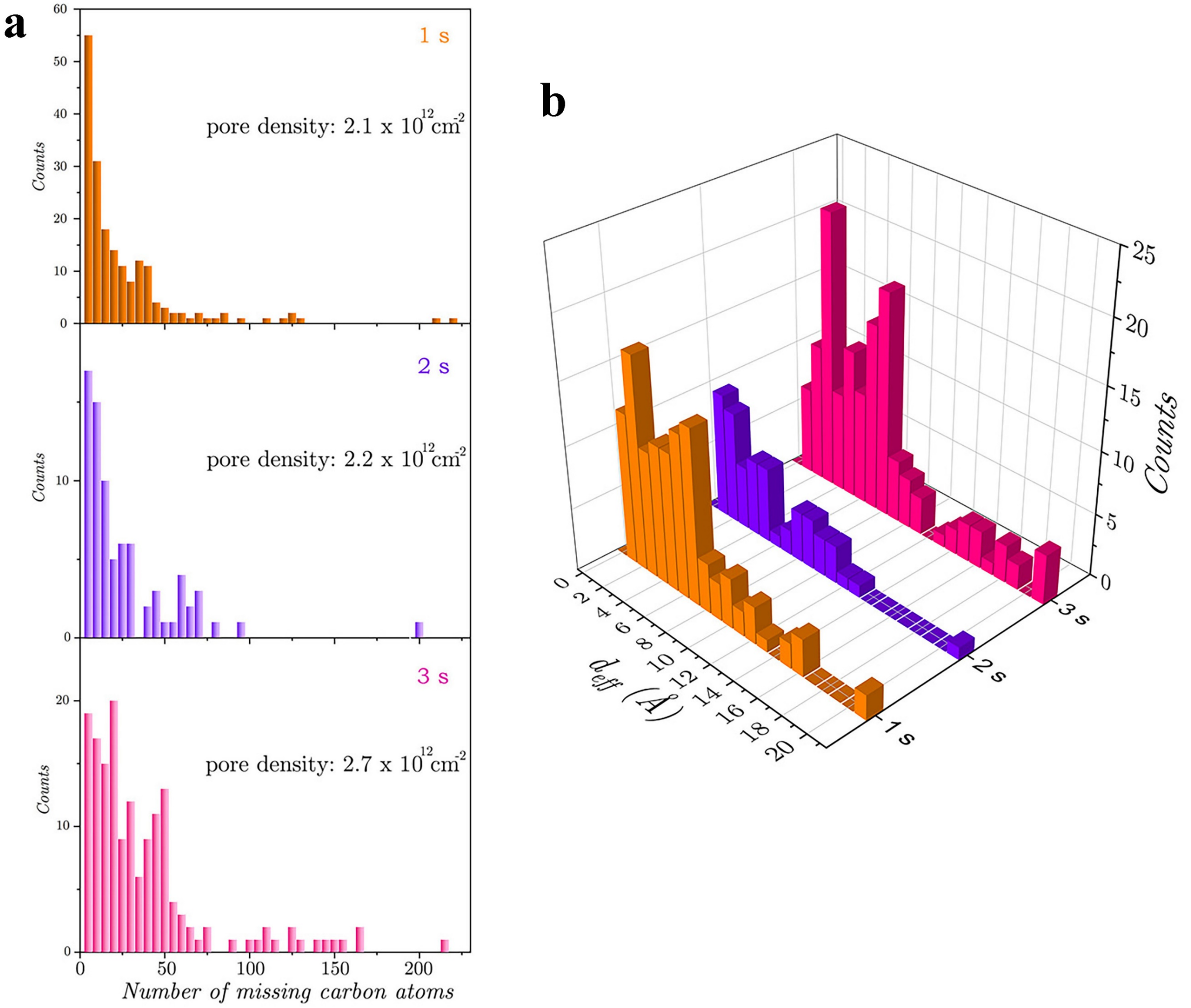

Figure 2.5. Pore size distribution analysis. (a) Pore size distribution (PSD) in terms of missing carbon atoms for different plasma treatments. (b) PSD of d_{eff} for different plasma treatments.

2.3.2 Water vapor transport

Next, to probe the evaporation of water, the porous graphene film was transferred on a porous W foil hosting an array of 5-μm-sized holes over a mm^2 area. To prevent cracks and tears in graphene during the transfer and during the transport study, graphene was mechanically reinforced with a 200-nm-thick nanoporous carbon (NPC) film hosting much larger pore opening of 20–30 nm [130]. We refer to this film as the support film. The W foil-supported graphene/support film was subsequently annealed at 500 °C to improve the adhesion of the film with the foil (**Figure 2.6**), without which the film had the tendency to peel off in the presence of water. The hydrophilic nature of the support film (contact angle ~59 degree) allowed wetting of the film with liquid water enabling us to successfully conduct the evaporation experiments. For measuring the evaporation flux, the film was sealed inside a stainless-steel module, and liquid water was loaded on the side of the support film (**Figure 2.7a**). The other side (vapor-side) of the film was connected to a vapor collection chamber with volume *V*, maintained at a low pressure (0.5–0.6 Torr) with a vacuum pump. To initiate the measurement of water vapor evaporation rate, the collection chamber was isolated from the vacuum pump at a set time which allowed the accumulation of water vapor in the collection chamber, witnessed by a rise in the chamber pressure. The time-dependent and linear rise in the chamber pressure, *P*, from the accumulation of water vapor in the chamber was used to calculate the evaporation rate, *dN/dt* (unit: mol/s, **Equation 2.5**).

$$\frac{dN}{dt} = \frac{V(dP/dt)}{RT} \qquad \textbf{(Equation 2.5)}$$

where *R* is the universal gas constant, and *T* is the temperature.

Equation 2.5 can be used to calculate the accumulation of water vapor in the collection chamber since *P* in the chamber increases linearly to 2 Torr and water vapor can be treated as an ideal gas at pressure below ~ 78 Torr with an error less than 0.3% [158].

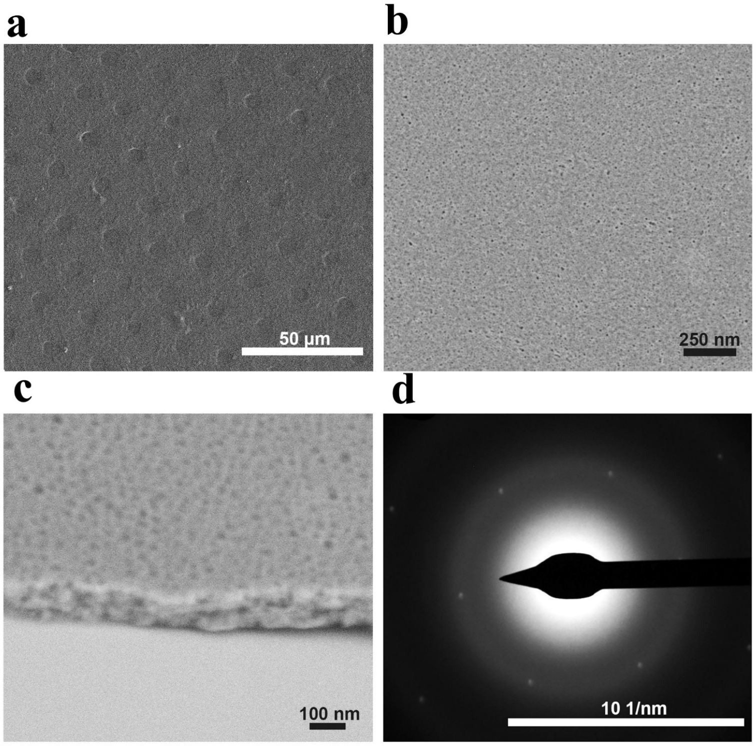

Figure 2.6. Characterization of nanoporous graphene/support film. (a) SEM image of graphene/support film suspended on a macroporous tungsten support, (b) Top-view SEM image, (c) cross-section SEM image, and (d) SAED of the film.

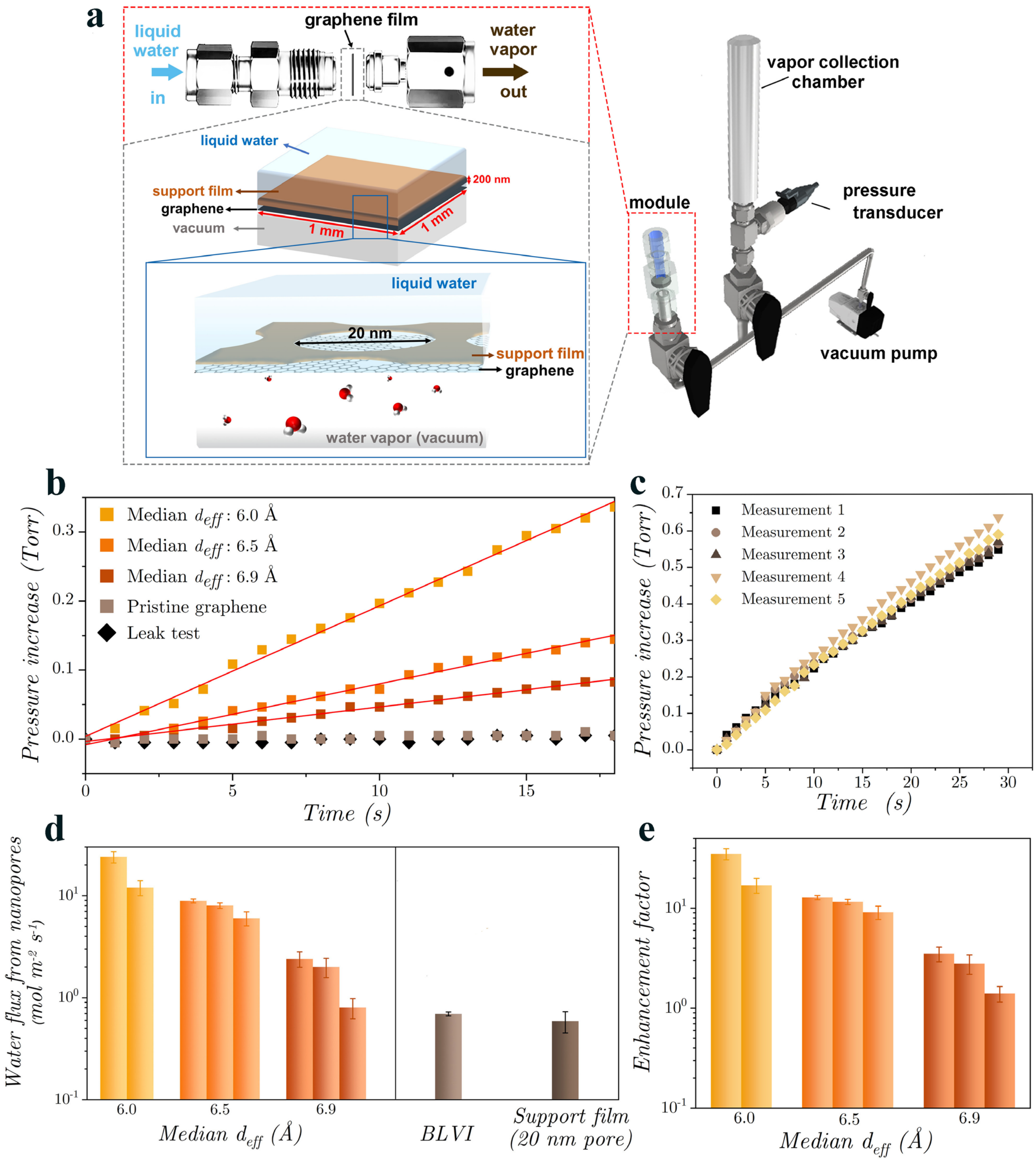

Figure 2.7. Water evaporation data from graphene nanopore compared to that from BLVI and the support film. (a) Schematic of the water permeation setup and water permeation through the support film, nanoporous graphene, and eventually in a vacuum. (b) The raw data of water permeation tests from nanoporous graphene devices. The R^2 values of each linear regression are 0.998, 0.99, and 0.992, for median d_{eff} of 6.0, 6.5, and 6.9 Å, respectively. (c) Five measurements on the same graphene film, PG-1. (d) Water flux from nanopores of each film, and their comparison with BLVI and the support film, NPC

(20–30-nm-sized pore opening) at 22 °C. From left to right, the columns denote PG-1 to PG-8. (e) Comparison of evaporation enhancement between each nanoporous graphene device at 22 °C. The enhancement factor is defined as the ratio of water flux from nanopores of a graphene device to the water flux from the BLVI. Error bars in (c) and (d) represent the standard deviation of three (BLVI) or five measurements (graphene films and support film).

The measurement of the water evaporation rate by the above protocol allowed us to study evaporation in a regime where the external mass transfer of water vapor is not the rate-limiting step. On the liquid water side, the supply of water to the graphene interface was orders of magnitude higher than the evaporation rate in these conditions (**Appendix 2.5.1**), thanks to the capillary-pressure-driven flow of liquid water in 20–30-nm-sized pores in the support film, and much higher porosity of the support film (50–60 %) compared to that in graphene (0.4–1.3 %, estimated from AC-HRTEM images). Therefore, the supply of liquid water to the evaporation front was also not the rate-limiting step [16,56]. It is reported that the heat-transfer limitation in evaporation becomes negligible compared to the interfacial evaporation kinetics when using a material with a thermal conductivity, *k*, much larger than that of the working liquid [159]. Therefore, the use of a stainless-steel module in this study ensures that the evaporation is not limited by heat transfer from the surroundings because of an order of magnitude higher thermal conductivity of stainless steel compared to water. [160–163]. Thus, the transport of energy to the interface was also not the rate-limiting step in our study. We used the same stainless-steel module for BLVI, support film and the graphene film with only one exception that graphene and support film had area of 1 mm^2 whereas the area of BLVI was 133 mm^2 to ensure a reliable measurement (**Figure 2.7a** and **Figure 2.8a**; see details in section **2.2.7**).

We prepared 2–3 porous graphene films for each plasma condition (total 8 films, referred to as PG-1 to PG-8). Before water evaporation tests, we ensured the integrity of the films by pressurizing them with H_2 and measuring the gas transport. Only devices which showed no signs of tears or cracks, marked by orders of magnitude lower gas flow rate from porous graphene compared to the support film, were used for the water evaporation study. A comparison of the gas transport data on a specimen before and after the water evaporation test revealed that there were no significant differences in the gas transport properties (**Figure 2.9b**), confirming that the nanopores did not expand during the evaporation study. This was also supported by O1s XPS spectrum showing that the composition of oxygen-functional groups did not change after exposure to water in a typical water evaporation condition (**Figure 2.9a**).

Before each water evaporation experiment, a leak test was performed by isolating the collection chamber from the vacuum pump and the module containing nanoporous graphene. We did not witness any significant rise in the pressure of the collection chamber during this test, indicating a negligible leak into the chamber from the atmosphere (**Figure 2.7b**). In contrast, when the graphene module was not isolated while the vacuum pump was isolated, the pressure in the chamber rose sharply with a near-constant rate with respect to time. The near-constant rate in these measurements is driven by the fact that the driving force for evaporation, the difference between the saturation vapor pressure of water (24 Torr) and the vapor pressure in the chamber (0.5–2 Torr), does not change significantly.

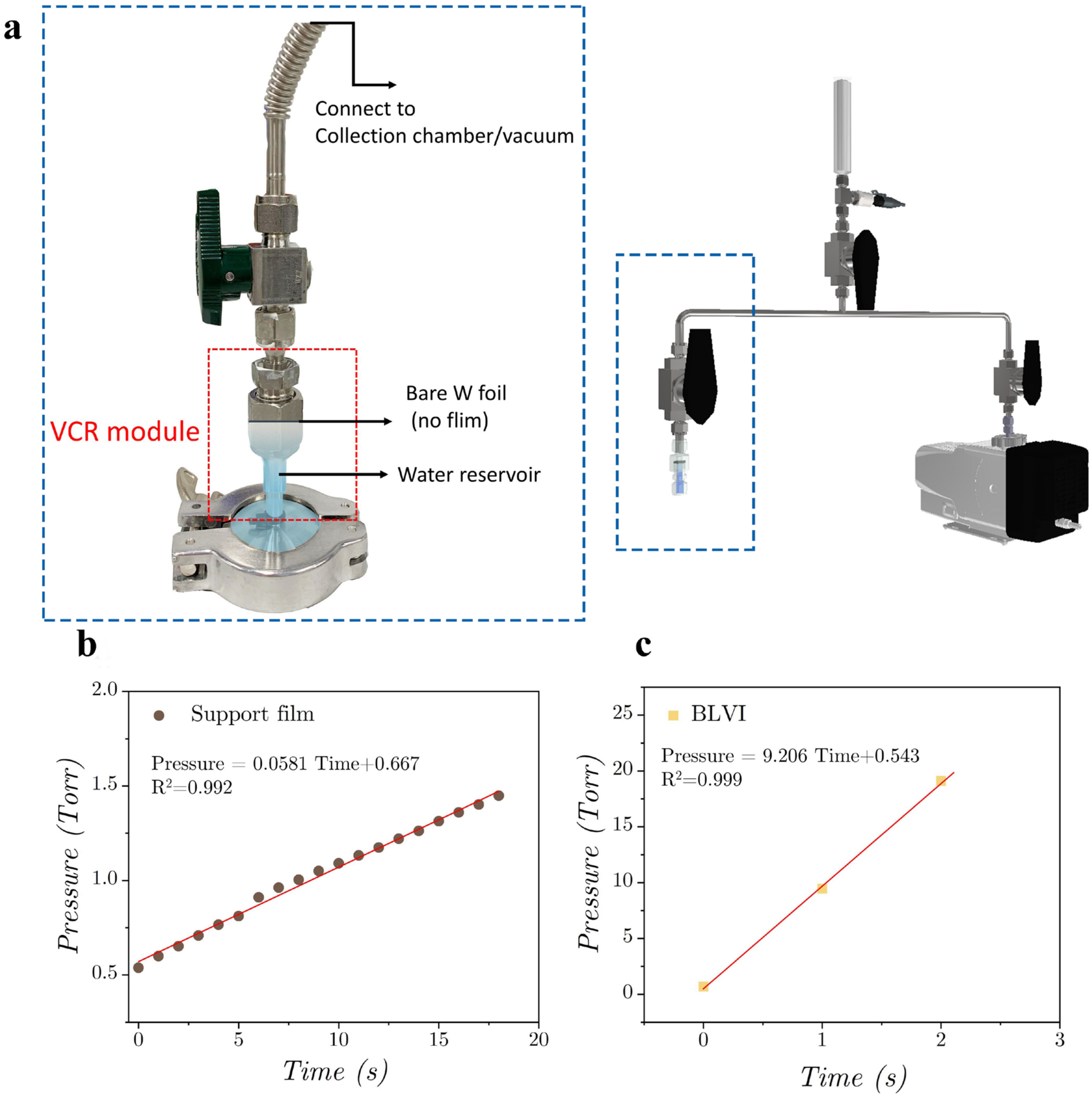

Figure 2.8. The setup and raw data of water permeation tests. (a) The water cell used in the measurement of the BLVI. Pressure versus time measured from the (b) the support film and (c) the BLVI.

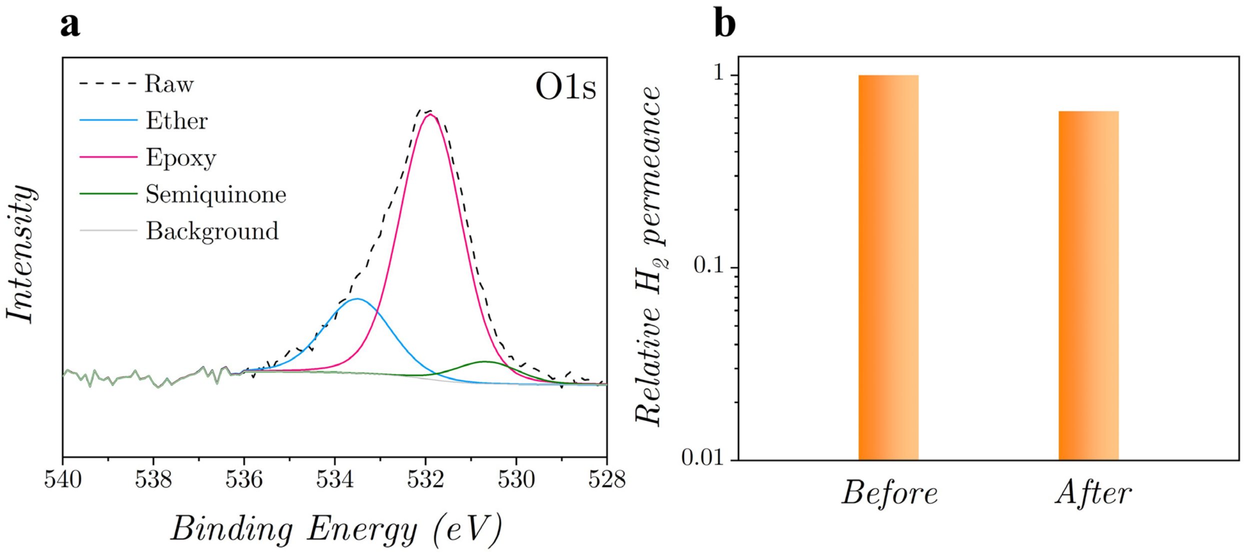

Figure 2.9. Characterization of HOPG/nanoporous graphene after evaporation. (a) O1s spectrum of HOPG after water evaporation. Oxygen-plasma-treated HOPG was first immersed in a water bath and subsequently, the water evaporation on the HOPG surface was carried out under vacuum. We then dried the HOPG and thermally annealed the plasma-treated HOPG inside the XPS chamber to desorb the physisorbed water and contaminants. (b) Gas permeance of PG-2 measured at 100 °C before and after the water evaporation measurement.

We obtained an effective evaporation flux from BLVI of 0.69±0.04 mol m^{-2} s^{-1} at bulk liquid temperature of 22 °C (**Figure 2.8c**). This flux is consistent with BLVI flux reported in literature using reservoir made up of stainless-steel container and using evacuation to induce evaporation (**Table 2.1**). Additionally, the flux from the bare support film (0.59±0.14 mol m^{-2} s^{-1}) was close to that of BLVI indicating that 20 nm pores of support film do not yield enhancement. This contradicts the literature on enhancement from a similar sized nanopore [16]. This is attributed to the lack of an extended meniscus in our millimeter-scale liquid-vapor interface created by the support film in contrast to the literature where a single nanopore with finite depths creates the presence of an extended meniscus (also see discussion in the MD simulation section).

Table 2.1. BLVI reported in the literature and in this study.

Reservoir Material	Pressure in the vapor phase (Pa)	Evaporation flux (mol m^{-2} s^{-1})	Reference
Stainless steel	247.5	0.19	[164]
Stainless steel	258.6	0.23	[163]
Stainless steel	256	0.19	[162]
Stainless steel	228.1	0.36	[161]
Stainless steel	80.2	0.70	This study

To understand the effective evaporation enhancement contributed by graphene nanopores at the liquid-vapor interface, we used **Equation 2.6** to estimate water flux and compared it to the corresponding value from the BLVI (**Figure 2.7c**).

$$\text{Water flux from nanopores}\left(\frac{mol}{m^2 s}\right) = \frac{\text{Evaporation rate}(mol/s)}{\text{Pore area}(m^2)} \qquad \textbf{(Equation 2.6)}$$

Here the pore area, A_{tot}, was estimated by the size distribution of d_{eff} (**Figure 2.5b**) and could be calculated using **Equation 2.7**:

$$A_{tot} = \sum_{d_{i,eff} > d_{water}} \rho f_i \frac{\pi d^2_{i,eff}}{4} \qquad \textbf{(Equation 2.7)}$$

where f is the relative frequency of each observed pore, ρ is the pore density estimated by the AC-HRTEM study. We only consider pores whose d_{eff} is larger than the kinetic diameter of water, d_{water} (0.26 nm). The calculated porosities were 0.42 %, 0.44 %, and 1.3% for samples having median d_{eff} of 6.0 Å, 6.5 Å, and 6.9 Å, respectively.

Compared to the measurement of evaporation flux from the BLVI, we found that the evaporation fluxes from graphene nanopores were remarkably enhanced (**Figure 2.7c**). The water evaporation fluxes from two separate nanoporous graphene samples (PG-1 and PG-2) with median d_{eff} of 6.0 Å were 24±3 and 12±2 mol m^{-2} s^{-1} (**Figure 2.7c**), corresponding to enhancements of 35±4 and 17±3, respectively (**Figure 2.7d**). The fluxes of the other set of nanoporous graphene samples (PG-3, PG-4, PG-5) with a slightly larger median d_{eff} of 6.5 Å were comparatively lower (8.9±0.4, 8±0.5, and 6±0.9 mol m^{-2} s^{-1}, **Figure 2.7c**), corresponding to enhancements of 13±0.6, 12±0.7 and 9.1±1.4, respectively (**Figure 2.7d**). The fluxes from the samples (PG-6, PG-7, PG-8) with the largest median d_{eff} (6.9 Å) were the lowest (2.4±0.4, 2±0.4, and 0.94±0.18 mol m^{-2} s^{-1}, **Figure 2.7c**), corresponding to enhancements of 3.5±0.6, 2.8±0.6, and 1.3±0.25, respectively (**Figure 2.7d**). Overall, we observed enhanced water evaporation fluxes for all nanoporous graphene samples considered in this study, with enhancement increasing for smaller nanopores. We finally point out that although it is customary to use the Hertz-Knudsen and its variants to characterize evaporation, we refrain from using this formulation due to the underlying equilibrium framework used while deriving the Hertz-Knudsen relation [108,165].

While the water evaporation rate decreased for increasing pore size, the H_2 transport rate showed a reverse trend, i.e., it increased for the larger pores (**Figure 2.10**). The latter is consistent with the gas transport mechanism, i.e., hydrogen flow is proportional to the pore area (**Equation 2.8**) [69,77].

$$j_{H_2} = A_P \frac{\Delta P}{\sqrt{2\pi m k_B T}} \qquad \textbf{(Equation 2.8)}$$

where P is the feed pressure, m is the mass of H_2, A_P is the area of the pore, k_B is the Boltzmann constant and T is the temperature.

The increased water evaporation fluxes from the ensemble of nanopores with the smallest median d_{eff} indicate a strong role of nanopore edge-driven confinement effects on interfacial water that controls the evaporation flux. Next, to understand the observed enhancement, we carried out MD simulations on water evaporating from graphene nanopores.

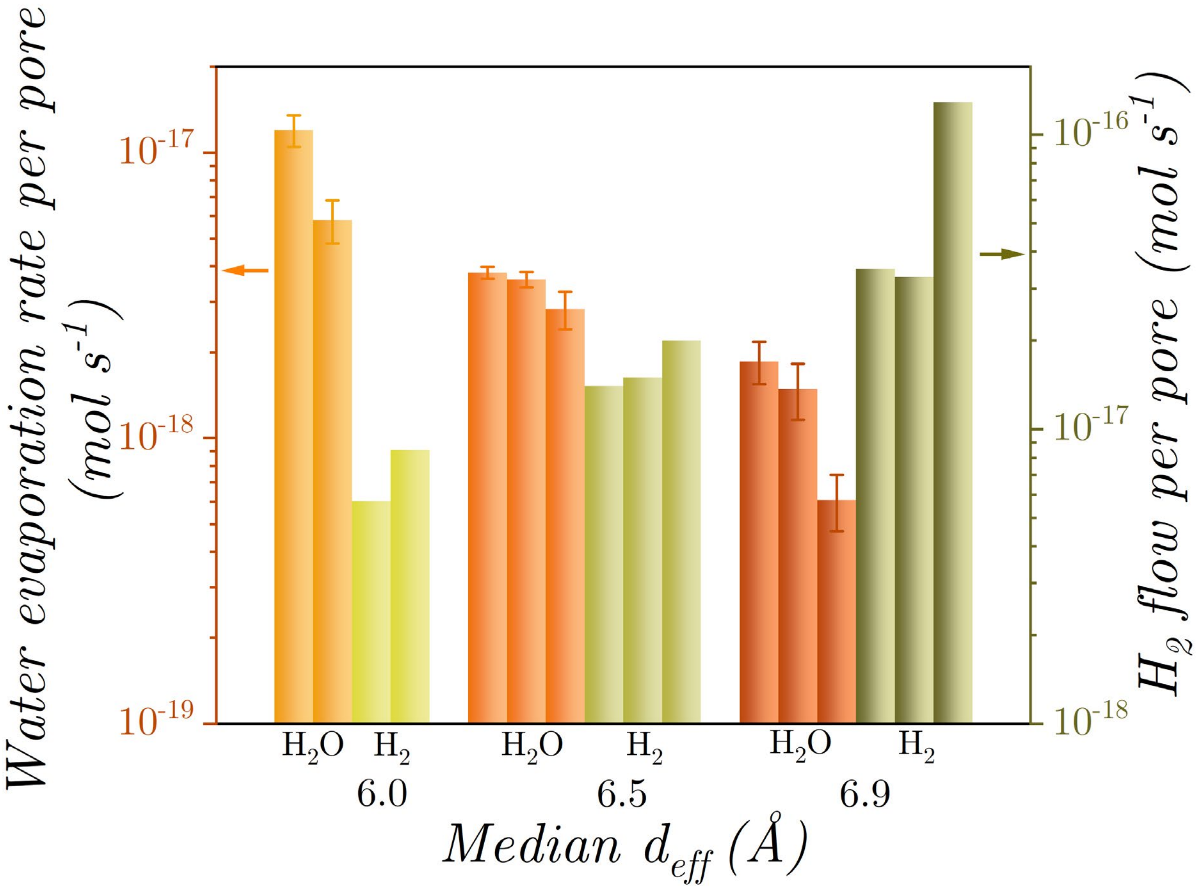

Figure 2.10. Analysis of water evaporation rate per pore, and H_2 flow rate per pore of different graphene films. Mass flow per pore of water vapor (22 °C) and H_2 from each nanoporous graphene device (25 °C) as a function median d_{eff}. From left to right, the columns denote PG-1 to PG-8.

** The simulation work was performed by Anshaj Ronghe and K. Ganapathy Ayappa from Indian Institute of Science, Bangalore.*

2.3.3 System details for molecular dynamics simulations

We simulated four different sized nanopores by removing 16, 22, 52, and 94 carbon atoms from the pristine graphene [69], which are referred to as type-0, 1, 2, and 3 nanopores, respectively. The carbon atoms on the nanopore edges were terminated with hydrogen atoms (H), ether (ET), and hydroxyl (OH) (**Figure 2.11a**) to study the effect of pore-edge functional groups on the water evaporation flux. Density functional theory (DFT) calculations revealed that the nanopore edges alternately terminated with H atoms, and the oxygen-functional groups had the lowest formation energies (**Appendix 2.5.2**). d_{eff}, based on the diameter of the largest van der Waal sphere that can be accommodated in the functionalized nanopore [166], are listed in **Table 2.2**. All-atom MD simulations to study the evaporation through the functionalized nanoporous graphene (FNPGs) were carried out with a TIP4P-Ew [143] water bath and an attractive pristine graphene surface (attractive wall) placed 8 nm away from the FNPG (**Appendix 2.5.3**) is used to capture evaporated water molecules (**Figure 2.11d**).

2.3.4 Evaporation flux of water molecules

The water evaporation flux, j (molecules nm^{-2} ns^{-1}), at 25 °C (**Figure 2.11e**) was evaluated from the slopes of the net number of water molecules exiting the nanopores (**Appendix 2.5.3**). In the absence of FNPG, the evaporation flux from a BLVI interface was 0.081 molecules nm^{-2} ns^{-1}, in good agreement with the value of ~ 0.085 molecules nm^{-2} ns^{-1} predicted by Julin *et al.* [167] for the TIP4P-Ew water model at 27 °C. In the presence of FNPG, the water evaporation flux increased monotonically with decreasing d_{eff} (**Figure 2.11e**), irrespective of the nanopore functionality, consistent with our experimental findings. Interestingly, the presence of oxygen functional groups enhanced the evaporation flux. The greatest enhancement with respect to BLVI was ~13.3-fold, observed for the smallest OH-terminated nanopores (OH–0) with a flux of 1.081±0.002 molecules nm^{-2} ns^{-1} (**Table 2.3**). For the largest nanopores, the flux approaches the BLVI flux. The observed enhancement factors in the simulations are in the same order of magnitude as those observed in the experiments (**Figure 2.7e**). In experiments, while ether and semiquinone functional groups (C=O) are present substantially at the pore edge, epoxy functional groups are found to be barely present at the pore edge [97,153]. Therefore, in addition to the functionalized nanopore flux data reported here, we also carried out simulations with edges functionalized with semiquinone functional groups for $d_{eff}=0.345$ nm ($j=0.844\pm0.003$ molecules nm^{-2} ns^{-1}) and 0.461 nm ($j=0.701\pm0.002$ molecules nm^{-2} ns^{-1}) and found that the fluxes were between the values obtained for the OH and ether groups.

In order to explain this increase in the water evaporation flux, we focused our attention on properties of water molecules present in the cylindrical volume adjacent to the nanopore, as shown in **Figure 2.11f** and **g**. The length, l, of this cylindrical volume is equal to the thickness of the first hydration layer of FNPG (**Figure 2.11h**), and its diameter is equal to d_{eff}. We refer to these cylindrical regions as the region of interest (ROI) in the forthcoming sections. For BLVI, we focused our attention on properties of water molecules present in the "10-90" interface (**Appendix 2.5.3**) which describes the density change from 90% to 10% of the bulk water density.

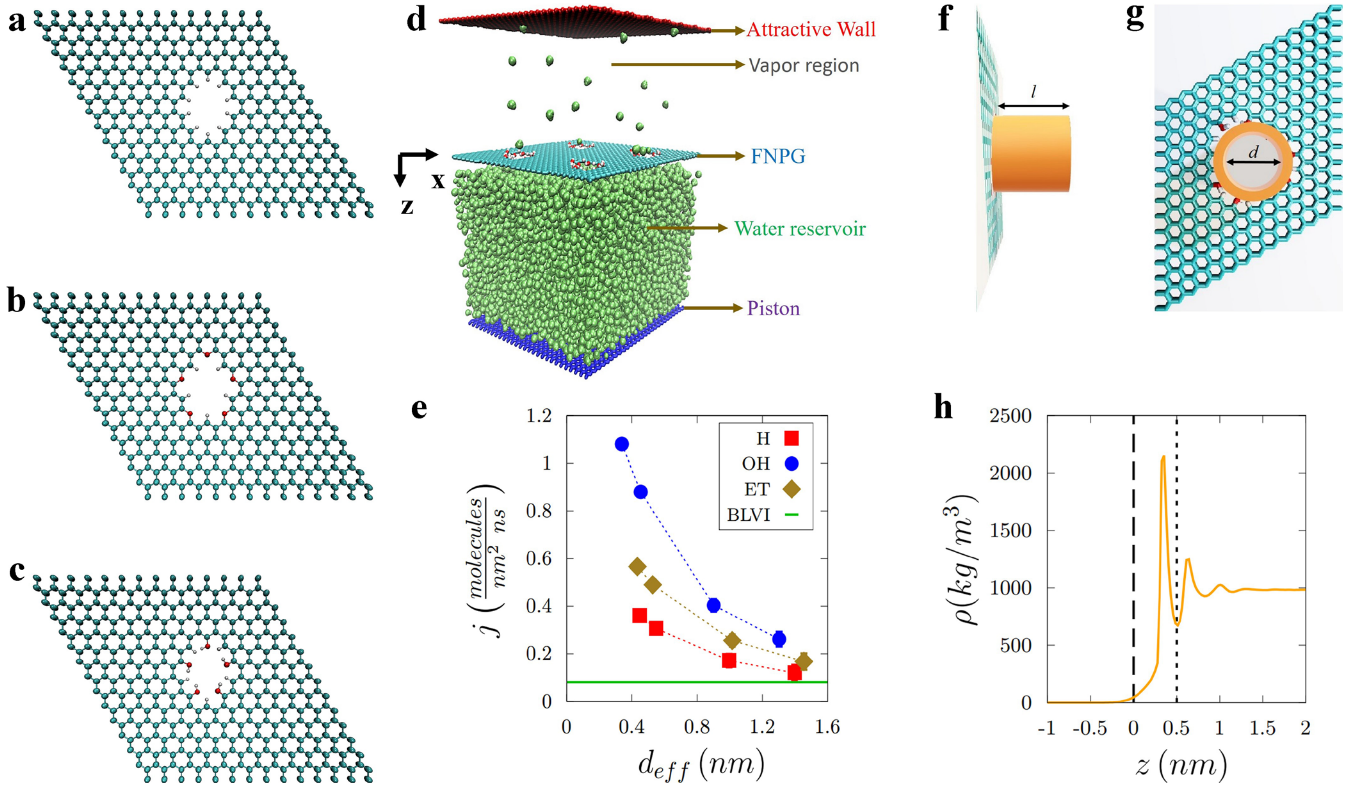

Figure 2.11. System details for MD simulations and evaporation flux from different FNPGs. Nanopores with 16 carbon atoms removed (type-0 nanopores) and nanopore edge terminated with H atoms (H–0) (a), ET and H (ET–0) (b) and OH and H (OH–0) (c). Each FNPG consists of four nanopores. (d) System configuration used to study water evaporation through FNPGs. (e) Evaporation flux of water molecules through different FNPGs. The standard error in mean of the reported flux values is very small (within 0.005 molecules nm-2 ns-1) and hence are not seen easily. (f) and (g) are the side and top views of the cylindrical volume considered for analyzing water properties. (h) Density profile of water molecules in contact with the FNPG located at $z = 0$ (black dashed line). $z > 0$ and $z < 0$ represent liquid and vapor regions, respectively. The location of the first hydration layer of thickness ~ 0.5 nm is also illustrated (black dotted line).

2.3.5 Hydrogen bond analysis, rotational dynamics, and translational dynamics

For the water molecules present in the ROI, HBs formed with the edge functional groups [168], and HBs formed between water molecules [169] were analyzed using a geometric criterion. Since OH functional groups can act as both HB donors and acceptors, their propensity to form HBs with water is greater when compared with the ET functional groups that can act only as HB acceptors (**Figure 2.12b–d**). For the H-terminated nanopores, the carbon atoms to which these H atoms are bonded are not sufficiently electronegative to form HBs with water, and we did not observe any HBs in this situation (**Figure 2.12a**). Nevertheless, the H-terminated FNPGs assist in breaking water-water HBs, albeit to a lesser extent via the asymmetry imposed upon the water molecules by the FNPG surface [170].

This enhancement of HBs with functional groups resulted in the greatest reduction in water–water HBs in the ROI of FNPGs terminated with OH functional groups (**Figure 2.12e**). We point out that the water molecules in the ROI for all FNPGs displayed a reduced number of HBs when compared with water molecules present in “10-90” interface (2.75±0.002). The presence of functional groups disrupts interactions between water molecules present in the ROI by breaking HBs between them (**Figure 2.12e**), allowing for a greater escape tendency through the nanopores. This trend correlates with the highest evaporation flux observed for OH-functionalized nanopores (**Figure 2.11e**), consistent with the increased disruption of HBs with decreasing nanopore size. For the smallest nanopore (type-0), water molecules in ROI interact mainly with the functional groups (**Figure 2.13**). A qualitatively similar increase in the evaporation flux has been observed by adding charges to the edge carbon atoms to mimic the presence of functional groups [83].

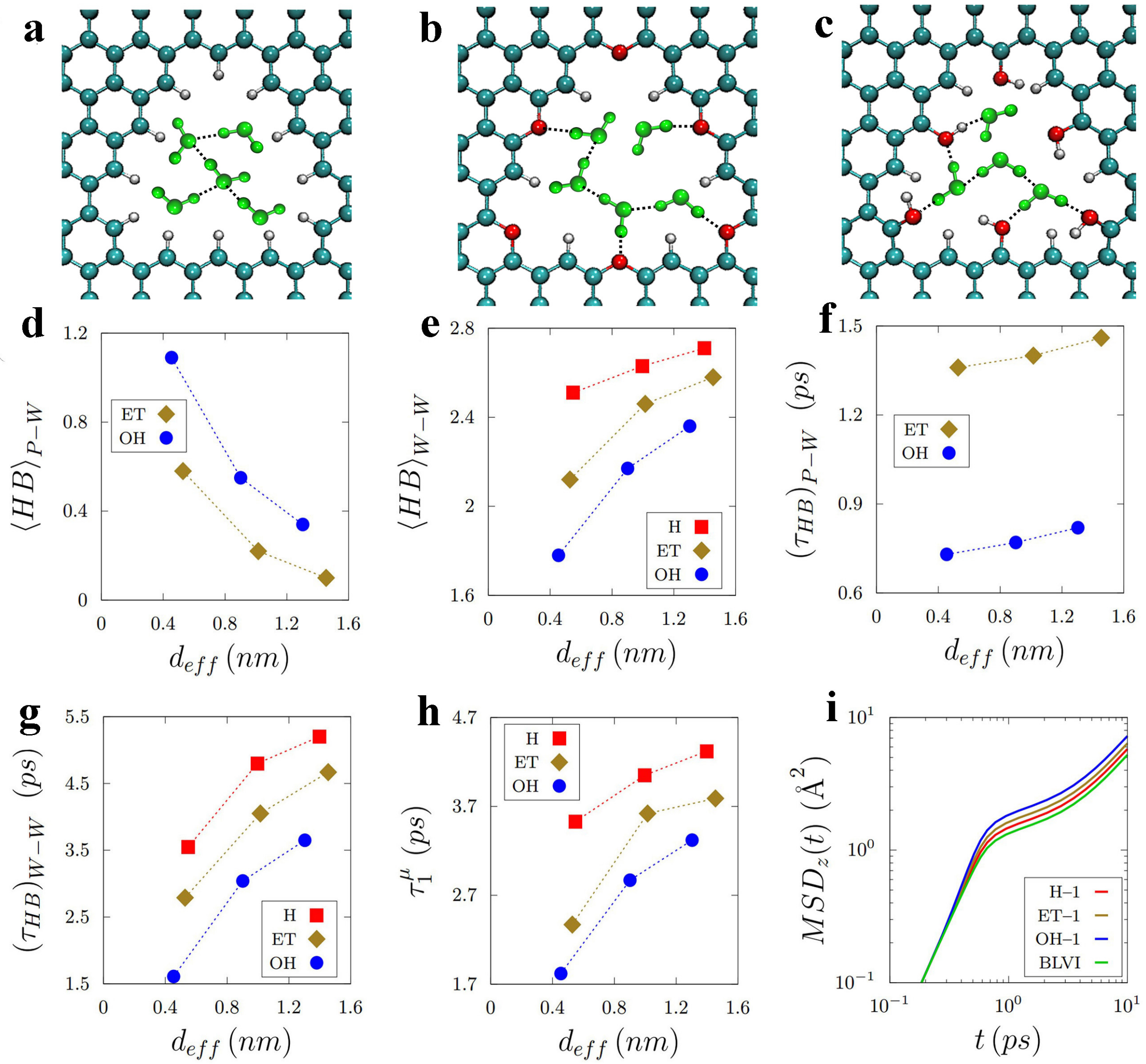

Figure 2.12. HB analysis for the functional group (pore)–water (P–W) pair and water–water (W–W) pair along with rotational dynamics and translational dynamics of water molecules present in the ROI of different FNPGs. (a), (b) and (c) show type-1 nanopores terminated with H atoms, ET and H, and OH and H, respectively. Water molecules (green) in the vicinity of the nanopores are shown along with the HBs (black dotted lines) between different pairs. (d) Average number of HBs per water molecule formed between functional groups terminating the nanopores and water molecules present in the ROI. (e) Average number of HBs per water molecule formed between the water molecules present in the ROI. The same for the water molecules present in the "10-90" interface of BLVI is shown for comparison. (f) Lifetime of HBs formed between functional groups terminating the nanopores and water molecules present in the ROI. (g) Lifetime of HBs formed between the water molecules present in the ROI. Lifetime of HBs formed between water molecules present in the "10-90" interface of BLVI is shown for comparison. (h) Dipole relaxation times of water molecules present in the ROI for *l* = 1. Dipole relaxation times of water molecules present in the "10-90" interface of BLVI is shown for comparison.

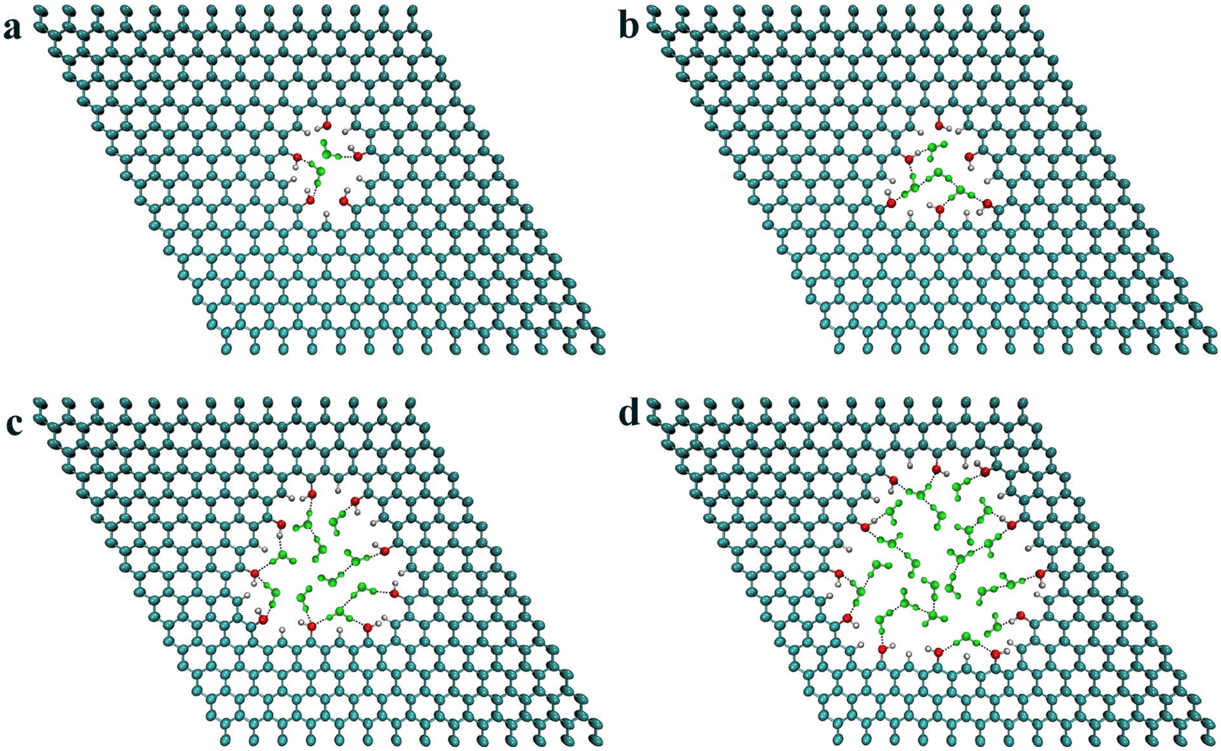

Figure 2.13. Interaction of water molecules with the functional groups and with other water molecules in the vicinity of the nanopore via HBs. (a), (b), (c), and (d) show type-0, 1,2, and 3, OH and H terminated nanopores, respectively. Water molecules (green) in the vicinityof the nanopores are shown along with the HBs (black dotted lines) between different pairs.

In addition to the number of HBs, the HB dynamics of water molecules in the ROI provides additional insight into the enhanced evaporation flux with decreasing nanopore size. From the intermittent HB correlation function, $C_{HB}(t)$ [171,172], we obtained HB lifetime, τ_{HB}, using a single exponential fit [172]:

$$C_{HB}(t) = A\exp(\frac{-t}{\tau_{HB}}) \qquad \textbf{(Equation 2.9)}$$

where A is a pre-exponential factor and t is time.

As compared to the water molecules present in the “10-90” interface of BLVI, water molecules present in the ROI of FNPGs show reduced number and reduced lifetime of HBs (**Figure 2.12f** and **g**). Lower τ_{HB} values revealed faster dynamics for HBs for the OH-terminated FNPGs when compared with the ET-terminated FNPGs. This trend was observed for functional group–water (**Figure 2.12f**) as well as water-water HBs (**Figure 2.12g**). The reduced τ_{HB} for the OH groups is partly due to the increased steric effects at the pore edge when compared with the ET groups (**Figure 2.12b and c**). Additionally, the lower τ_{HB}

for the water–water HBs (**Figure 2.12g**) correlates directly with the decreased water-water HBs in the ROI (**Figure 2.12e**). For a given pore functionality, the τ_{HB} values between water present in the ROI and the functional groups are relatively invariant with d_{eff}(**Figure 2.12f**). The observed τ_{HB} values are unique to the given functional group and water pair. The reduction in τ_{HB} is the greatest for FNPGs terminated with OH functional groups which effectively reduces the HB lifetimes. We point out that both the number of HBs and τ_{HB} play an important role in the escape probability of the water molecule. Smaller τ_{HB}, indicates shorter-lived HBs, resulting in faster HB dynamics to render enhanced evaporation fluxes (**Figure 2.11e**).

As another measure of the altered water dynamics and relaxation, we evaluated the dipole-dipole re-orientational dynamics by computing the first ($l = 1$) and second rank ($l = 2$) Legendre polynomials of the water dipole moment in the ROI as well as the corresponding dipole relaxation times, τ_l^{μ} (**Appendix 2.5.4**). τ_l^{μ} values for water molecules present in the ROI of different FNPGs are smaller than the τ_l^{μ} values of water molecules present in the "10-90" interface of BLVI (τ_1^{μ} = 4.67 ps and τ_2^{μ} = 1.70 ps) (**Figure 2.12h**). For a given pore diameter, the dipole relaxation times were lowest for the OH-functionalized pores and highest for the H-terminated pores (**Figure 2.12h**), reflecting the trends in the HB lifetimes (**Figure 2.12g**). Additionally, faster HB and dipole-dipole re-orientational dynamics were observed at the smaller nanopore sizes because of their tendency to effectively disrupt the interaction between water molecules in the ROI (**Figure 2.13**). The local water dynamics are dependent on the ability of the water molecule to both form and break HBs at a given instant [173,174]. Our results clearly reveal the presence of faster HB and dipole-dipole re-orientational dynamics for water in the ROI of the nanopores accentuated by edge functionalization with the greatest reduction in relaxation times observed for the OH-functionalized nanopores. The trends in these dynamic quantities are consistent with the enhanced evaporation flux with decreasing d_{eff} observed in experiments, where the increased presence of oxygen as either ET or epoxy and semiquinone at the nanopore edge was found to correlate positively with enhanced evaporation.

A direct dynamic measure of the propensity of a water molecule to exit the liquid-vapor interface can also be obtained from the variation of the mean square displacement (MSD) of water molecules along the z-axis of the ROI, illustrated for the FNPGs with type-1 nanopores in **Figure 2.12i**. Due to the limited spatial extent sampled in the z-direction, we did not attempt to extract a diffusion coefficient. However, the data clearly revealed the increased MSD_z for all nanopores relative to the MSD_z of water molecules present in the "10-90" interface of BLVI (**Figure 2.12i** and **Appendix 2.5.4**). Despite the limited extent of the distance sampled in the z-direction, the MSD_z plots for the water molecules present in the ROI for different FNPGs showed a distinct transition from the ballistic regime (where MSD scales as t^2) at short times to the diffusive regime (where MSD scales as t) at longer times. The relative increase in the MSDz with respect to water molecules present in the "10-90" interface of BLVI diminishes with increasing d_{eff} as expected (**Figure 2.13**).

2.3.6 Potential of mean force and surface tension analysis

The variation of the potential of mean force (PMF) for a water molecule along the z-axis of the ROI for different FNPGs are illustrated in **Figure 2.14a** and **b** for smallest (type-0) and largest (type-3) nanopores, respectively. A clear decrease in the free energy barrier for moving a water molecule from the bulk liquid (denoted as '*l*' in **Figure 2.14a**) to the vapor phase (denoted as '*v*' in **Figure 2.14a**) in the immediate vicinity (-1.5 nm $< z < 0$) of the FNPG when compared with the PMF for BLVI is observed (**Figure 2.14a** and **b**). The PMF values in the bulk vapor phase (denoted as '*bv*' in **Figure 2.14a**) are similar for the different systems reflecting the constant free energy difference for transferring a water molecule between the bulk liquid and the bulk vapor phases. From the PMF variations, we obtained the change in Gibbs free energy ($\Delta G = G_v - G_l$) for transferring a water molecule from the liquid phase ('*l*') to the vapor region ('*v*'). In all the FNPG systems we observed a reduction in ΔG when compared with the value of $\Delta G = 29.9$ kJ/mol obtained for evaporation from a BLVI (**Figure 2.14c**). We saw the lowest ΔG values for type-0 nanopores with the smallest $\Delta G = 22.1$ kJ/mol for OH–0 nanopores (**Table 2.4**). The free energy difference decreases with increasing d_{eff}, primarily due to the ineffectiveness of larger pores in disrupting water-water HBs (**Figure 2.13**). However, even for the largest nanopore studied, ΔG values were slightly smaller than the BLVI values, approaching the BLVI values for the largest H-terminated pores (**Figure 2.14c**). The variations in ΔG (**Figure 2.14c**) are consistent with the enhanced evaporation observed for the OH-, ET- and H-terminated nanopores (**Figure 2.11e**).

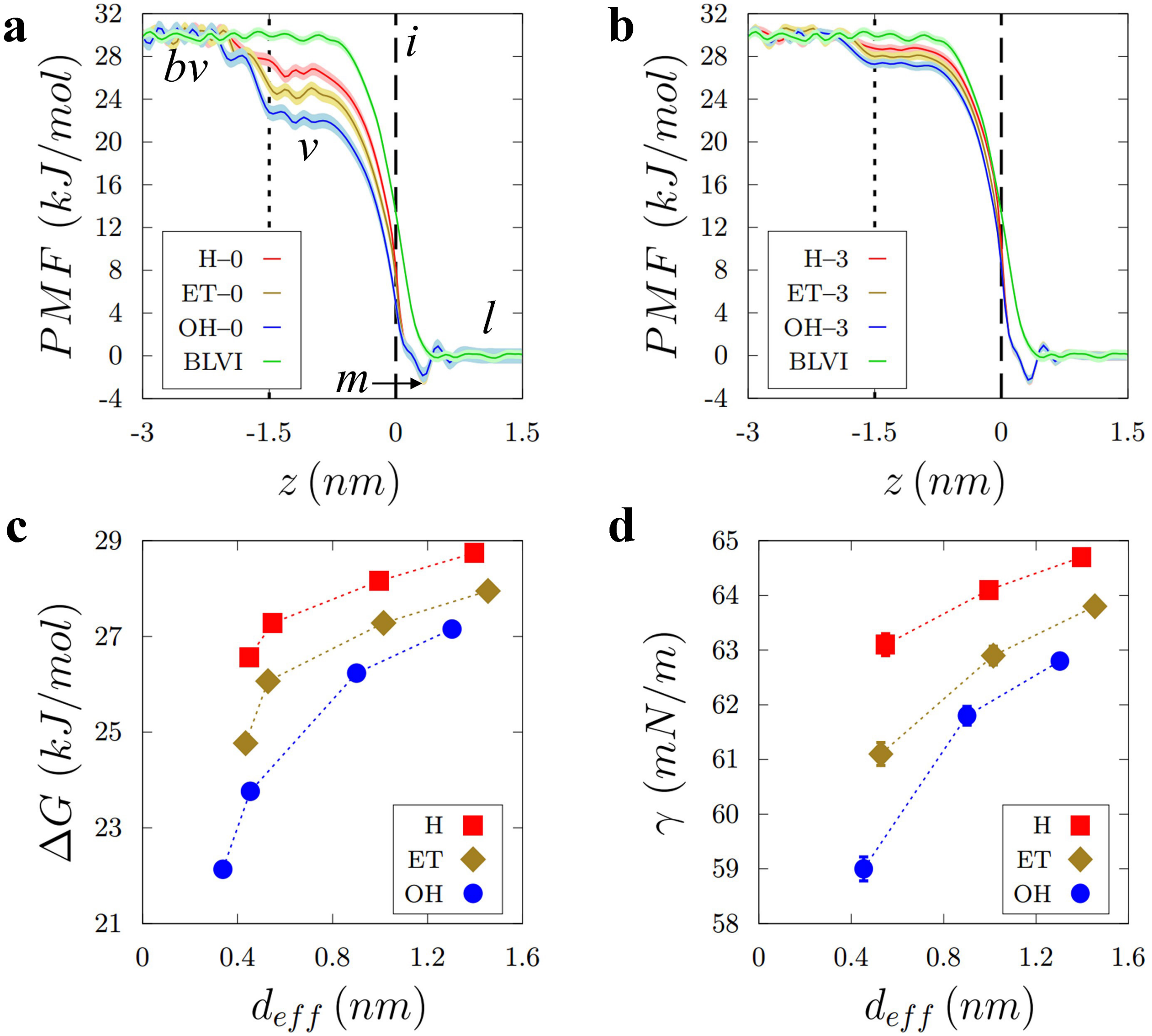

Figure 2.14. Free energy calculations for evaporation of water molecules and surface tension at water-vapor interface for different FNPGs. (a) PMF profiles for evaporation of water molecules through the FNPGs with type-0 nanopores, with different regions depicted. (b) PMF profiles for evaporation of water molecules through the FNPGs with type-3 nanopores. The same for the BLVI is also shown for comparison. Black dashed lines denote the position of FNPG (or vapor edge of "10–90" interface for BLVI), (z = 0). The fluctuations in the PMF values are denoted by the shaded regions around the PMF plots. (c) Free energy barrier (ΔG) for taking a water molecule from bulk liquid (l) to vapor phase (v), with ΔG for BLVI shown for comparison. (d) Surface tension at the water-vapor interface for different FNPGs. Surface tension at the water-vapor interface of BLVI is shown for comparison. Due to insufficient sampling in the ROI of type-0 nanopores, we report the values for type-1,2 and 3 nanopores only.

Due to the enhanced density in the contact water layer formed adjacent to the FNPG, a distinct global minimum (denoted as 'm' in **Figure 2.14a**) in the free energy profile was observed at z = 0.35 nm coinciding with the maxima in the density distribution (**Figure 2.11h**) where the water molecule resides prior to escaping into the vapor phase. Since an evaporating water molecule located at the minimum has to overcome a free energy barrier across the FNPG to enter the vapor phase, we also evaluated the free energy barrier for a water molecule to translocate ($\Delta G_t = G_i - G_m$) from this minimum to the interface (denoted as 'i' in **Figure 2.14a**). In all cases, ΔG_t values were smaller than the corresponding ΔG_t = 13.47 kJ/mol obtained for the BLVI, indicating the lowered barrier for evaporation due to the presence of the nanopores (**Table 2.4**). For the OH–0 nanopores, a significant reduction was observed, with ΔG_t = 6.57 kJ/mol. Interestingly, only a marginal increase was observed for the free energy change ($\Delta G_e = G_v - G_i$) between the vapor region ('v') and the interface ('i') across the different pore types lying between 17.28 kJ/mol for OH–0 nanopores and 18.87 kJ/mol for H–3 nanopores. Further, this free energy change was slightly higher than 16.40 kJ/mol obtained for the BLVI (**Table 2.4**). These differences are, however, less than 1 $k_B T$ (2.49 kJ/mol) at 298 K (25 °C), indicating that the enhancement in evaporation flux is governed mainly by the larger differences in ΔG_t driven primarily by the interaction between functional groups and water molecules in the ROI (**Figure 2.13**).

Since we observed an increased evaporation flux from both experiments and MD simulations for the nanopores, we computed interfacial tension (γ) at the water-vapor interface using the Kirkwood pressure tensor formulation [118,175]. Unlike the BLVI, in the case of the nanopores, the pressure tensor computation was carried out in the ROI. **Figure 2.14d** illustrates the surface tension at the water-vapor interface for different FNPG systems. The greatest decrease in γ was observed for the type-1 nanopores, and the smallest value of 59.0±0.02 mN/m was observed for the OH–1 nanopores correlating with the highest flux observed in the MD simulations (**Figure 2.11e**). Additionally, for a given pore type, the greatest reduction in γ occurred for the OH-functionalization followed by the ET-functionalization with the least reduction observed for the H-terminated nanopores (**Figure 2.14d** and **Table 2.5**).

We note that previous studies attributed the enhanced evaporation to the extended meniscus or evaporation area [6,16] outside the hydrophilic pore mouth. In our case, the support film hosting 20-nm-sized pore opening was a film with macroscopic length-scale (1 mm^2); therefore, it did not have any significantly extended meniscus. Hence, no enhancement was observed from the support film. For nanoporous graphene, one can rule out the existence of an extended liquid film on the back side of the graphene film as the basal plane of graphene away from the pore is hydrophobic. This is also evidenced by the imaging of nanopores obtained by oxidative treatment where oxygen-containing functional groups are clustered around the pores leaving a pristine hydrophobic basal plane between the pores [97]. In addition, this has also been recently borne out in molecular simulations of water adsorption on graphene oxide surfaces [176]. Therefore, the observed enhancement could be explained by the hydrogen bonding dynamics in a confined geometry of graphene nanopores, as shown by the MD simulation.

2.4 Conclusion

We report a significant enhancement in water evaporation flux, up to 35-fold compared to BLVI, when millimeter-scale 2D graphene film hosting billions of oxygen-functionalized Å-scale pores is positioned at the liquid-vapor interface, with enhancement exhibiting a strong dependence on the pore size. We discuss that enhancement from millimeter-sized porous graphene in our study is obtained without any extended liquid meniscus and is linked to the rapid hydrogen bonding and orientational dynamics of water in the vicinity of the nanopore rendered by the strong interaction between the water molecule and the pore edge oxygen-functional groups. This results in a decreased free energy barrier for water crossover to the vapor phase, leading to an enhanced evaporation flux. Enhancement increases for the smaller pores because water molecules have a higher probability to interact with the edge function groups in smaller pores.

Before this study, the state-of-the-art studies on evaporation of water confined in nanopores were limited to the solid-state pores that were several nanometers in size and length. Therefore, this study constitutes the ultimate limit for the confinement of the liquid/vapor interface where the interface is only atom thick, and pores are commensurate to the size of water molecules. This was possible by carefully placing crack-free nanoporous graphene film on the water-vapor interface while ensuring that the liquid supply to the interface as well as the mass transfer of vapor away from the interface were not the rate-limiting step. Opposite flux trends observed for water evaporation rate and gas transport as a function of pore size from the same film adds robustness to our conclusion.

Overall, this study provides the first experimental demonstration of significantly enhanced water evaporation flux from a 2D nanoporous interface hosting Å-scale pores. The enhancements observed here can be extremely attractive for applications dependent on the phase change of liquid water. The findings in this study are expected to aid the development of novel strategies for evaporation-based separations, e.g., membrane distillation.

2.5 Appendix I

2.5.1 Water supply and vapor removal limit in the evaporation process

In general, the event of water evaporation through graphene comprises three steps: (a) water transport to the liquid-vapor interface at the nanopore, (b) liquid vaporization at the nanopore, and (c) water vapor leaving the entrance of the nanopore. For the sake of measuring only the kinetic limit of water evaporation through the nanoporous graphene, we cautiously examine if the evaporation is limited by step (a) and (c). In the case of step (c), given that the permeate side of the set-up is at 500 mTorr (~ 66 Pa) vacuum and low absolute water evaporation flux, the diffusion of water vapor leaving the nanopore is greatly accelerated, and therefore, it is not the limiting factor. On the other hand, the capillary pressure and the transport impedance of each layer determine the liquid water supply in nanoporous graphene/support films. Assuming that water flow through the support film (NPC film) behaves as a classical liquid in a cylindrical tube while that through the nanoporous graphene/support film behaves as a Sampson's flow, we can employ the Hagen-Poiseuille equation, Sampson's formula and Young-Laplace equation [56,177]:

$$Q \sim \sigma\left(\frac{\Delta P}{R_{NPC}+R_{Gr}}\right)\rho \qquad \textbf{(Equation 2.10)}$$

$$\Delta P = \frac{4\gamma\cos\theta}{D_{Gr}} - \frac{4\gamma\cos\theta^*}{D_{NPC}} \qquad \textbf{(Equation 2.11)}$$

$$R_{NPC} = \frac{128\mu L_{NPC}}{\pi D^4_{NPC}} \qquad \textbf{(Equation 2.12)}$$

$$R_{Gr} = \frac{24\mu}{D^3_{Gr}} \qquad \textbf{(Equation 2.13)}$$

where Q is the mass flow per unit area per unit time in the case when the meniscus starts to recede,which is also regarded as the lower limit of water supply. σ is the pore density per unit area of nanoporous graphene, ρ is the density of water, ΔP is the difference of capillary pressure, and γ is the surface tension of water. D_{Gr} and D_{NPC}, as well as θ and θ^*, are the pore diameter and water contact angle of graphene and the support film, respectively. R_{NPC} and R_{Gr} represent the impedance of the support and graphene layer. μ is the viscosity of water, and L refers to the thickness of the film. In the case of a standalone support film, we do not consider the contribution from graphene. **Figure 2.15** shows the comparison between the calculated liquid supply limits and the experimental data at 22 °C. It is clearly seen that the limits are few order-of-magnitude higher than the measured evaporationfluxes, suggesting that water supply is not a limiting factor for all our measurements.

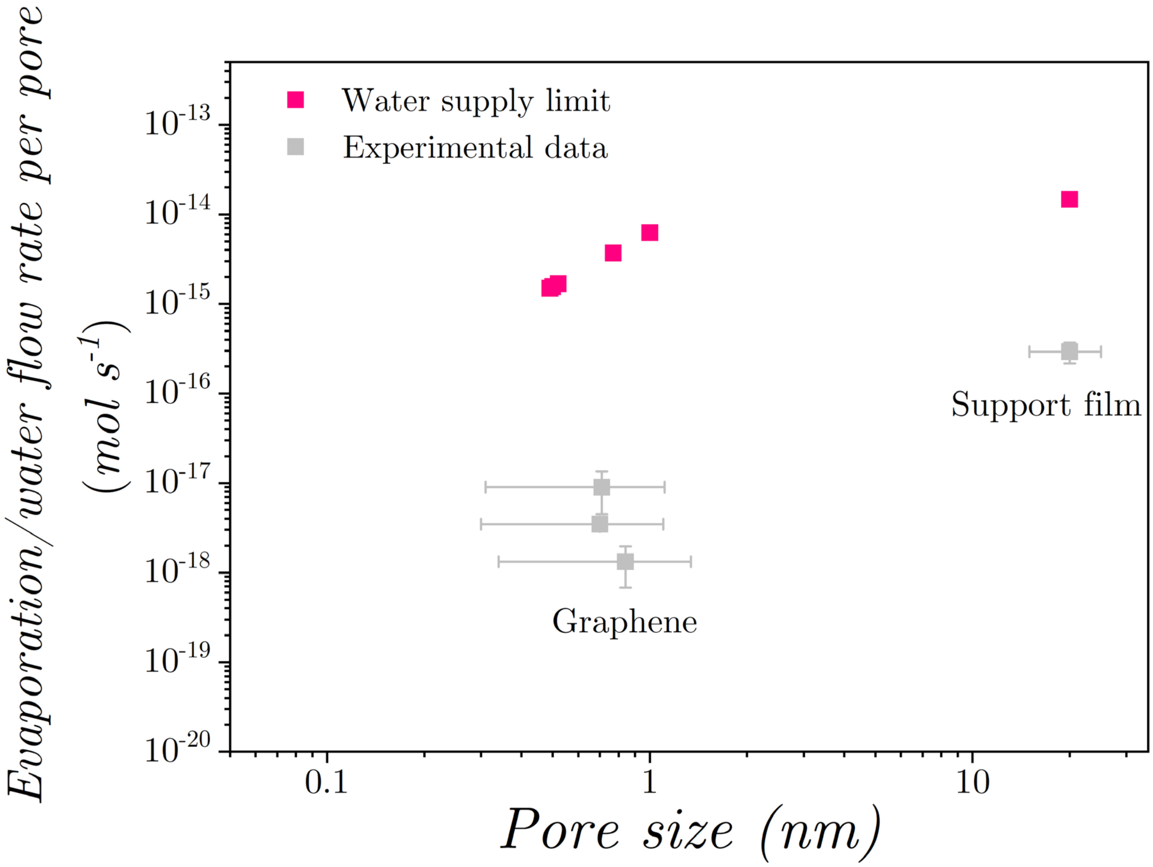

Figure 2.15. Comparison of calculated water supply limit and the measured evaporation flux of all tested nanoporous graphene films at 22 °C.

2.5.2 System details of MD

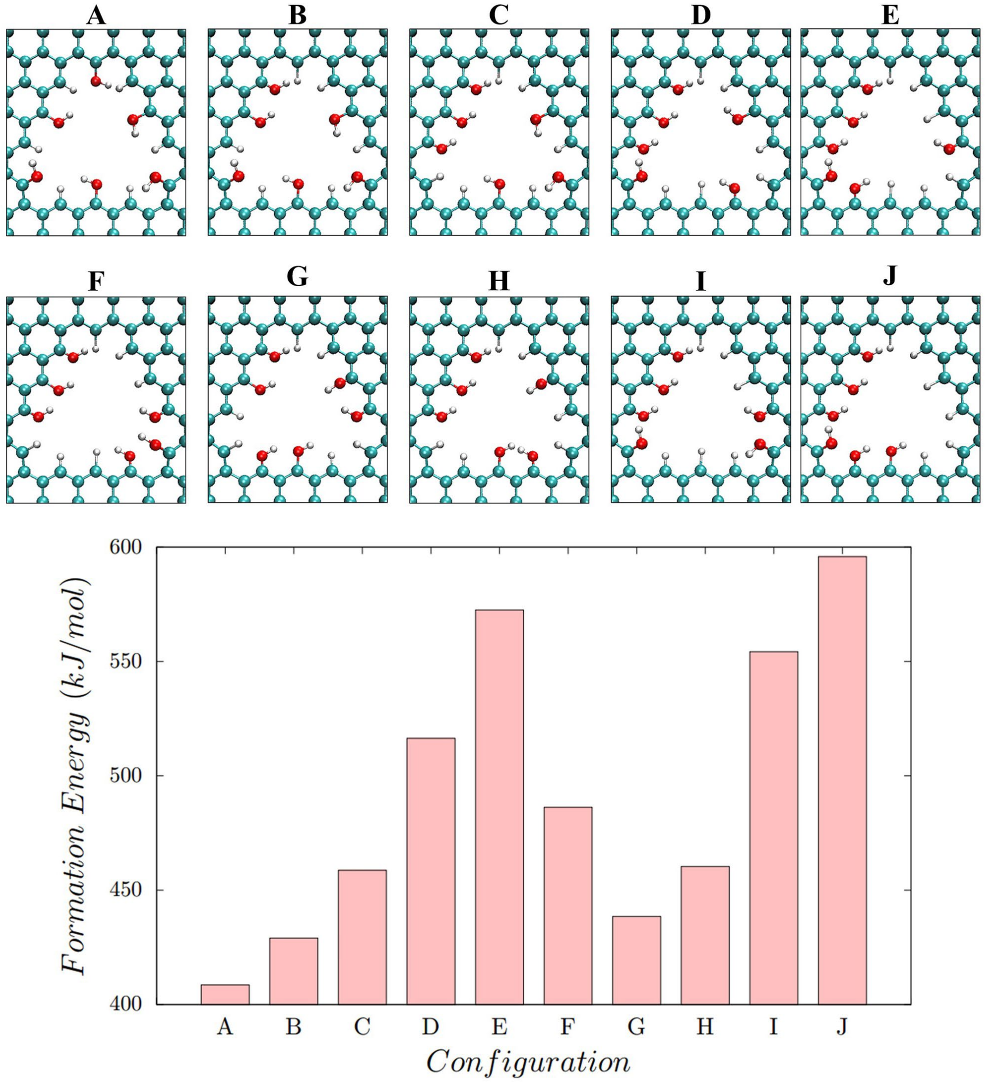

Figure 2.16. Different arrangements of H atoms and OH functional groups on the edge of type-1 nanopore to determine the FNPG with the lowest formation energy and the formation energies of optimized FNPGs with the arrangements of H atoms and OH functional groups on the edge of nanopore corresponding to the different configurations (A–J).

Table 2.2. Effective pore diameter, d_{eff} and effective pore area, A_{eff} of each functionalizednanopore of the FNPGs shown in Figure 2.11a.

Pore	d_{eff} (nm)	A_{eff} (nm^2)
H–0	0.448	0.158
ET–0	0.434	0.148
OH–0	0.338	0.090
H–1	0.549	0.237
ET–1	0.528	0.219
OH–1	0.454	0.162
H–2	0.996	0.779
ET–2	1.015	0.809
OH–2	0.901	0.638
H–3	1.397	1.533
ET–3	1.454	1.660
OH–3	1.303	1.333

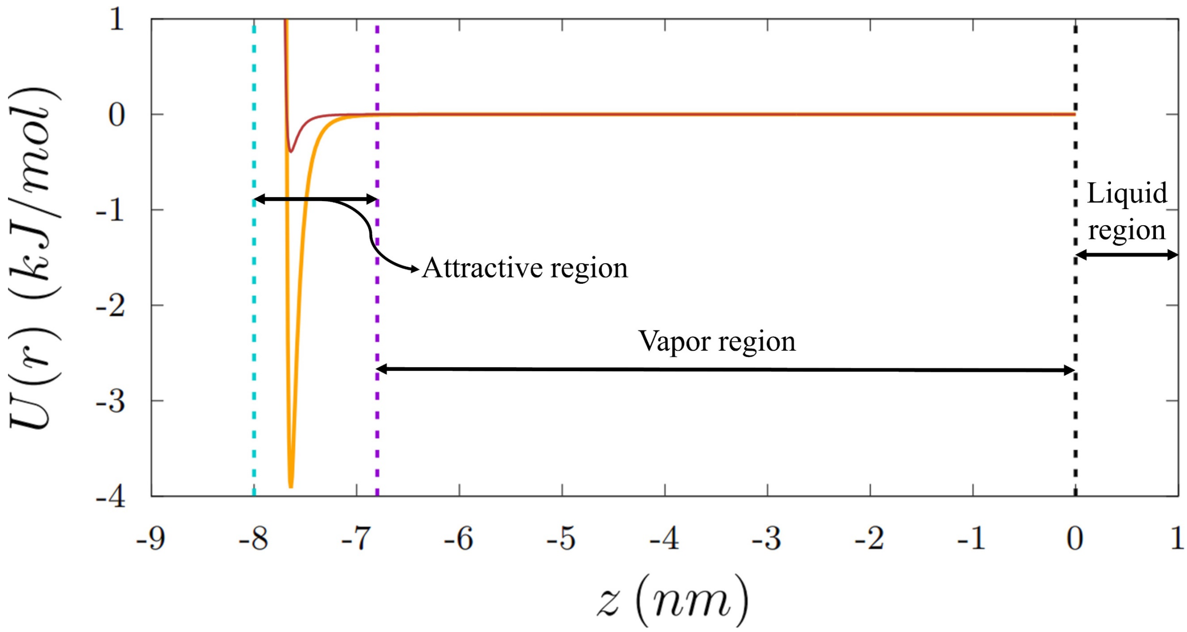

Figure 2.17. Interaction potential between the carbon atom of the attractive wall and the oxygen atom of water molecule (shown in orange). The carbon-water interaction parameters are adjusted to yield a ten times greater interaction potential between the carbon atom of the attractive wall and the oxygen atom of water molecule (σ_{CO}=3.19 A˚, ϵ_{CO}=3.92 kJ/mol). The cutoff for the van der Waals interactions was set as 1.2 nm and hence the water molecules beyond this distance are unaffected by the influence of the attractive wall. This also ensures a vapor region of 6.8 nm for the evaporating water molecules. For comparison, the same for the single pristine graphene sheet (brown) is also shown. The attractive wall is placed at *z*= 8 nm (shown in dotted cyan line) and its influence is limited to a cut-off of 1.2 nm (shown in dotted violet line).FNPG is present at *z* = 0 (shown in black dotted line). Different regions are also depicted.

2.5.3 Cumulative number of evaporated water molecules and evaporation flux calculation

For the production run of 500 ns, we track the net number of water molecules leaving the FNPG in increments of 1 ns (**Figure 2.18**).

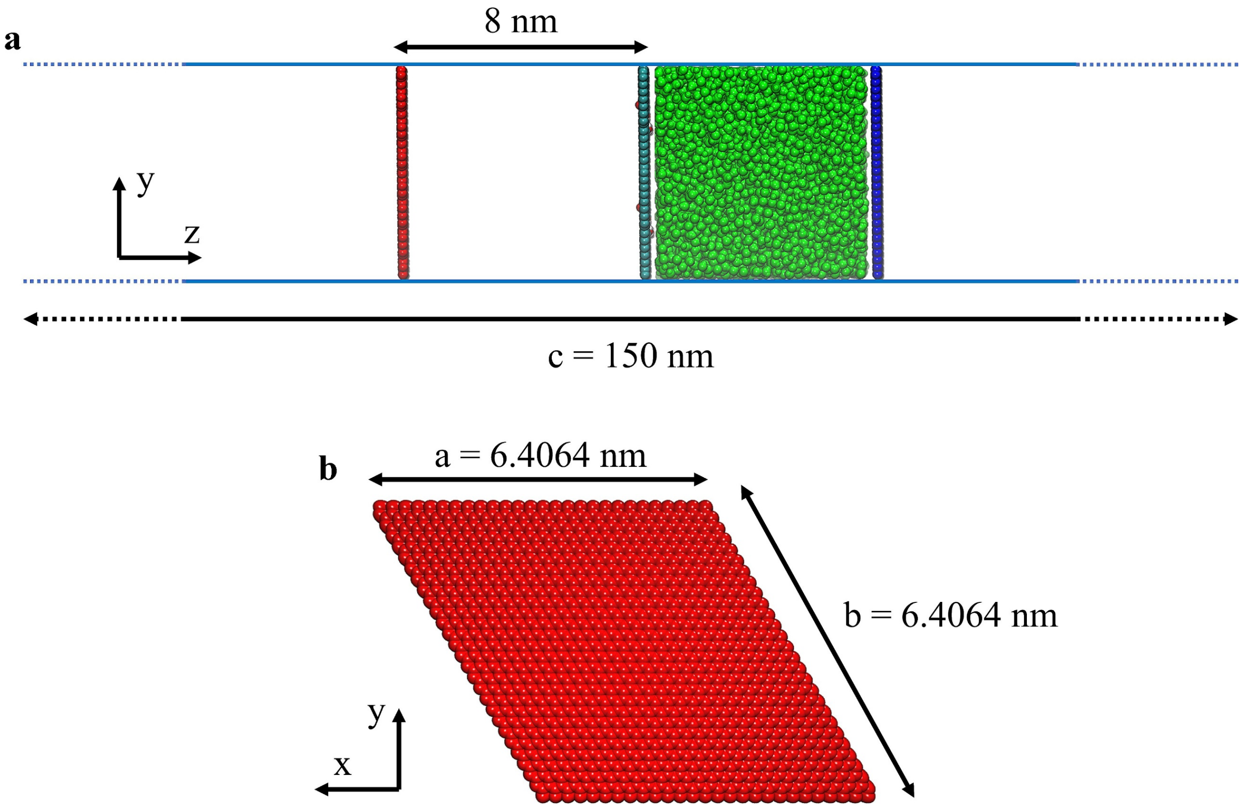

Figure 2.18. System details and dimensions for simulation with FNPGs. (a) Side view of the simulation box with the dimensions depicted. The dimensions that are invariable with time are only shown. (b) Top view (from the attractive wall side) with the dimensions depicted. Red: Attractive wall, Cyan: FNPG, Green: Water molecules, and Blue: Piston.

System details and dimensions for the bare liquid-vapor interface (BLVI) simulations are given in **Figure 2.19**. Since water molecules can now evaporate from two opposing surfaces, we have used two attractive walls. We have used 42650 water molecules for simulating a BLVI. **Figure 2.19b** illustrates the water density profile for a BLVI. This density profile was fit with a hyperbolic tangent function of the following form:

$$\rho(\mathrm{z})=\frac{\rho_l+\rho_v}{2}-(\frac{\rho_l-\rho_v}{2})\tanh(\frac{2.1972(z-z_0)}{h}) \qquad \textbf{(Equation 2.14)}$$

where ρ_l and ρ_v are the liquid and vapor phase densities, respectively. z_0 is the position of Gibbs dividing surface, where $\rho(\mathrm{z})=\frac{\rho_l+\rho_v}{2}$. h is the thickness of "10–90" interface which describes the density change from 90% to 10% of the bulk water density.

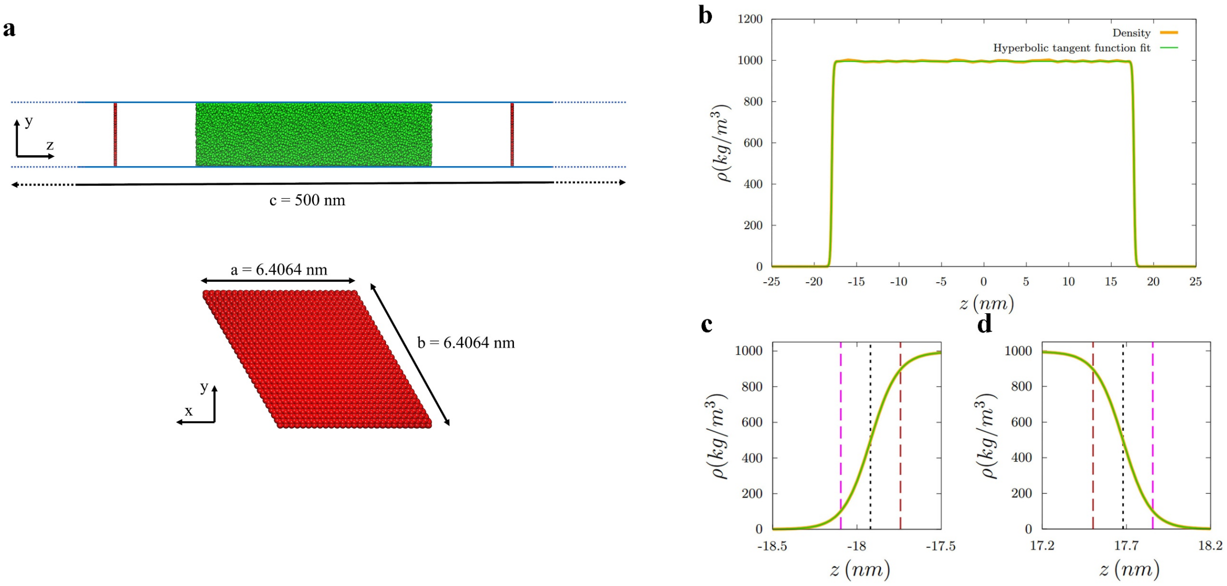

Figure 2.19. Density profile of water molecules in the BLVI simulations. (a) System details and dimensions for the bare liquid-vapor interface (BLVI) simulations. Side view of the simulation box with the dimensions depicted. The dimensions that are invariable with time are only shown. Top view (from the attractive wall side) with the dimensions depicted. Red: Attractive wall and Green: Water molecules. (b) Density profile of water molecules along with the hyperbolic tangent function fit. (c) and (d) Density profiles along with the hyperbolic tangent function fit for left and right interfaces, respectively. Black dotted line: Gibbs dividing surface. Magenta dashed line: Vapor side of ‘h.’ Brown dashed line: Liquid side of ‘h.’

Since we have two liquid–vapor interfaces, **Figure 2.19c** and **d** illustrates the position of the Gibbs dividing surface and the “10–90” thickness for the left and right interfaces, respectively. For the left interface we have z_0 = −17.92 nm and h = 0.354 nm whereas for the right interface we have z_0 = 17.68 nm and h = 0.355 nm. For the flux computations, we evaluate the net num- ber of water molecules leaving the vapor edge of “10–90” thickness (magenta dashed lines in **Figure 2.19c** and **d**). The cumulative number of water molecules evaporating through different FNPGs and BLVI are shown in **Figure 2.20**. Using the above procedure to determine the net number of water molecules leaving the interface, we observe that the cumulative increase follows a linear trend over the 500 ns of sampling time for all the different FNPGs as well as the BLVI (**Figure 2.20**). Linear fits to the N versus t data are used to determine the flux for the different FNPGs using

$$j = \frac{1}{A_{eff}} \frac{dN}{dt}$$ **quation 2.15)**

where A_{eff} is the effective area for evaporation.

The calculated evaporation flux is summarized in **Table 2.3**.

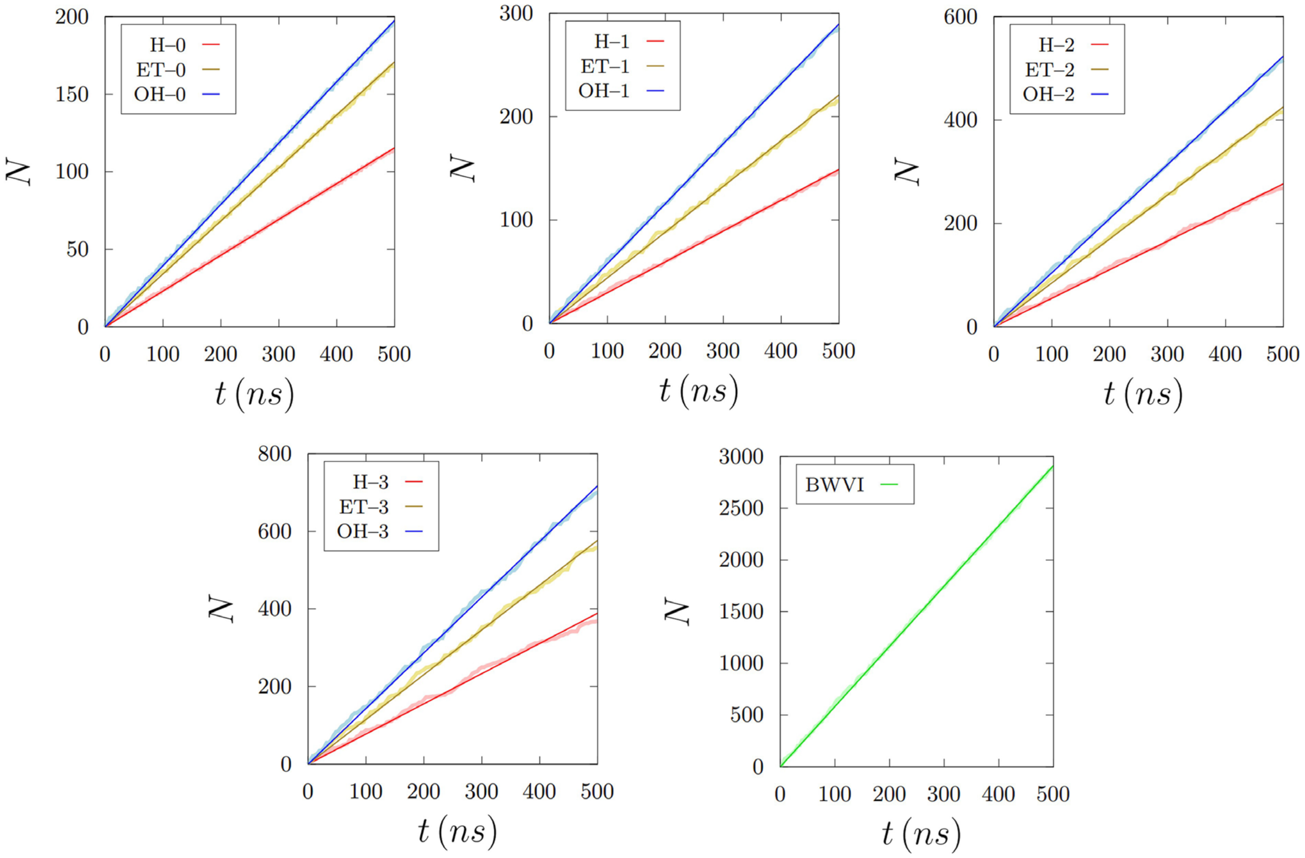

Figure 2.20. Cumulative number of evaporated water molecules. Each panel represents the cumulative number of water molecules evaporating through FNPGs with type-0, 1, 2, and 3 nanopores, and BLVI.

Table 2.3. Details for evaluation of evaporation flux, *j*. The data of BLVI includes both interfaces.

Pore	*dN/dt* (molecules/ns)	A_{eff}	*j* (molecules/ns/nm^2)
H–0	0.228	0.632	0.360
ET–0	0.336	0.592	0.567
OH–0	0.389	0.360	1.081
H–1	0.291	0.948	0.307
ET–1	0.429	0.876	0.490
OH–1	0.570	0.648	0.880
H–2	0.535	3.116	0.172
ET–2	0.828	3.236	0.256
OH–2	1.030	2.552	0.404
H–3	0.737	6.132	0.120
ET–3	1.115	6.640	0.168
OH–3	1.398	5.332	0.262
BLVI	5.751	71.088	0.081

2.5.4 Dipole-dipole re-orientational dynamics and mean square displacement

Dipole-dipole re-orientational dynamics are analysed by computing the first,(l = 1) and second rank (l = 2) Legendre polynomials of the water dipole moment. The orientational correlation functions (OCFs), Γ^{l}_{μ}, are calculated using:

$$\Gamma_l^{\mu}(t) = \left\langle \sum_{i=1}^{N} P_l\,[\mu(t)\cdot\mu(0)] \right\rangle_{\tau,N} \qquad \textbf{(Equation 2.16)}$$

where the $\langle\cdot\ \cdot\ \cdot\rangle_{\tau,N}$ represents an ensemble average over τ shifted time origins and encompasses the subset of water molecules continuously surviving in the ROI during the time interval t. P_l are the

Legendre polynomials of rank *l*. μ denotes the unit vector in the direction of the water dipole. To capture the relaxation times we use a biexponential function:

$$\Gamma_l^{\mu}(t) = A_f^{\mu} \exp(\frac{-t}{\tau_f}) + A_s^{\mu} \exp(\frac{-t}{\tau_s}) \qquad \textbf{(Equation 2.17)}$$

where τ_f represents the time constant for faster timescale relaxation and τ_s represents the time constant for slower timescale relaxation. A_f^{μ} and A_s^{μ} represent the parameters for components of the faster and slower timescale relaxations, respectively.

The dipole relaxation times of the water molecules are then calculated using:

$$\tau_l = \frac{A_f^{\mu}\tau_f + A_s^{\mu}\tau_s}{A_f^{\mu} + A_s^{\mu}} \qquad \textbf{(Equation 2.18)}$$

Computation of A_f^{μ}, A_s^{μ}, τ_s, and τ_l for $l = 1$ and $l = 2$ is organized in 5000 blocks, each having a length of 0.1 ns.

Mean square displacement (MSD) of water molecules present in the ROI of different FNPGs is calculated in the z-direction (perpendicular to the surface of FNPG) using:

$$MSD_z(t) = \left\langle \sum_{i=1}^{N} \left| z_i(\mathrm{t}) - z_i(0) \right|^2 \right\rangle_{\tau,N} \qquad \textbf{(Equation 2.19)}$$

where $z_i(t)$ is the z coordinate of the center of mass of water molecule *i* and $\langle \cdot\ \cdot\ \cdot \rangle_{\tau,N}$ represents an ensemble average over τ shifted time origins and encompasses the subset of water molecules continuously surviving in the ROI during the time interval *t*.

2.5.5 PMF calculation

Table 2.4. Free energy difference (kJ/mol) between different regions.

Pore	$\Delta G = G_v - G_l$	$\Delta G_t = G_i - G_m$	$\Delta G_{vi} = G_v - G_i$
H–0	26.57	10.29	18.33
ET–0	24.77	9.25	17.49
OH–0	22.13	6.57	17.28
H–1	27.28	10.71	18.74
ET–1	26.07	9.41	18.70
OH–1	23.77	7.11	18.58
H–2	28.16	11.63	18.79
ET–2	27.28	10.75	18.74
OH–2	26.23	9.71	18.66
H–3	28.74	12.18	18.87
ET–3	27.95	11.46	18.70
OH–3	27.15	10.63	18.70
BLVI	29.87	13.47	16.40

Table 2.5. Surface tension values at water-vapor interface for different FNPG systems andBLVI.

Pore	γ (mN/m)
H–1	63.1
ET–1	61.1
OH–1	59.0
H–2	64.1
ET–2	62.9
OH–2	61.8
H–3	64.7
ET–3	63.8
OH–3	62.8
BLVI	65.62

Chapter 3 Size-dependent Subcontinuum Ion Permeation Across Nanoporous Graphene Membranes

Abstract

Atomically thin graphene nanopores are promising for mimicking the functionality of biological channels which demonstrate a remarkable ion-ion selectivity. However, the performance of the state-of-the-art nanopores/nanochannels is far from that from biological channels due to difficulty in achieving a precise control over the pore size. Here, we report nanoporous graphene membranes hosting pores approaching the size of hydrated ions to enable effective monovalent cation sieving. The controlled pore size at the sub-nanometer scale is realized by top-down etching-based nucleation and pore expansion, which results in a sharp molecular cutoff for maximum K^+/Mg^+ and Li^+/Mg^{2+} selectivities up to 350 and 260, respectively. Analysis of the transport resistance model and the energy barrier for ion transport suggests that the high selectivity results from a size-exclusion mechanism associated with the ion-dependent dehydration process. Our findings demonstrate the potential of graphene nanopores for application in metal mining, energy storage, and various separation technologies.

3.1 Introduction

Understanding the transport of ionic species under nanoscale confinement to mimic the conditions in biological channels is desirable because it involves unexplored fluid mechanics in a new regime, which enables the novel development of energy storage [23,178,179], nanofluidic applications [180,181], and high-efficiency separation [82,182,183]. In particular, ion–ion separation using nanopores/nanochannels is attractive for the extraction of highly demanded lithium from brine [184–186], in which the recovery process separates Li^+ from Mg^{2+} in a highly concentrated salt mixture [185,187]. Conventional methods relying on reactive extraction of Li are energy-intensive and lead to large consumption of scarce fresh water resources near Li-rich mines [188,189]. In this respect, high-performance membranes yielding a large Li^+ flux and high Li^+/Mg^{2+} selectivity are highly attractive to meet the growing demand for lithium in applications involving renewable energy and next-generation vehicles [190].

Biological channels have shown an exceptional transport rate of K^+ or Na^+ [191,192] while simultaneously rejecting divalent cations. The ultrahigh ion selectivity of protein-ion channels results from a sub-nanometer-sized pore channel [193] and the presence of a selectivity filter [194,195]. In contrast, artificial nanochannels/nanopores perform poorly compared to their biological counterparts. This is mainly because of the difficulty in controlling the pore size distribution of nanopores in artificial channels. Improving the control over the pore size, down to the resolution of 1 Å, is expected to significantly improve the ion–ion selectivity [196,197]. For instance, graphene oxide laminates with an interlayer spacing below 8 Å [13,198] demonstrated a K^+/Mg^{2+} selectivity up to 650 and a Li^+/Mg^{2+} selectivity up to 500. Polymeric membranes [17,199] and metal-organic frameworks [18,200,201] with channel sizes in the sub-1-nm regime also achieved ion sieving of monovalent cations from divalent cations. On the other hand, atomically thin nanopores [22,23,47] have shown potential for studying ion transport under nanoconfinement along with mimicking the high performance of biological channels due to the atomic thinness. However, no remarkable metal-ion selectivity from two-dimensional nanopores has been reported. The key challenge in achieving high ion selectivity is the controllable tuning of the nanopore diameter approaching the size of hydrated ions. Several attempts have been made to investigate the cation selectivity of graphene nanopores. Pioneer work done by Rollings *et al.* [47] involved ionic transport across 2–23-nm-sized graphene nanopores, in which a high K^+/Cl^- selectivity over 100 was obtained due to the electrostatic interaction between the ions and the negatively charged pore rim. Nevertheless, the K^+/Mg^{2+} and Li^+/Mg^{2+} selectivities were low, approximately 4 and 3, respectively. Cation selectivities in current studies on nanoporous graphene membranes [28,183,202,203] are also far from those expected due to the large pore size and cracks and tears on the membrane. Furthermore, a clear understanding of the factors affecting the ion selectivity of graphene nanopores remains limited, and a detailed investigation is urgently needed.

Herein, we design a robust graphene nanopore platform to study ion transport under sub-nanometer confinement. Taking advantage of the etching kinetics of two different chemical etchants, O_3 and CO_2, decoupled pore nucleation and expansion in a graphene lattice were achieved, thereby creating nanopores at the sub-nanometer scale for ion transport. We demonstrate that tailored pore size and pore structure can modulate the diffusion of ions across the nanopores and enable a K^+/Mg^{2+} selectivity up to 70 and a Li^+/Mg^{2+} up to 50. The ion selectivity can be further improved by reducing the number of non-selective pores in the nucleation step using a graphene regrowth method. The size-dependent metal ion selectivity suggests the steric effect associated with ion dehydration as the main factor governing ion transport. In addition, the nanopores exhibit stable fluxes across a range of electrolytes with high concentration (1 M), and high M^+/Mg^{2+} (M: K, Na, or Li) selectivities are preserved in a solution mixture of all the tested ions. This work shows a significant improvement in the ion selectivity of 2D nanopores, which is promising for a wide range of separation applications.

3.2 Methods and materials

3.2.1 Synthesis of single-layer graphene by low-pressure chemical vapor deposition (LPCVD)

Single-layer graphene was synthesized by the LPCVD process using a pre-annealed copper foil (50 µm thick, 99.9 % purity, Stream). Briefly, the foil was subjected to a CO_2 and H_2 atmosphere at 1000 °C for 30 min, respectively. Subsequently, 24 sccm of CH_4 and 8 sccm of H_2 were introduced into the reactor at a total pressure of 460 mTorr for 30 min. The reactor was then rapidly cooled down to room temperature after the completion of the synthesis.

3.2.2 Defects generation in graphene lattice using ozone

A homemade setup was used for incorporating defects into the graphene lattice. The setup was composed of a reactor chamber with a thermocouple placed inside the heating zone. The reactor was carefully wrapped with a heating tape, which was connected to a controller. Briefly, as-synthesized graphene on Cu was placed inside the reactor under a continuous Ar flow (100 sccm) in 1 bar at 43 °C. After the whole system reached thermal equilibrium, the Ar flow was cut off, followed by the injection of an O_3/O_2 mixture (9 % O_3 on a molar basis, Atlas 30, Absolute Ozone) into the chamber. The as-synthesized graphene was exposed to the O_3/O_2 mixture for 1 h. Thereafter, the O_3/O_2 mixture was cut off, the heater was turned off, and an Ar flow was injected to flush away the remaining O_3.

3.2.3 Expansion of graphene nanopores using CO_2 as the etchant and regrowth of graphene in large pores

First, O_3-treated graphene on Cu was placed in a tubular furnace. The furnace was filled with H_2 (100 sccm) and evacuated three times, and then refilled to a pressure of 800 torrs. After that, the furnace was heated to 800 °C in 50 min and kept at 800 °C for 2 minutes. Subsequently, a mixture of H_2 (23 sccm) and CO_2 (50 sccm) was introduced into the furnace and flowed through the reactor for 5 to 8 minutes. Once the expansion was done, the reactor was then rapidly cooled down to room temperature to stop the reaction. For the regrowth of graphene in larger pores, prior to CO_2 etching, the sample was exposed to a mixture of CH_4 and CO_2 (molar ratio 2:1) with H_2 as a protective gas at 800 °C for 10 min.

3.2.4 Membrane fabrication

Nanoporous graphene was reinforced by a two-layer composite film composed of a NPC film [130] and a Nafion film. First, the fabrication of the porous carbon film on graphene was performed using a method reported elsewhere with modification. Briefly, the precursor of NPC was prepared by dissolving 0.1g poly(styrene-b-4-vinyl pyridine) and 0.2 g turanose in 1 g N,N-dimethylformamide. Subsequently, the solution was heated at 180 °C for 3 h. The NPC film was obtained by spin coating the solution on the nanoporous graphene resting on a Cu foil, followed by pyrolysis at 500 °C in a H_2/Ar atmosphere for 1 h. Thereafter, a Nafion (Nafion D-520 dispersion, 5 % w/w in water and 1-propanol) layer was spin-coated onto the NPC/Gr/Cu film, followed by maintaining the resultant film at 120 °C for 1 h to induce cross-linking in the Nafion film. Then, the nanoporous graphene on Cu supported by the two-layer composite film was placed in a $FeCl_3$ bath to remove the Cu foil. After Cu etching, the floating graphene composite film was rinsed in HCl and deionized (DI) water to remove the residues. Finally, the floating graphene film was scooped on a polytetrafluoroethylene (PTFE) washer (outer diameter: 20 mm, inner diameter: 8 mm) for other use.

3.2.5 Ion diffusion tests

A homemade diffusion cell with two 50 mL chambers was used for membrane performance testing. A membrane (area of 50.3 mm^2) was sandwiched between two PTFE washers and mounted between two chambers, with the graphene side toward a feed solution. The feed solution contained 1 or 0.1 M of one or mixed salts (KCl, NaCl, LiCl, $MgCl_2$, >98%, Sigma-Aldrich), and the receiving solution contained Milli-Q water. Over the measurement period, the concentration change in the receiving side was negligible compared to the feed concentration; therefore, the driving force for ion diffusion remained constant. For single-ion tests, a pre-calibrated conductivity probe (Mettler-Toledo GmbH, SevenCompact Cond. Meter S230) was placed in the receiving chamber to record the conductivity increase due to ion diffusion for 5 h. The conductivity (μs/cm) was converted to concentration (mol/L) by obtaining a calibration curve of conductivity as a function of concentration, which was measured by inductively coupled plasma-optical emission spectrometry (ICP-OES, 5110, Agilent). For mixed-ion tests, the concentration of each cation was measured by ICP-MS. The membrane cation flux, J, was then calculated as:

$$J = \frac{C_r V}{A \Delta t} \qquad \textbf{(Equation 3.1)}$$

where C_r is the concentration in the receiving chamber, V is the volume of the chamber, A is the area of the membrane, and Δt is the time.

The selectivity, S_{ij}, of one cation, i, over another one, j, was calculated as:

$$S_{ij} = \frac{J_i / J_j}{C_{f,i} / C_{f,j}} \qquad \textbf{(Equation 3.2)}$$

where J_i is the flux of cation *i* and $C_{f,i}$ is the feed concentration of cation *i*.

3.2.6 Scanning tunneling microscope (STM) imaging

STM imaging was performed using a low-temperature STM (CreaTec Fischer & Co. GmbH). To remove contamination from the graphene surface, the graphene/Cu samples were annealed/reduced under H_2 flow (50 sccm) at 800 torr and 900 °C for 3 hours in a quartz tube furnace to reduce the oxidized copper surface. Right after the 900 °C annealing, the sample was transferred to the UHV chamber of the STM. The samples were again heated inside the UHV chamber at 700°C for 3 hours to remove the surface contamination. STM imaging was performed at 77 K and a pressure of 2×10^{-10} mbar. The STM probe was prepared by cutting a commercial Pt/Ir wire (Pt: 90 wt % and diameter of 0.25 mm; Alfa Aesar). The tilt in the acquired STM images was reduced by flattening in the WSxM software [204].

3.2.7 Other characterizations

Scanning electron microscope (SEM) images were obtained by using an FEI Teneo scanning electron microscope at 1.0–5.0 kV and working distances of 2.5–5.0 mm. No conductive coating was applied to the substrates before SEM imaging. The thickness of the film was measured by optical profilometry. Raman measurement was performed on the nanoporous graphene on the Cu foil right after the synthesis using 457 nm excitation and the Renishaw micro-Raman spectroscope with a 100× objective. The obtained Raman data were analyzed using a MATLAB script. To calculate the D and G peak heights, the background was subtracted from the Raman data using the least-squares curve fitting tool (lsqnonlin). X-ray photoelectron spectroscopy (XPS) measurements on highly oriented pyrolytic graphite (HOPG) and graphene resting on the Cu foil were carried out on Axis Supra (Kratos Analytical) using the monochromated Kα X-ray line of an aluminum anode. The pass energy was set to 20 eV, and the step size was set to 0.1 eV. The peak fitting was performed using CasaXPS, and the Shirley method was used for background subtraction.

3.3 Results and discussion

3.3.1 Tailored graphene nanopores for selective ion transport

To understand the transport behavior of cations (K^+, Na^+, Li^+, and Mg^{2+}) under nanoconfinement, the nanopores in graphene were tailored via decoupling the pore nucleation and expansion using two different chemical etchants. High-quality single-layer graphene ($I_{2D}/I_G = 2.3\pm0.5$, $I_D/I_G = 0.09 \pm 0.03$) was synthesized by LPCVD on a catalytic substrate, Cu. Prior to the synthesis, the substrate was thermally annealed in the H_2/Ar atmosphere to reduce the roughness of Cu as well as the density of the intrinsic defects. O_3 was used as an etchant to generate new vacancy defects in the graphene lattice, which has been proven effective to create angstrom-scale pores for molecular sieving [44,205,206]. Our protocol for O_3-etching yields small nanopores (~3–4 Å) which are too small to permit transport of hydrated cations because of the involved high energy barrier to enter the pore (~40–240 kJ/mol) [207,208], as suggested by previous simulation studies. To resolve this issue, we employed CO_2 as a post etchant to expand the pores. Based on the recent studies [54,209] on the reaction kinetics of CO_2 with graphene lattice, CO_2 could provide slow expansion of the pre-existing nanopores (few atoms per second) without new nucleation events in graphene because of the high energy barrier for CO_2 to nucleate defects (~5.0 eV) [210] and relatively lower energy barrier for expansion (~ 2.7 eV) [54,211]. To initiate the pore expansion, the graphene/Cu substrate hosting the pre-existing O_3-etched pores was exposed to CO_2 at 800 °C in H_2 atmosphere (**Figure 3.1a**). The pore etching rate of graphene by CO_2 is pore-size dependent and decreases with the decreasing size of the defects [54,209]. Therefore, considering our small starting pores (3–4 Å), the etching rate was presumably slower than 0.25 nm/min at 800 °C [54]. Based on the above discussion, we chose to carry out pore expansion with 5 min and 8 min of CO_2 etching, which were expected to result in nanopores approaching the size of hydrated ions.

Chemically etched graphene using O_3 usually leaves behind oxygen-containing functional groups on the graphene basal plane and pore edges after etching [44,97]. To understand the surface chemistry behind the two-step pore etching, XPS measurement was performed to analyze the chemical states of the resulting graphene nanopores after thermally annealing the CO_2-treated graphene inside the XPS chamber to desorb contaminants such as hydrocarbons and water. As a control, as-synthesized graphene without postsynthetic etching was considered, which showed negligible oxygen concentration in the C1s spectrum (**Figure 3.1b**). In contrast, graphene after CO_2 treatment exhibited the presence of 3.0% C–O (~ 286 eV) in the C1s spectrum. A low concentration of oxygen on graphene was expected because of the thermal decomposition of those functional groups at 800 °C in a reducing environment [212,213]. In general, the C–O peak found on previously reported O_3-treated graphene could be assigned to epoxy/hydroxyl bonded carbons on the graphene lattice and ether groups at lattice and edge sites [153]. It has been reported that epoxy groups start decomposing around 150–200°C [152,213], while the decomposition of hydroxyl and ether groups are activated from approximately 800 °C [213] and 735 °C [214], respectively. Therefore, it is reasonable to postulate that the C–O peak has a contribution from both the hydroxyl and the ether groups. The relative composition of these functional groups can be analyzed by the O1s peak. However, it was challenging to deconvolute O1s in the graphene/Cu sample because of the contribution from copper oxide from the catalytic Cu substrate, formed by the oxidation of Cu during O_3 and CO_2 treatment. To resolve this, we carried out the CO_2 etching on freshly cleaved highly-oriented pyrolytic graphite (HOPG). Deconvolution of the resulting spectrum (**Figure 3.1d**) indicates two distinct peaks at 533.4 eV and 532 eV. These two peaks in the O1s spectrum corresponded to the presence of the C–O bonding, consistent with the observation in C1s spectrum of CO_2-etched graphene (**Figure 3.1c**). The former was assigned to the ether-boned aromatic carbon, while the latter was attributed to the hydroxyl groups. The origin of hydroxyl groups may come from the generation of reactive defects during CO_2 exposure and their subsequent oxidation by oxygen or water in the air [215,216].

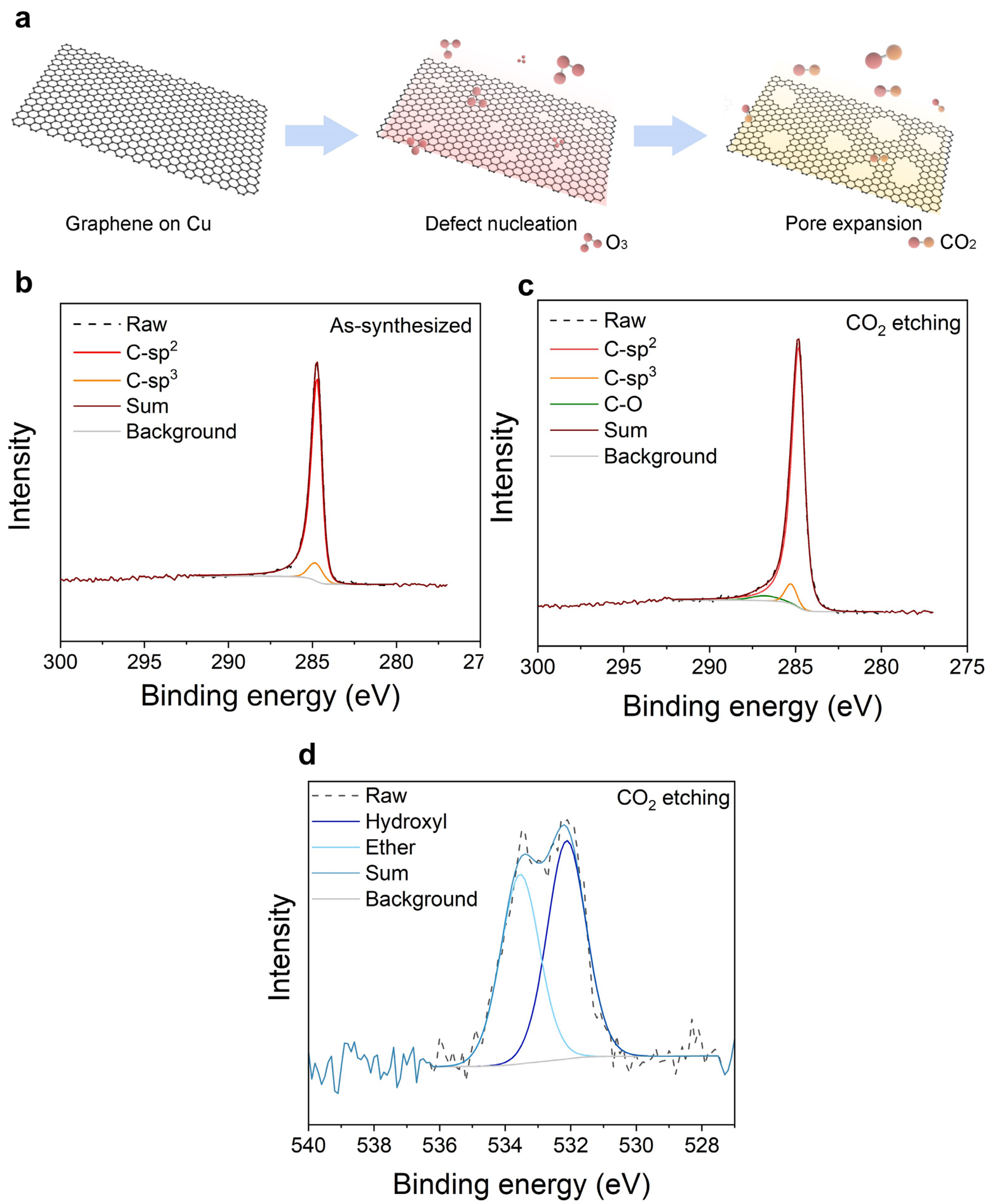

Figure 3.1. Creation and characterization of graphene nanopores using a decoupled nucleation/expansion method. (a) Schematic of the decoupling method. (b) C1s spectra of as-synthesized graphene and (c) C1s spectra of graphene after O_3 treatment followed by 5 min of CO_2 etching. (d) O1s spectra of HOPG after O_3 treatment followed by 5 min of CO_2 etching. Prior to each XPS measurement, the samples were heated in-situ up to 400 °C in the XPS chamber to remove contamination.

Next, STM was performed directly on the CO_2-etched graphene nanopores on Cu to understand the density and size distribution of the carbon vacancies. To obtain a smooth surface for STM imaging, the samples were annealed at 900 °C in a H_2 atmosphere. The resulting images (**Figure 3.2a–d**) revealed a high surface roughness of copper that limited the observation of the atomic structure. However, nanopores with sub-nanometer sizes were present on graphene/Cu with a dark contrast in the topography images. We estimated the pore size by analyzing the cross-section profile of the observed nanopores (**Figure 3.2e**). The pore size was determined using a straight line segment that passes through the center of the pore and whose endpoints lie on the dark contrast (red crosses in **Figure 3.2c and e**). Since STM imaged the electron density of the atoms, the measured pore size reflected the effective electron density gap that allows the transport of the molecules. We found that the mean pore size for the sample prepared by 5 min of CO_2 etching was 8.0 Å (standard deviation: 1.5 Å) with a pore density of ~ 10^{12} cm^{-2} (**Figure 3.2f**).

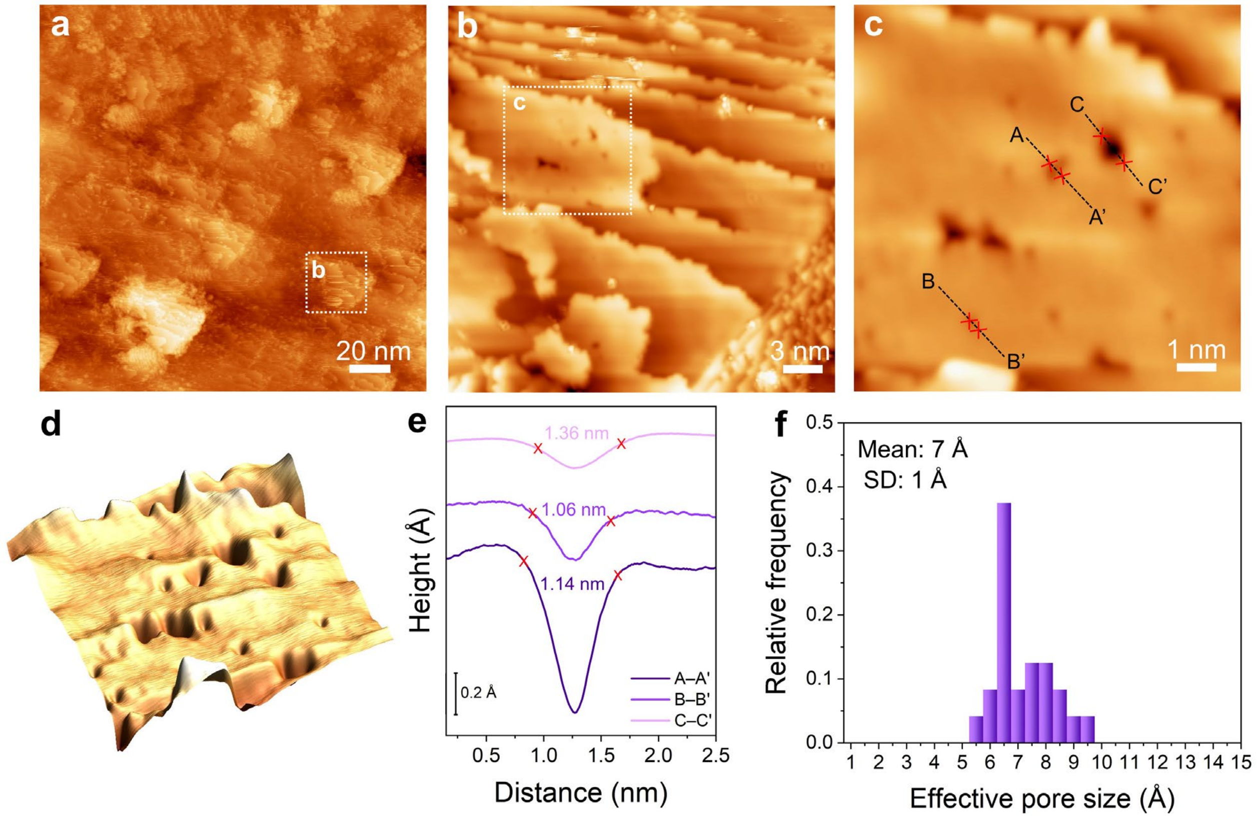

Figure 3.2. STM analysis of graphene nanopores etched by CO_2. (a–c) STM images of nanoporous graphene on Cu foil prepared by 5 min of CO_2 etching. (d) 3D landscape of nanoporous graphene/Cu shown in (c). (e) Cross-section profiles along lines A–A', B–B', and C–C'. (f) Pore size distribution of graphene nanopores etched by 5 min of CO_2 etching.

3.3.2 Ion permeation across graphene nanopores

The nanoporous graphene membranes were prepared by reinforcing graphene with a two-layer composite film (**Figure 3.3a)**. We refer to this composite film as the support film in the following discussion. The support film was composed of a NPC layer hosting 20–30 nm apertures and a thin Nafion layer. Compared to nanoporous graphene, the support film provides a much lower transport resistance, and it is non-selective to ions due to the large pore size in the carbon layer and the intrinsic property of Nafion layer [17,130]. It was used as a mechanical reinforcement for graphene to assist crack-free transfer. The resulting membrane was mechanically robust and could be suspended on a PTFE washer without any visible tears (**Figure 3.3b**). SEM images showed that the support had a smooth surface and a distinguishable layer-by-layer structure, where the upper Nafion layer was dense, and the lower carbon layer was porous (**Figure 3.3e and f**). Furthermore, optical profilometry revealed that the graphene/support film was 748±39 nm thick (**Figure 3.3c**).

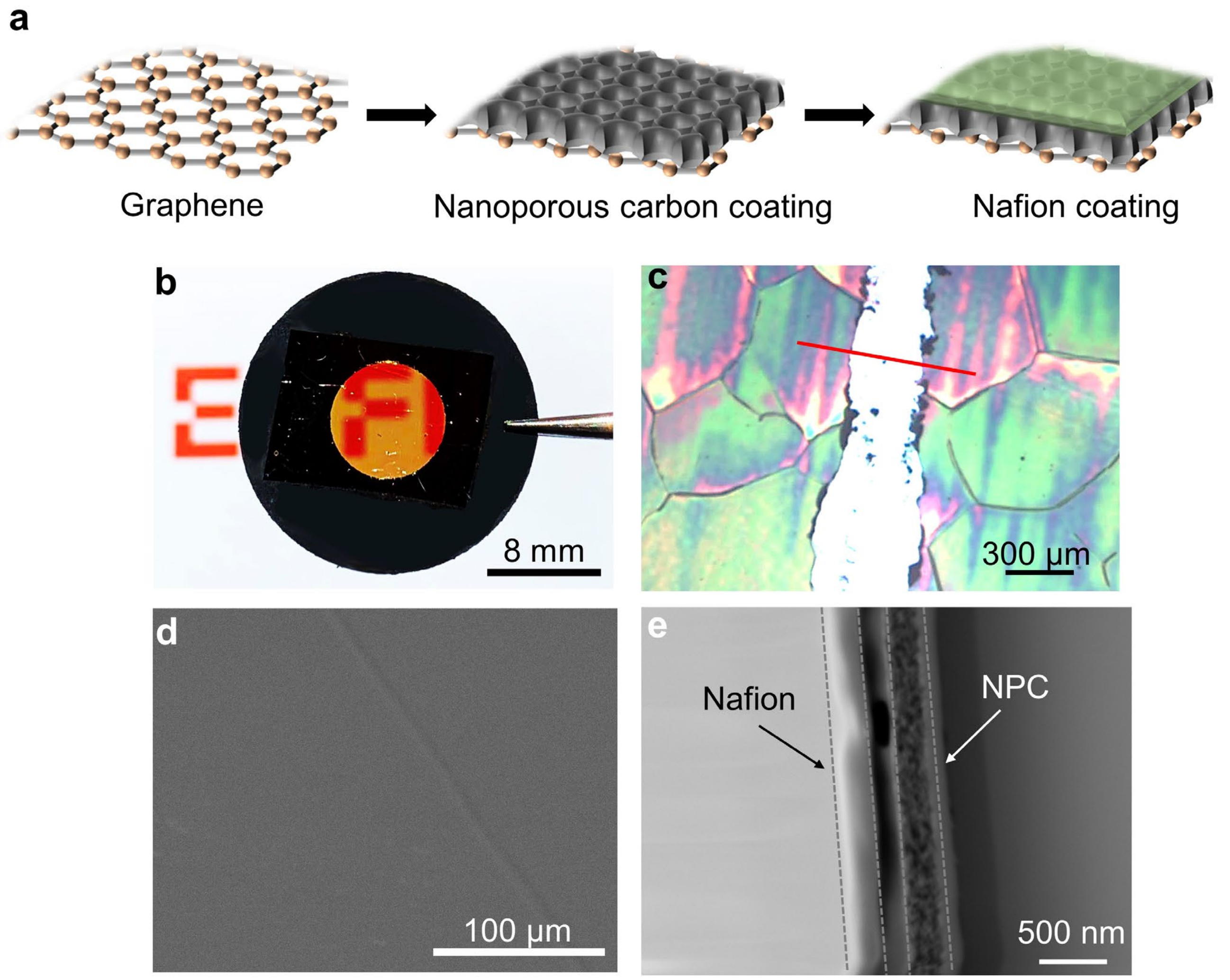

Figure 3.3. Characterization of nanoporous graphene membranes used to study ion transport. (a) Schematic of the fabrication of nanoporous graphene reinforced by a nanoporous carbon (NPC) and a Nafion layer. (b) Photograph of the membrane suspended on a PTFE washer. (c) Optical image of the membrane under profilometry measurement. The red

line denotes where line scan profiles are taken. (d) SEM image of the top view of the membrane. (e) Cross-section of the membrane.

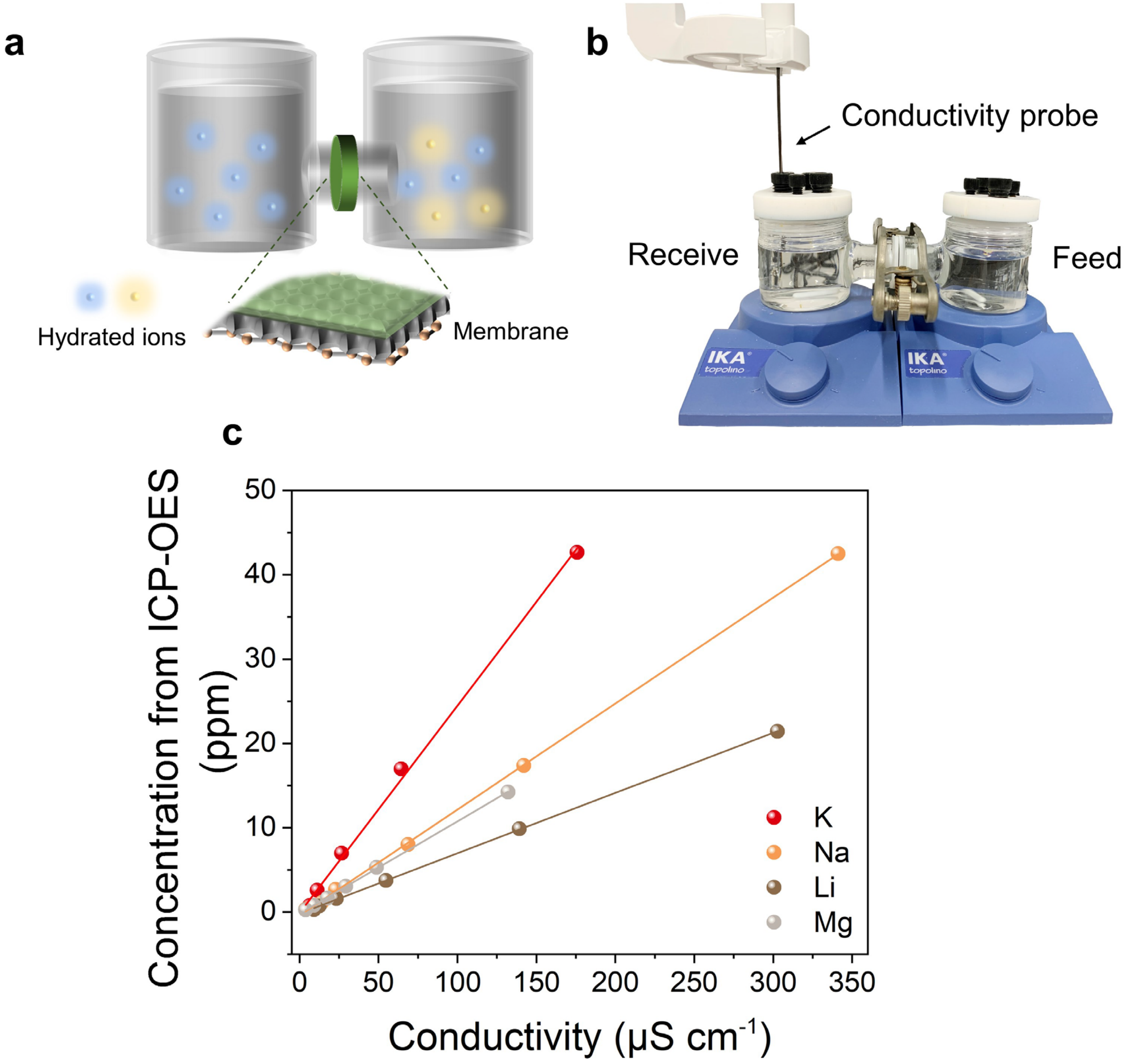

Figure 3.4. Setup for diffusion tests. (a) Schematic of the diffusion cell used in this study. (b) Photograph of the diffusion cell used to study ion transport across nanoporous graphene membrane. (c) Calibration of the conductivity probe versus concentration determined by ICP-OES. The R^2 values of K, Na, Li, Mg are 0.998, 0.999, 0.999, and 0.997, respectively.

The behavior of the cations passing through the graphene nanopores was studied using the forward osmosis of ions. The graphene/support film was sandwiched between two 50 mL chambers, and two washers were used to ensure a liquid-tight seal between the feed and the receiving chambers (**Figure 3.4a and b**). The feed side was filled with 1 M of salt solution (KCl, NaCl, LiCl, or $MgCl_2$, pH ~ 5.3), while the receiving side contained Milli-Q water (**Figure 3.5a**). Magnetic stirrers were used to mitigate the effect of concentration polarization. A conductivity probe was placed in the receiving chamber to monitor the ionic concentration as a function of time. The conductivity probe was calibrated with inductively coupled plasma-optical emission spectrometry (ICP-OES) to correlate the conductivity and the concentration (**Figure 3.4c**).

First, a control experiment was conducted by measuring the ionic diffusion through the support film (**Figure 3.5b**). As expected, the support films showed high cation diffusive fluxes but poor selectivities (K^+/Mg^{2+} and Li^+/Mg^{2+}~1–2), consistent with those reported in the literature [17]. Subsequently, we studied the ion transport through as-synthesized graphene hosting only intrinsic defects. It showed very small diffusive fluxes of four different cations (close to the detection limit of the conductivity probe), and no cation selectivity was observed. This could be attributed to the low density of the intrinsic defects (porosity of 0.025%) and uncontrolled pore sizes [7,26]. In contrast, the nanoporous graphene hosting O_3-etched defects showed almost ten times higher fluxes for all the studied ions than those of the as-synthesized graphene, but still exhibited a poor K^+/Mg^{2+} selectivity of 4. Previous studies [44,206] have reported that the size of the vacancy defects etched by O_3 from a pristine graphene lattice spans from 3–4 Å. Therefore, it is unlikely for ions to pass through these new vacancy defects due to a considerably high energy penalty [79,207,217]. Thus, we assigned the increase in the observed flux to the contribution from the expanded intrinsic defects or pore coalesce due to O_3 etching rather than from the new pores. The small population and the uncontrollable property of these intrinsic defects lead to again a poor ion selectivity. To resolve this issue, we employed CO_2 to create nanopores with controllable sizes for ion separation. **Figure 3.5b** shows that, after 5 min of CO_2 etching, the graphene membrane exhibited a much higher K^+ diffusive flux, which was 100-fold compared to the sample hosting intrinsic defects, and ten times higher than that of O_3-etched graphene. On the other hand, Mg^{2+} permeated much slower, with a diffusive flux close to that of graphene treated only with O_3, resulting in a significant improvement in the K^+/Mg^{2+} selectivity (maximum K^+/Mg^{2+} selectivity reached 70). In addition, the increase in the flux of other monovalent cations (Na^+, Li^+) was also rapid, and the transport rate of each ion was positively correlated to their hydrated diameters. We note that the observed trend could be linked to the pore size distribution estimated by STM, which showed that the majority of the pores etched by 5 min of CO_2 etching spanned 0.6–0.8 Å (**Figure 3.2f**), larger than the hydrated diameter of K^+ (6.6 Å) but smaller than the that of Mg^{2+} (8.6 Å).

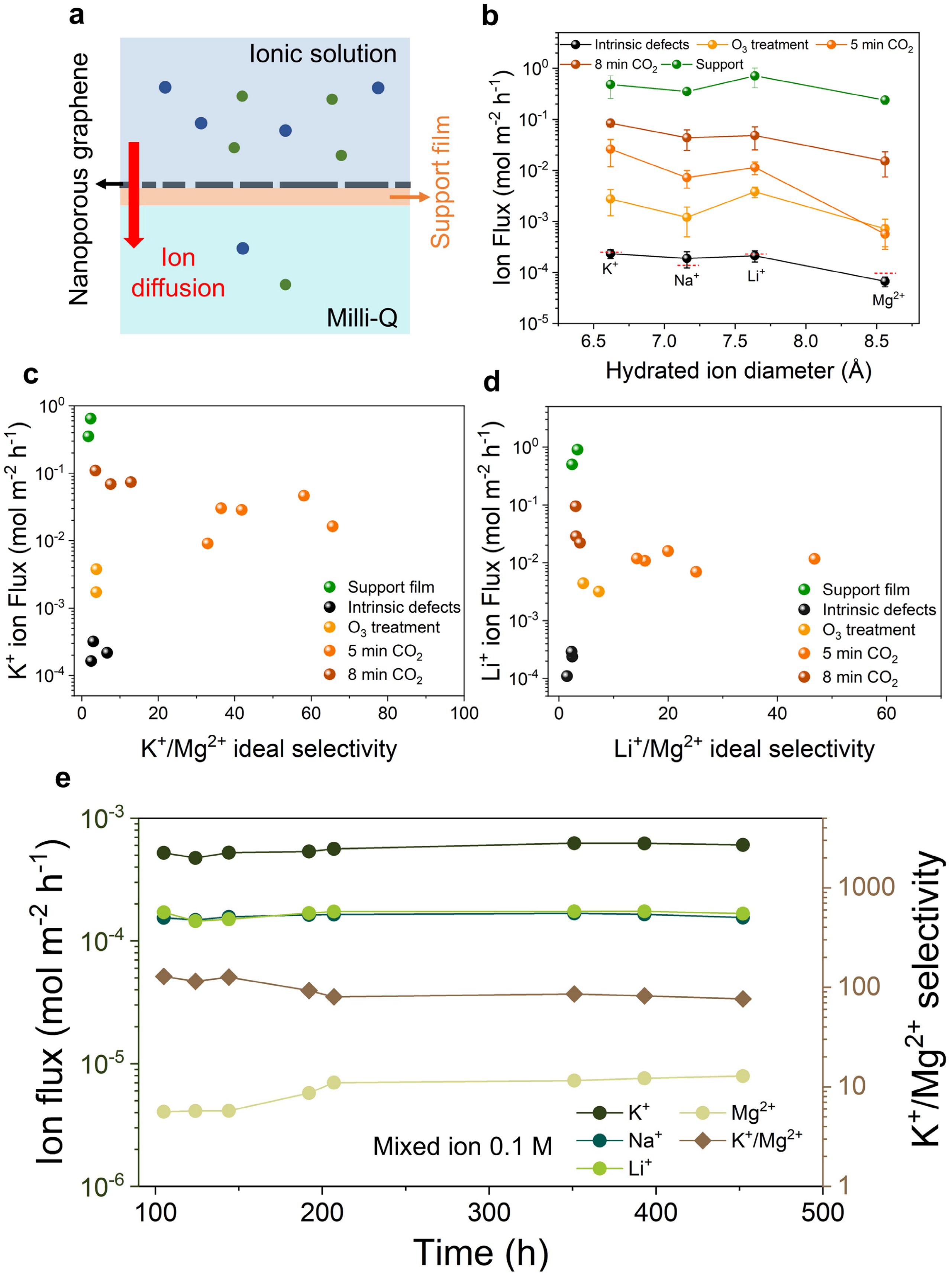

Figure 3.5. Measurement of ion diffusion across graphene nanopores. (a) Schematic of ion diffusion across the graphene nanopores. (b) Ion diffusive flux of samples with different postsynthetic etching as a function of the studied ions.

The red dashed lines indicate the detection limit of each ion using the conductivity probe. The error bars denote the standard deviation of two to five membranes prepared under the same etching condition. (c) K^+ ion diffusive flux versus K^+/Mg^{2+} for all the tested graphene membranes. (d) Li^+ ion diffusive flux versus Li^+/Mg^{2+} for all the tested graphene membranes. (e) Mixed-ion diffusive flux versus measurement time for a graphene membrane prepared by 5 min of CO_2 etching.

To further understand the correlation between the pore size and the cation diffusive flux, the CO_2 etching time was increased to 8 min to enlarge the nanopores. As expected, all the ions showed an increase in the diffusive flux (**Figure 3.5b**) due to the increased porosity in graphene. It is noteworthy that the improvement in the Mg^{2+} flux was more significant compared to those of other cations: a 20-fold increase was noted compared to that observed in the membrane treated with 5 min of CO_2 etching. In contrast, the K^+, $Na^{+,}$ and Li^+ diffusive fluxes increased less than 10-fold, thereby yielding a lower cation selectivity (maximum K^+/Mg^{2+} selectivity reached 13). Notably, Li^+ permeated faster than Na^+, although the hydrated diameter of Li^+ was slightly larger (Li^+: 7.6 Å versus Na^+: 7.2 Å). A higher Li^+ transport rate was also observed in other materials hosting sub-nanometer pores, which could be attributed to the pronounced ion dehydration effects or ion–pore interactions at the nanoscale [94,220,221]. Nevertheless, the increased fluxes and decreased selectivities after 8 min of CO_2 etching indicates that a small increase in pore size deteriorated the selectivity significantly. In addition, the cation diffusion rate with respect to the pore size suggests that the size-exclusion mechanism may be a critical factor for the observed high monovalent/divalent cation selectivities [17,199,207], which we further discussed in the following sections.

Figure 3.5c and d summarize the cation flux and M^+/Mg^{2+} (M: K, Li) selectivity of all the tested membranes. These results confirm that the observed high monovalent/divalent cation selectivity was contributed by the graphene layer. In addition, it is clearly seen that once the new pores were created in graphene through step-by-step etching of O_3 and CO_2, the ion permeance increased rapidly, while the selectivity first increased and then decreased. The best cation selectivity was achieved after 5 min of CO_2 etching, which showed a K^+/Mg^{2+} selectivity of 35–70 with the K^+ flux ranging from 1×10^{-2}–7×10^{-2} mol m^{-2} h^{-1} and a Li^+/Mg^{2+} selectivity of 18–50 with the Li^+ flux ranging from 6×10^{-3}–2×10^{-2} mol m^{-2} h^{-1}. Our results demonstrate that tuning the pore size in graphene would effectively adjust the ion transport behavior and thus the selectivity. A high cation selectivity was also observed in a solution mixture containing 0.1 M of KCl, NaCl, LiCl, and $MgCl_2$ (**Figure 3.5e**), indicating the potential of nanoporous graphene in ion–ion separation applications. The membrane showed stable fluxes for each ion over a testing period of 450 h. High K^+/Mg^{2+} (~70) and Li^+/Mg^{2+} selectivities (~25) were preserved at the end of the measurement.

3.3.3 Adjustment of the molecular cutoff

To support the proposed size-limited ion transport across the graphene nanopores, we further reduced the pore size (molecular cutoff) in graphene and studied the ion diffusion behavior. While we demonstrated that using CO_2 for the pore expansion in graphene, a reverse pore shrinking process is possible by introducing a carbon precursor during etching [218,219]. This concept was showcased by mixing CH_4 with CO_2 in the etching process to regrow graphene in large vacancy defects that are not ion-selective, whose presence is reflected by the low ion selectivity in the O_3-treated graphene. In principle, the regrowth rate in a larger defect is faster than that in a smaller one due to the lower resistance for CH_4 to enter the pore [219]. Thus, the regrowth method enables the reduction in the number of non-selective pores before the pore expansion, leading to a narrower pore size distribution for a sharper size-exclusion cutoff for ion separation. Two samples subjected to the regrowth method showed a remarkable improvement in the selectivity, exhibiting K^+/Mg^{2+} selectivities of 255 and 345 and Li^+/Mg^{2+} selectivities of 220 and 264 (**Figure 3.6a** and **b**). The regrowth method once again indicates that the size-exclusion mechanism presumably dominates the high monovalent/divalent cation selectivity. It is noted that the cation fluxes were slightly lower than those of samples without regrown graphene in the large pores, which could be explained by the decreased porosity due to the pore shrinkage in graphene.

We compared our graphene nanopores with other ion-sieving materials based on the concentration-driven diffusion tests and found that our high selectivity exceeded those of commercial polymeric membranes and layered materials such as MXene. Furthermore, the performance of our ion-sieving graphene nanopores surpassed those reported in the previous studies (**Figure 3.6c**), being attributed to a sharp molecular cutoff ($\leq$ 8.0 Å) in the ensemble of the graphene nanopore subjected to 5 min of CO_2 etching (**Figure 3.2f**). This allows the transport of smaller hydrated monovalent cations while rejecting larger ions such as Mg^{2+}.

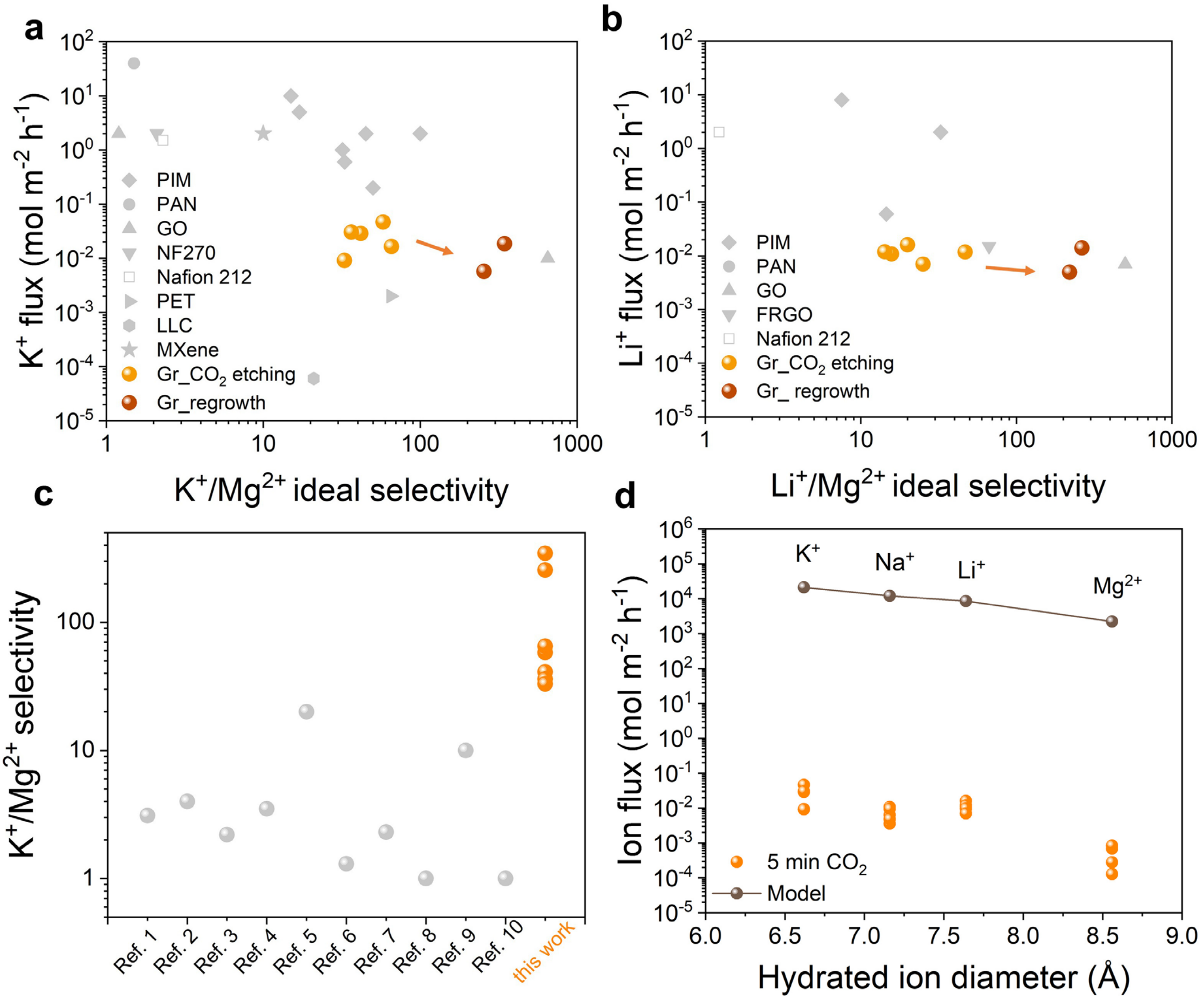

Figure 3.6. Ionic sieving in graphene nanopores and other materials. (a) Comparison of K^+ ion flux and K^+/Mg^{2+} selectivity and (b) Li^+ ion flux and Li^+/Mg^{2+} selectivity based on typical ion separation data of commercial polymeric membrane, other materials, and our study. (c) Comparison between typical ion separation data of graphene/MoS_2 nanopores reported in ref. 1 [47], ref. 2 [96], ref. 3 [220], ref. 4 [7], ref. 5 [221], ref. 6 [22], ref. 7 [24], ref. 8 [222], ref. 9 [28], ref. 10 [202], and our study. (d) Modeling cation flux using continuum theory in comparison with the nanoporous graphene membranes prepared by 5 min of CO_2 etching.

3.3.4 Modeling the ion flux across the nanopore

We further used a continuum analysis to understand the ion transport behavior from the graphene nanopores. Given the high ion flux and low selectivity of the support film, we can assume that the graphene layer dominates the overall ion transport. Here the graphene nanopore is assumed to be neutral at the pH range in this study (see the discussion in **section 3.3.5**), and the change in the concentration in the receiving chamber is considered negligible compared to the feed concentration. Under these assumptions, the cation flux, J_+, and the anion flux, J_-, across the nanopore are described by Nernst-Planck equation:

$$J_{\pm} = -D_{\pm}(\nabla C_{\pm} + C_{\pm} Z_{\pm} \frac{F\nabla \psi}{RT}) \qquad \textbf{(Equation 3.3)}$$

where D_+ and D_- are the diffusion coefficients of the cation and anion in the bulk solution, C_+ and C_- are the cation and anion concentration near the pore mouth, Z_+ *and* Z_- are the magnitude of the cation and anion charge, F is the Faraday constant, $\nabla \psi$ is the electric potential gradient across the nanopore, R is the gas constant , and T is the temperature.

Thus, the net current, I, generated due to the ion diffusion, can be written as:

$$I = |Z_+|J_+ - |Z_-|J_- \qquad \textbf{(Equation 3.4)}$$

Given the neutral nanopore and the electroneutrality of the system in this model, the net current flow of cation and anion, I, is zero. This fact allows $\nabla \psi$ in the cation flux expression in **Equation 3.3** to be rewritten using **Equation 3.4**:

$$J_+ = -(\frac{2D_+D_-}{D_+ + D_-}\nabla C_+) = -(D\nabla C_+) \qquad \textbf{(Equation 3.5)}$$

where $D = \frac{2D_+D_-}{D_+ + D_-}$. Here we use the fact that $C_+ = C_-$ and $|Z_+| = |Z_-|$ for 1:1 electrolyte to obtain **Equation 3.5.**

On the other hand, for 1:2 electrolyte (i.e., $MgCl_2$), the cation flux is written as:

$$J_+ = -(\frac{3D_+D_-}{2D_+ + D_-}\nabla C_+) = -(D'\nabla C_+) \qquad \textbf{(Equation 3.6)}$$

where $D' = \frac{3D_+D_-}{2D_+ + D_-}$. Here we use the fact that $2C_+ = C_-$ and $|Z_+| = 2|Z_-|$ to obtain **Equation 3.6.**

Equation 3.5 and **Equation 3.6** show that, without the presence of an external electric field and charges, the ion transport across the nano pore is governed by the concentration gradient of the ions. In this case, the theoretical transport resistance of a cation across a graphene nanopore, R, can be written as [91]:

$$R_{tot} = R_{access} + R_{pore} = \frac{1}{D}(\frac{1}{d} + \frac{4L}{\pi d^2}) \qquad \textbf{(Equation 3.7)}$$

where R_{tot} is the total transport resistance of a nanopore, R_{access} is the access resistance, R_{pore} is the pore channel resistance, d is the pore diameter, and L is the length of the graphene nanopore. D is replaced by D' when Mg^{2+} is considered.

It is clearly seen that the transport resistance is geometry-dependent. By determining R_{tot}, one can estimate the cation permeation rate, n, from the nanopore using a circuit analogy as:

$$n = \frac{driving\ \ force}{R_{tot}} = \frac{\Delta C}{R_{tot}} \qquad \textbf{(Equation 3.8)}$$

where ΔC is the concentration difference across the graphene nanopore.

Equation 3.8 calculates the contribution of a single graphene nanopore. To estimate the cation flux of a membrane, J_{th}, we use the pore size distribution and pore density estimated via STM study (**Figure 3.2f**) and combine them in **Equation 3.9**:

$$J_{th} = \sum_{d_i > d_{ion}} p_i n_i \qquad \textbf{(Equation 3.9)}$$

where p_i is the areal density of pores with diameter d_i, n_i is the cation permeation rate of pores with diameter d_i. Here we only consider the contribution of those pores whose sizes are larger than the hydrated diameter of the studied ion, d_{ion}. In addition, because the porosity of the graphene is very low (~ 1%), we assume that the fluxes through neighboring pores do not interfere.

The predicted cation fluxes are compared to experimental data in **Figure 3.6d**. We note that the continuum theory considering only size effect yielded ion fluxes that are 6–8 orders magnitude higher than those membranes prepared by 5 min CO_2 etching. On one hand, the fact that the pore size distribution estimated by STM analysis may not reflect the actual situation cannot be ruled out as the explanation of results in **Figure 3.6d**. On the other hand, the overestimation in the continuum model indicates that ion permeation across nanopores may not purely be a geometric effect. Indeed, it is well known that ions are hydrated in water [230], and thus the dynamics of the hydration shell should play an important role in ion transport under nanoscale confinement [217,231]. We showed that the majority of the pores in 5 min CO_2-etched graphene (**Figure 3.2f**) indeed are smaller than the hydrated diameter of Mg^{2+}. Hence, Mg^{2+} is likely to be partially dehydrated [13,207] while passing through the pore in a subcontinuum flow regime [91]. We speculate that the large discrepancy in Mg^{2+} flux between the theoretical prediction and the experiment is associated with the fact that Mg^{2+} has considerably higher dehydration energy compared to other monovalent cations (**Table 3.1**), as many studies revealed that ion dehydration at the pore entry is the main contribution to the apparent energy barrier to permeation [13,223,224].

Table 3.1. Experimental hydration free energy and hydrated diameter of different ions [225].

Ion	Hydrated diameter (Å)	Absolute hydration energy (kJ/mol)
K^+	6.6	321
Na^+	7.2	405
Li^+	7.6	515
Mg^{2+}	8.6	1592

3.3.5 Mechanism of ion transport through graphene nanopores

To gain insight into the distinct transport behavior of monovalent and divalent cations in our graphene membrane, we carried out ion diffusion tests at different temperatures and used an Arrhenius-type equation to extract the apparent activation energy, $E_{a,app}$:

$$J = A\exp\left(\frac{-E_{a,app}}{RT}\right) \qquad \textbf{(Equation 3.10)}$$

where J is the measured cation diffusive flux, A is the pre-exponential factor, R is the universal gas constant, and T is the temperature.

All studied ions (K^+, Na^+, Li^+, and Mg^{2+}) showed temperature-activated diffusive fluxes from a membrane prepared by 5 min of CO_2 etching (**Figure 3.7a**). This is consistent with recent theoretical studies that ions should have high energy barriers to permeate nanopores with diameters <10 Å s because of the required partial dehydration for the entry [224,229,230]. Notably, the calculated $E_{a,app}$ positively correlated to both the hydration energies and the hydrated ion diameters (**Figure 3.7b** and **Table 3.1**). Specifically, $E_{a,app}$ for the monovalent ions, K^+, Na^+, and Li^+ were 36, 33, and 50 kJ/mol, respectively (**Figure 3.7b**). $E_{a,app}$ of K^+ was slightly higher than that of Na^+, resulting in discrepancy between hydration energies and $E_{a,app}$ within monovalent cations. This may be attributed to the fact K^+ and Na^+ have relatively similar hydration energy compared to other cations, and the complex dynamics of hydration shell and pore–ion interaction would lead to the observed discrepancy, as reported by previous simulation works [13,95]. Nevertheless, it is clearly seen that compared to monovalent cations, Mg^{2+} required a much larger $E_{a,app}$ of 87 kJ/mol.

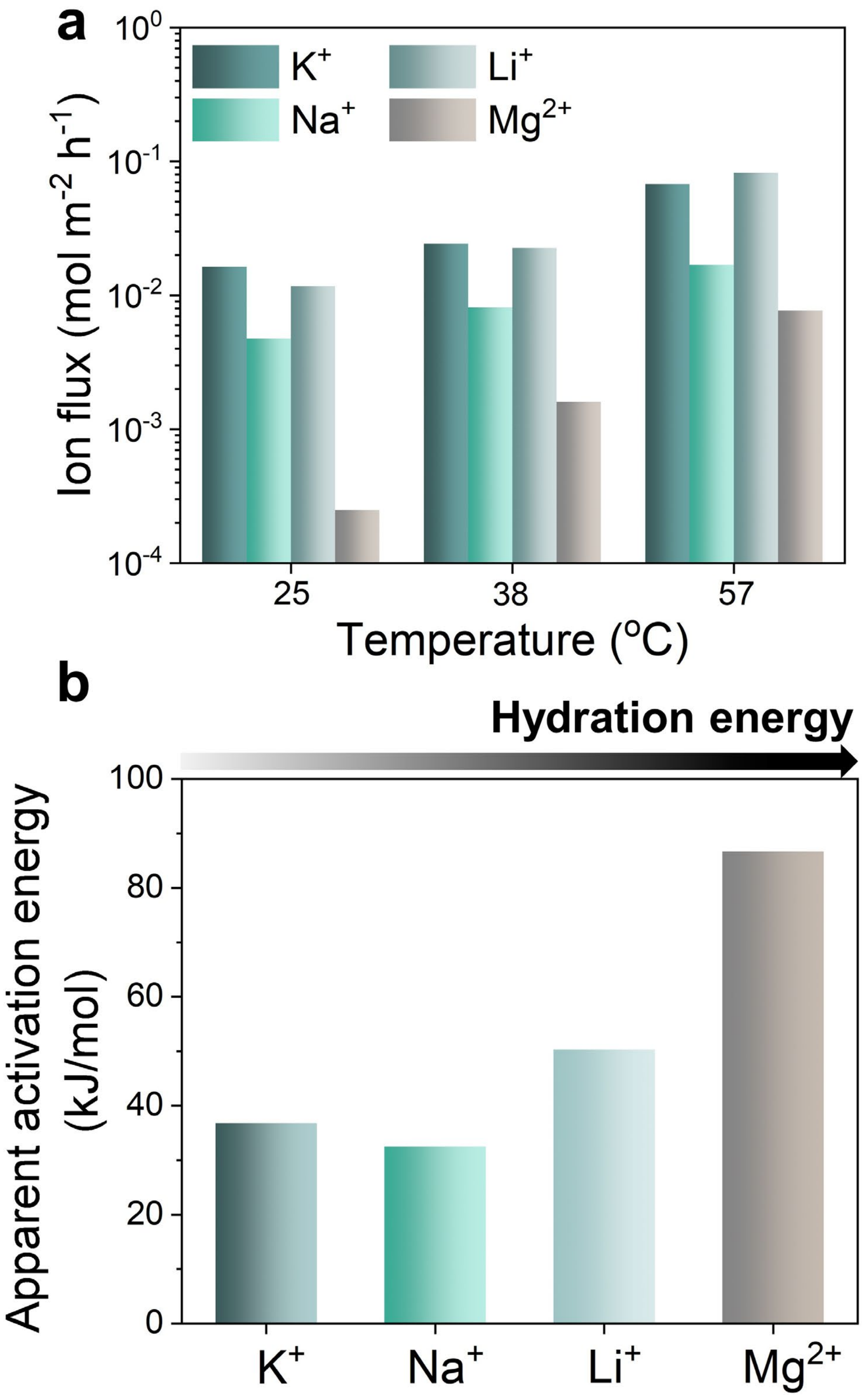

Figure 3.7. Experimental energy barriers for K$^+$, Na+, Li$^+$, and Mg^{2+}. (a) Cation diffusive flux of graphene nanopores subjected to 5 min of CO_2 etching as a function of temperature. (b) Apparent activation energy of different ions passing through the graphene nanopores subjected to 5 min of CO_2 etching.

According to Sahu *et al.* [226], the ion-dependent free energy barrier results from both the dehydration process and the pore geometry. The mechanism of partial dehydration on ion transport can be elaborated as follows. Ions with higher valence (e.g., Mg^{2+}) have stronger electrostatic interaction between the surrounding waters and the ion itself compared to ions with lower valence and thereby, have higher dehydration energy. For those ions with higher hydration energy, it is more difficult for them to remove water from the hydration shell for size adjustment while permeating through the nanopore comparable to the size of hydrated ions because of the high energy cost of dehydration. In contrast, ions with lower valence (e.g., K^+) could easily transport across the nanopore at the expense of lower energy required to remove water from the hydration shell. This explains the fact that $E_{a,app}$ is considerably larger for Mg^{2+} compared to other monovalent ions (**Figure 3.7b**). The overall partial dehydration effect in a microscopic picture leads to a size exclusion effect seen macroscopically in geometry-dependent cation selectivity (**Figure 3.5b**) [13,207,217]. In addition, Abraham *et al.* [13] reported that the dehydration effect in the free energy barriers is sensitive to the geometry, and this impact is significantly diminished once the hydrated ions are smaller compared to the confinement size. Their observation may explain what we saw after enlarging the nanopores with a longer CO_2 etching time: the improvement in Mg^{2+} flux was more pronounced than in other monovalent cations (**Figure 3.5b**). Overall, the agreement between our experimental findings and previous studies suggests that the monovalent/divalent cation selectivity of the nanopores could be explained by the size-exclusion effect associated with the ion-dependent dehydration process.

We note that electrostatic interaction between the nanopore rim and the ions is reported to be one of the mechanisms that govern ion transport [94]. In principle, graphene nanopore could be negatively charged due to the deprotonation of functional groups and surface contamination in the aqueous solution [28,47,96]. However, it has been reported that ether and hydroxyl groups bonded to graphene lattice are weak acid (pKa > 10) [227–229], and thus it is likely that those functional groups remained neutral during the ion diffusion test (solution pH ~ 5.3) rather than being deprotonated. In addition, the surface containments are often hydrocarbons which have very high pKa [229], unlikely to be the source of charges. On the other hand, the presence of oxygen-containing groups can indeed form permeant dipole moments which may interact with the ions [230]. Nevertheless, XPS measurement (**Figure 3.1c**) showed that the oxygen concentration was very low (~ 3.0%) on CO_2-etched graphene, and this would make the overall dipole–ion interaction small in magnitude. Therefore, we postulate that it may be negligible in our case. However, the details of charges/dipole on graphene nanopores require further investigation using other characterization approaches such as measuring the ionic conductance of graphene nanopores. Interestingly, Rollings *et al.* [47] reported K^+/Mg^{2+} selectivity of 1–4 from a single, negatively charged (-0.6 C m^2) graphene nanopore with the diameter spanning from 3–50 nm. Their results indicate that the presence of charges may not govern the cation selectivity, and it is less sensitive to the pore size [226], which is opposite to our case. Thus, the discussion above suggests that electrostatics may not be the primary factor of the high monovalent/divalent cation selectivity seen in our graphene membranes.

3.4 Conclusion

Size adjustment of 2D confinement in graphene to achieve a specific molecular cutoff for desirable ion separation was realized using a decoupled pore nucleation/expansion approach. We successfully demonstrated that by precisely tuning the pore size in graphene, unprecedentedly high K^+/Mg^{2+} and Li^+/Mg^{2+} selectivities could be achieved, which is believed to result from the size-exclusion mechanism associated with an ion-dependent dehydration process. Moreover, our membrane was able to withstand long-term forward osmosis for over 400 h, thereby demonstrating its potential for practical ion separation applications. However, the cation fluxes are relatively low compared to materials such as polymeric membranes because of the inherent low porosity of nanoporous graphene (~ 1 %). This could be improved by engineering the number of nuclei in the defect nucleation step in the pore etching process. Overall, our work opens a new pathway for developing atomically thin 2D nanopore platforms for fundamental hydrodynamics study as well as energy-efficient ion–ion separation applications such as redox-flow batteries and membrane-based lithium extraction.

Chapter 4 Centimeter-Scale Gas-Sieving Nanoporous Single-Layer Graphene Membrane

Adapted with permission from Wan-Chi Lee, Luc Bondaz, Shiqi Huang, Guangwei He, Mostapha Dakhchoune and Kumar Varoon Agrawal, Centimeter-scale gas-sieving nanoporous single-layer graphene membrane. ***Journal of Membrane Science****, 618, 118745, 2021. Copyright © 2021 Elsevier*

Wan-Chi Lee designed and performed the membrane fabrication, the gas permeation tests and the characterization, analyzed the data and wrote the paper with other authors.

Abstract

High-permeance, molecular-sieving, nanoporous single-layer graphene (NSLG) membranes are highly promising for gas separation. However, the formation of cracks during the transfer of NSLG to a low-cost porous support is difficult to avoid. These cracks are detrimental to gas selectivity, and therefore, make the scale-up of the gas-sieving NSLG membranes challenging. To mitigate the crack formation on low-cost macroporous supports, herein, we demonstrate mechanical reinforcement of the graphene film with a two-layer composite carbon film. The bottom layer of the composite film is a 100-nm-thick block-copolymer film derived nanoporous carbon (NPC) film with a pore size of 20–30 nm. This layer makes an intimate contact with NSLG and prevents generation of crack. However, the NPC film by itself is not robust enough to cover the rough surface of low-cost macroporous supports and tends to generate occasional cracks. This is prevented by spin-coating a 500-nm-thick multi-walled carbon nanotube (MWNT) film, hosting pore size of 200–300 nm, on top of the NPC film. This imparts enough mechanical strength of NSLG/NPC film to be successfully suspended on a low-cost, macroporous, nonwoven metal wire mesh on a centimeter-scale while completely avoiding cracks. As a result, H_2/CH_4 and H_2/CO_2 selectivities of 11–23 and 5–8, respectively, higher than the corresponding Knudsen selectivities of 2.8 and 4.7, respectively, are obtained from the centimeter-scale NSLG membranes. The reinforced membranes are mechanically robust and can successfully withstand transmembrane pressure difference of 4 bar. When the MWNT film is directly coated on NSLG without using the intermediate NPC layer, the gas sieving behavior is not observed, perhaps due to the development of nanoscale cracks. This underlines the crucial role of the hierarchical pore structure in the composite carbon film in realizing the gas-sieving graphene membranes.

4.1 Introduction

Atom-thick single-layer graphene (SLG) film incorporated with sub-nanometer pores enables high-flux yet selective molecular transport, and is promising for improving the energy-efficiency of water desalination [41,51,82,203,231] and gas separation [53,75,232–238]. However, a key bottleneck in the scale-up of nanoporous SLG (NSLG) membranes, especially for the gas separation, is the fabrication of large-area NSLG films without cracks and tears on low-cost porous supports. This is because the gas transport from a nanoscale crack in NSLG is several orders of magnitude faster than that from a molecular-sieving nanopore [239]. For example, the permeation coefficients of H_2 and CH_4 from a large non-selective defect (e.g. 2–50 nm in size) are within the same order of magnitude, ca. 10^{-18}–10^{-19} mol s^{-1} Pa^{-1} [70,240]. In comparison, the permeation coefficient of H_2 from a H_2-selective nanopore is much smaller, in the range of 10^{-21} to 10^{-22} mol s^{-1} Pa^{-1} [53]. The permeation coefficient of CH_4 from a H_2-selective nanopore, assuming H_2/CH_4 selectivity of 100 to 1000, is even smaller, lower than 10^{-24} [53]. As such, even a few ppm of nanoscale cracks in NSLG will significantly increase the CH_4 transport, deteriorating the gas selectivity.

The cracks and tears in the suspended graphene film originate during the transfer of graphene onto a porous support. The fabrication of NSLG-based membranes involves three key steps, (i) synthesis of SLG, (ii) incorporation of gas-selective nanopores in SLG and (iii) transfer of NSLG to a porous support. High-quality SLG with a low density of intrinsic defects is synthesized by chemical vapor deposition (CVD) of a hydrocarbon precursor on a Cu foil, a process that has been demonstrated on a scalable roll-to-roll basis [41,42]. Since the pristine graphene lattice is theoretically impermeable to molecules, molecular-selective nanopores with a narrow pore-size-distribution (PSD) in SLG are introduced by chemical or physical etching techniques [241,242]. Finally, NSLG is transferred from the Cu foil to the target porous support. It is this transfer step that leads to mechanical-stress-induced cracks and tears in the NSLG film [56,243,244]. Therefore, it is essential to provide mechanical reinforcement to the NSLG membrane, which at the same time helps to fulfill the requirement of membrane-based gas separation involving pressurization [245]. A strategy to achieve this is to integrate NSLG with a mechanically-reinforcing porous film that does not restrict the molecular transport across graphene. Naturally, the conventional and most popular poly(methyl methacrylate) (PMMA) [246] reinforcement of graphene is ruled out because PMMA has a small gas permeability and, therefore, would control the overall gas transport. In this regard, one can use a porous polymer film as the reinforcement. For example, a porous polymer film can be directly cast on top of graphene by the non-solvent induced phase separation (NIPS) process [236,244]. However, in this method, graphene contacts the bottom layer of the polymer film, and the presence of macrovoids or micron-sized pores in the bottom layer of the polymer film does not provide sufficient mechanical reinforcement, and cracks in the suspended graphene film develops during the NIPS process. We recently reported hydrogen-sieving NSLG membranes with 1 mm^2 area, using a block-copolymer-templated nanoporous carbon (NPC) film to reinforce graphene, with the resolution of molecular differentiation approaching 1 Å [234]. However, these membranes were fabricated on laser-drilled smooth tungsten foils which are difficult to scale up [247]. As we show here, the standalone NPC film tends to develop cracks when transferred onto low-cost macroporous supports which generally have a relatively higher surface roughness compared to the tungsten foil. Recently, Yuan and co-workers demonstrated a centimeter-sized single-walled carbon nanotube (SWNT) reinforced, crack-free NSLG membranes for nanofiltration, achieving Na$^+$ and Rhodamine B rejections of 85 and 97%, respectively [203]. Such reinforcement also allowed the construction of tubular water-desalination modules, yielding salt rejection up to 95.3%. Nevertheless, it is unclear that this method would lead to gas-sieving membranes because molecular diffusivity in the gas phase is four to five orders of magnitude larger than that in the liquid phase. Further, the size differences between the gas molecules are much smaller than those between water and hydrated ions. As we show later, we could not obtain a gas-sieving performance from graphene supported by a carbon nanotube mesh.

Herein, we report a method to fabricate centimeter-scale gas-sieving NSLG membranes on a commercial low-cost stainless-steel nonwoven mesh (pore size of 20 μm) where the mechanical reinforcement is provided from a two-layer composite carbon film. The bottom layer of the reinforcement is composed of a 100-nm-thick NPC film while the top layer is made up of a 500-nm-thick multi-walled carbon nanotubes (MWNT) film with a pore size ranging from 200 to 300 nm. The NPC film has a high affinity with graphene lattice while MWNT film is mechanically robust, improving the overall mechanical robustness of the composite film. As a result, centimeter-scale film could be prepared on low-cost macroporous support. The resulting films could withstand pressurization, and yielded attractive H_2/CH_4 and H_2/CO_2 selectivities of 11–23 and 5–8, respectively, significantly higher than the corresponding Knudsen selectivities.

4.2. Methods and materials

4.2.1 Synthesis of SLG by low-pressure chemical vapor deposition (LPCVD)

SLG was synthesized by the LPCVD process using a Cu foil (25 μm thick, 99.98% purity, Alfa-Aesar or 50 μm thick, 99.9% purity, Strem) as a catalytic substrate. Briefly, the Cu foil was subjected to CO_2 and H_2 annealing at 1000 °C for 30 minutes, respectively. Afterward, CH_4 (24 sccm) and H_2 (8 sccm) were introduced into the reactor at a total pressure of 460 mtorr for 30 minutes for the nucleation and growth of the polycrystalline SLG film. The quartz tube used as the LPCVD reactor was subsequently pulled out from the hot furnace at the end of the synthesis to rapidly quench the crystallization. The as-synthesized graphene was either directly used to fabricate membranes or was further treated by ozone to incorporate the gas-selective nanopores.

4.2.2 Fabrication of graphene/NPC/MWNT membranes

Nanopores in single-layer graphene were introduced by exposing as-synthesized graphene on Cu to a short ozone (9% in O_2) pulse at 250 °C (pulse FWHM < 0.3 s). The reinforcing layer of the graphene membrane was made by the deposition of an NPC film followed by the deposition of an MWNT film on top of the NPC film. The fabrication of the NPC film was similar to the procedure reported elsewhere [234]. Briefly, the precursor of NPC was prepared by dissolving 0.1 g block-copolymer (poly (styrene-b-4-vinyl pyridine), Polymer Source) and 0.2 g turanose (Sigma Aldrich) in dimethylformamide (Sigma Aldrich) followed by heat treatment of the solution at 180 °C. The solution was spin-coated on the graphene film and pyrolyzed at 500 ºC in a H_2 (15 sccm) /Ar (200 sccm) atmosphere, with a total pressure of 1 bar for 1 hour to yield the NPC film. It has a mix of somewhat interconnected as well as straight pore channels where the proportional is determined by the annealing of the block copolymer film. It hosts a pore size of 20–30 nm, which corresponds to a density of 10^{-3} nm^{-2} for the pores opening to the top surface. The MWNT coating suspension was prepared by dispersing MWNT powders (multi-walled, carboxylic acid functionalized, average diameter and length of 9.5 and 1500 nm, respectively, Sigma Aldrich) with surfactant (modified polyvinyl alcohol, XFNano, China) in dimethylformamide (Sigma Aldrich) at a weight ratio of 2:1 (20 mg/mL: 10 mg/mL). Following this, the suspension was sonicated for 3 hours to obtain a uniform dispersion (average length of 690 nm after the sonication). Subsequently, centrifugation was carried out to settle down the nondispersed MWNT and only the supernatant was collected. The MWNT film was deposited by spin-coating 0.5 mL of pre-dispersed suspension on top of the NPC reinforced graphene film at a spin speed of 1500 rpm for 1 minute. After the deposition, the sample was pyrolyzed at 500 °C in a H_2/Ar atmosphere for 1 hour. The resulting composite film was floated on a $Na_2S_2O_8$ bath (0.2 M in water) to etch the Cu foil. After Cu etching, the floating film was transferred to a deionized water bath to rinse the backside of the film. Finally, the rinsed film floating on water was scooped by a polished stainless-steel mesh (pore size 20 μm, TWP Inc., SKU #325X2300TL0014).

4.2.3 Characterization

Scanning electron microscope (SEM) images were obtained by using FEI Teneo scanning electron microscope at 1.0–5.0 kV and working distances of 2.5–5.0 mm. No conductive coating was applied to the substrates before SEM. Transmission electron microscope (TEM) imaging and selected area electron diffraction (SAED) of the composite graphene film were conducted by FEI Tecnai G2 Spirit Twin transmission electron microscope with a 120 kV incident electron beam. Raman measurement was carried on graphene on a Cu foil right after the synthesis and pore etching using 457 nm excitation or on graphene transferred to a Si/SiO_2 wafer using 532 nm excitation using Renishaw micro-Raman spectroscope with 100×objective. The obtained Raman data was analyzed using a MATLAB script. For the calculation of the D and the G peak height, the background was subtracted from the Raman data using the least-squares curve fitting tool (lsqnonlin).

4.2.4 Gas permeation test

The single-component and mixture gas permeation tests were carried out in a homemade permeation cell reported elsewhere [248]. The mass flow controllers (MKS and Brooks Instruments) were pre-calibrated using a bubble flow meter, delivering a pre-determined amount of gas to the feed side. The transmembrane pressure difference was varied between 1–4 bar with the permeate side maintained at 1 bar using an Ar sweep. The permeate was connected to a pre-calibrated mass spectrometer allowing real-time analysis of the permeate gas. The graphene membranes were sealed on to an annular metal disk using an epoxy-based sealant. Viton rings were used to ensure a gas-tight seal between the annular disk and the membrane module. The feed and sweep gas lines were preheated and the entire membrane module was heated inside an oven with high-temperature uniformity. The gas flux was calculated once the steady-state was reached. The permeance J_i of the gas was calculated according to **Equation 4.1**:

$$J_i = \frac{X_i}{A\Delta P_i} \qquad \textbf{(Equation 4.1)}$$

where X_i is the flow rate of gas i, A is the membrane area, and ΔP_i is the transmembrane pressure difference for the gas i. The selectivity (α_{ij}) of two gases, gas i and gas j, was calculated according to **Equation 4.2**:

$$\alpha_{ij} = \frac{(C_i / C_j)_{Permeate}}{(C_i / C_j)_{Feed}} \qquad \textbf{(Equation 4.2)}$$

where C_i is the concentration of gas i in a given stream.

4.3. Results and discussion

4.3.1 Fabrication of large-area graphene membrane

The procedure for preparing the reinforced NSLG membrane is shown in **Figure 4.1**. Briefly, the NPC film, hosting 20–30-nm-sized pores (**Figure 4.2**), was fabricated directly on top of the NSLG film using a block-copolymer based templating strategy [234]. An MWNT film was subsequently solution-cast on top of the NPC film, and the resulting composite film was annealed at 500 ºC to create a good adhesion. Following this, the Cu foil beneath NSLG was removed by etching in a $Na_2S_2O_8$ bath. The resulting floating NSLG/NPC/MWNT film was rinsed with water, and finally scooped by a macroporous, nonwoven metal wire mesh leading to the suspended NSLG membrane.

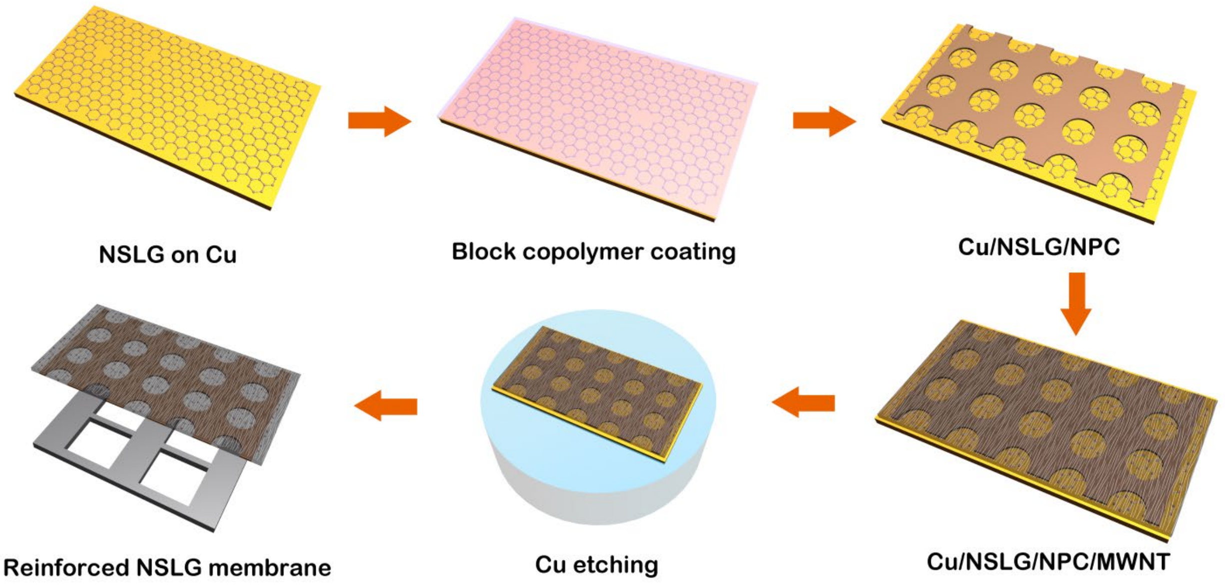

Figure 4.1. Schematic of the fabrication of large-area NSLG membranes using the composite NPC/MWNT film as a reinforcing layer. Briefly, a block-copolymer/turanose solution was coated on the NSLG film resting on a Cu foil. Pyrolysis was conducted to transform the coated film into NPC. Subsequently, an MWNT film was deposited on top of the NPC film. To fabricate membranes, Cu foil was etched out, leaving NSLG/NPC/MWNT film floating on a water bath. The floating film was finally transferred to the polished nonwoven wire mesh.

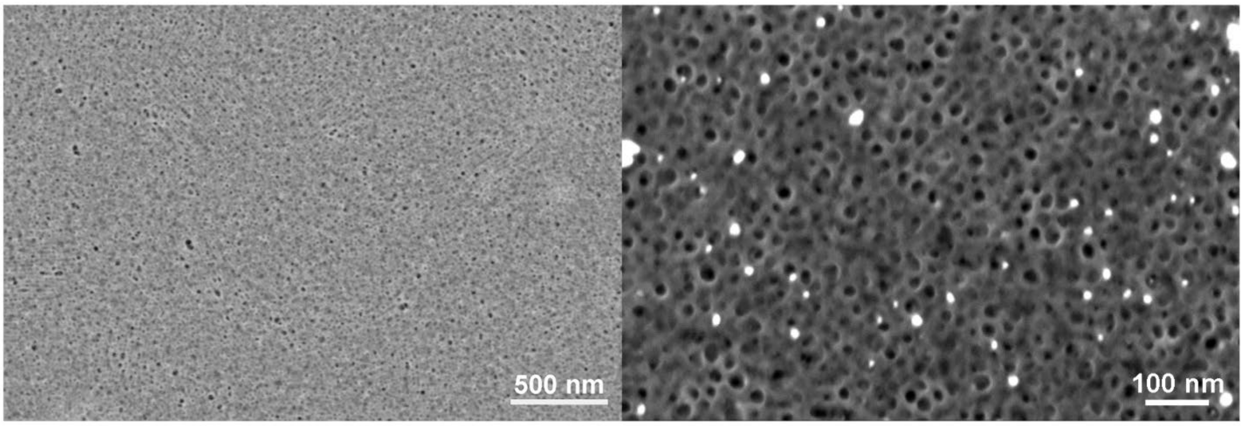

Figure 4.2. SEM images of the NPC film.

The standalone NPC film without the MWNT layer works well as the reinforcing support for NSLG, however, it requires a porous support with an extremely smooth surface such as a drilled metal foil which is difficult to produce with a large area and is not economically viable for the eventual scale-up. On the other hand, when using the metal wire mesh or a conventional inorganic porous support (**Figure 4.3**), we observed occasional cracks, occurring every few millimeters, in the NSLG/NPC film (**Figure 4.4a**). This is because these supports have, difficult to avoid, occasional 1 to 10 μm-sized surface protrusions, where the 100-nm-thick NPC film cracks. In this study, we overcome this obstacle by further reinforcing the graphene/NPC film with a thin MWNT layer. We chose the MWNT-based porous film as the reinforcing layer because the mesh-like carbon nanotube films have a high porosity allowing fast gas transport, as well as excellent mechanical properties [249–253]. The reinforced NSLG film could be transferred to a polished nonwoven stainless-steel mesh with a pore opening of 20 μm (**Figure 4.4b**). The suspended film was smooth and appeared to maintain its structural integrity (**Figure 4.4c** and **d**). No obvious cracks or tears were observed. A few-centimeter-long coupon of NSLG/NPC/MWNT film could be prepared on the stainless-steel mesh support (**Figure 4.4e**). A centimeter-wide film could be rolled up on a cylindrical quartz tube (2.5 cm in outer diameter) without inducing any visible cracks (**Figure 4.4f**). This indicated that the fabrication of spiral-wound NSLG-membrane modules by this method is promising.

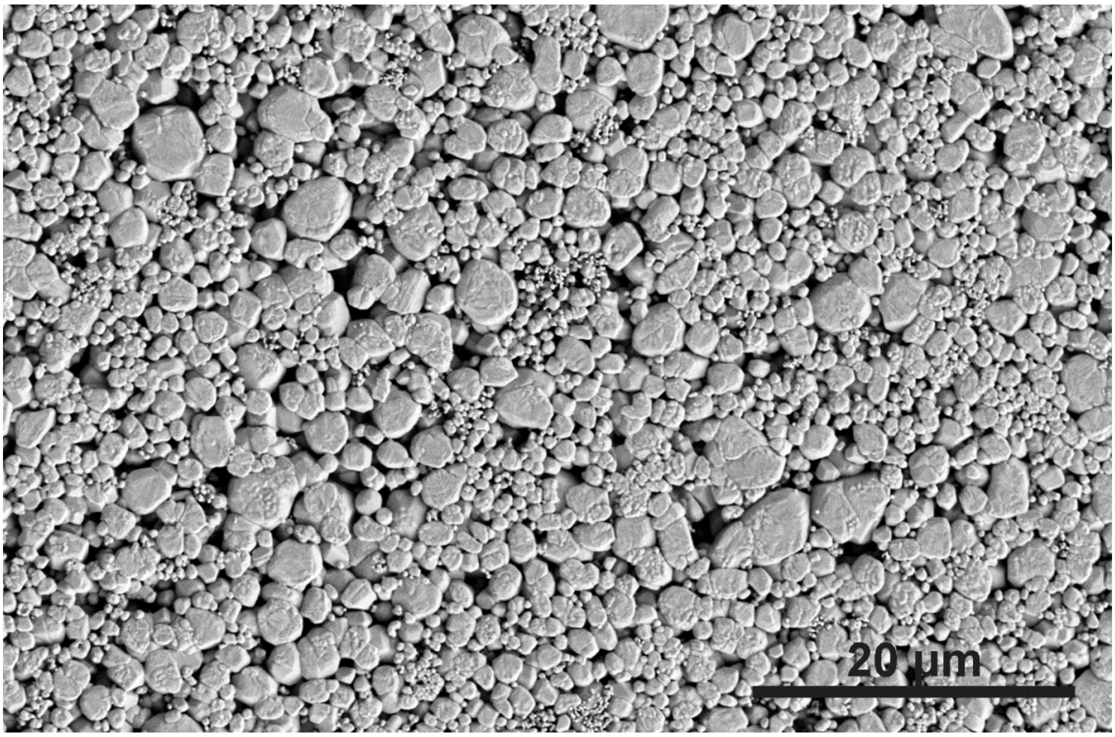

Figure 4.3. SEM image of sintered tungsten support.

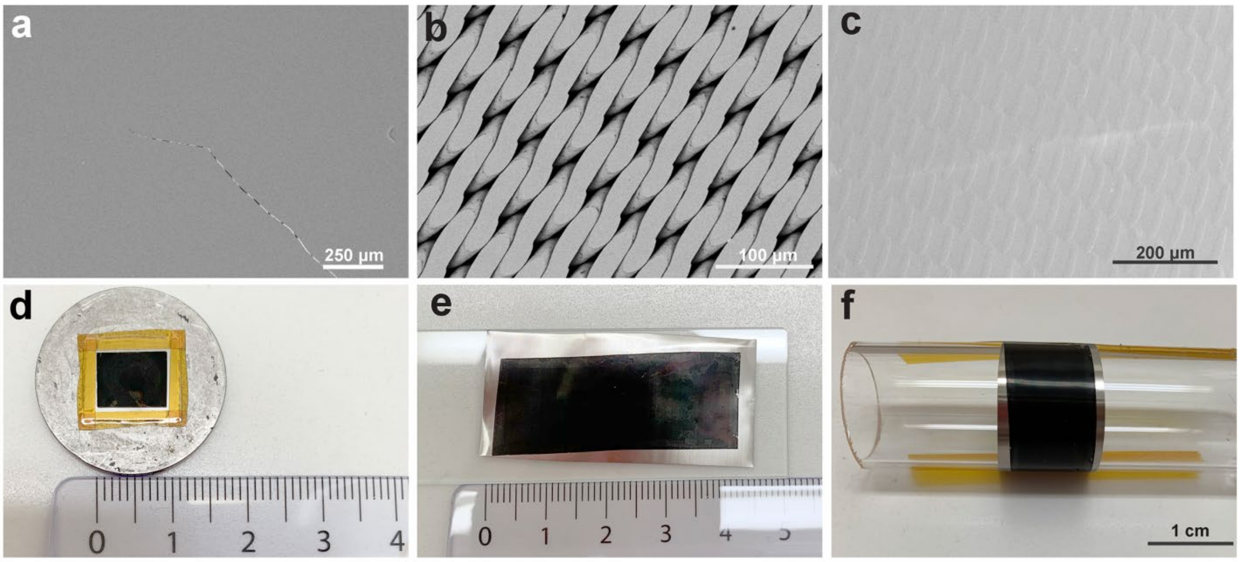

Figure 4.4. Characterization of the centimeter-scale graphene membrane. (a) NSLG/NPC film having cracks on the conventional metal support. (b) SEM image of the commercial nonwoven stainless-steel wire mesh after manual polishing of the top surface. (c) SEM image of the transferred NSLG/NPC/MWNT film on the metal mesh. (d) Photograph of a typical all-carbon NSLG membrane suspended on the stainless-steel wire mesh. (e) Photograph of a large-area all-carbon NSLG membrane lying flat and (f) rolled up on a cylindrical tube with an outer diameter of 2.5 cm. The units of the ruler in panels (d) and (e) are in centimeter.

The morphology of the NSLG/NPC/MWNT film was analyzed by scanning electron microscopy (SEM) which confirmed that the film was free from microscale cracks (**Figure 4.5a**). The top MWNT layer had a mesh-like structure with an interlocked array of nanotubes (**Figure 4.5b**), similar to the carbon nanotube mesh reported in the literature [254]. This relatively open mesh-like arrangement of the nanotubes is advantageous for gas transport, enabling gas molecules to diffuse across the film with low resistance. Selected area electron diffraction (SAED) from NSLG/NPC/MWNT film transferred on a transmission electron microscope (TEM) grid with 30 μm holes revealed a characteristic diffraction pattern of SLG, representing periodicities of 0.213 and 0.123 nm, on top of the diffraction rings from nanotubes (**Figure 4.5c**) [255]. We did not find an area in TEM grid where this characteristic diffraction pattern was not present, indicating that NSLG thoroughly adhered to the NPC/MWNT film. Flipping the composite film, we could observe the flat/smooth morphology of the NSLG film above the mesh-like structure of MWNT (**Figure 4.5d**). The thickness of the composite film was 500 nm. We did not observe any incidence of MWNT film peeling off from the NPC film during the transfer processes, indicating a strong affinity between the MWNT and the NPC films. This is likely due to (i) strong van der Waals and π-π interaction between NPC and MWNT[234] and, (ii) potential partial penetration of MWNT tips with a diameter of ca. 10 nm inside the 20–30 nm pores of the NPC film. Raman spectroscopy data, obtained from the flipped NSLG/NPC/MWNT film with graphene facing up, was dominated by the D and G peaks of the amorphous NPC film, and D, G, and 2D peaks of the MWNT film (**Figure 4.6**) [148]. Therefore, to extract information on the defect density of NSLG, Raman spectroscopy was carried out prior to the deposition step of NPC and MWNT films (discussed later).

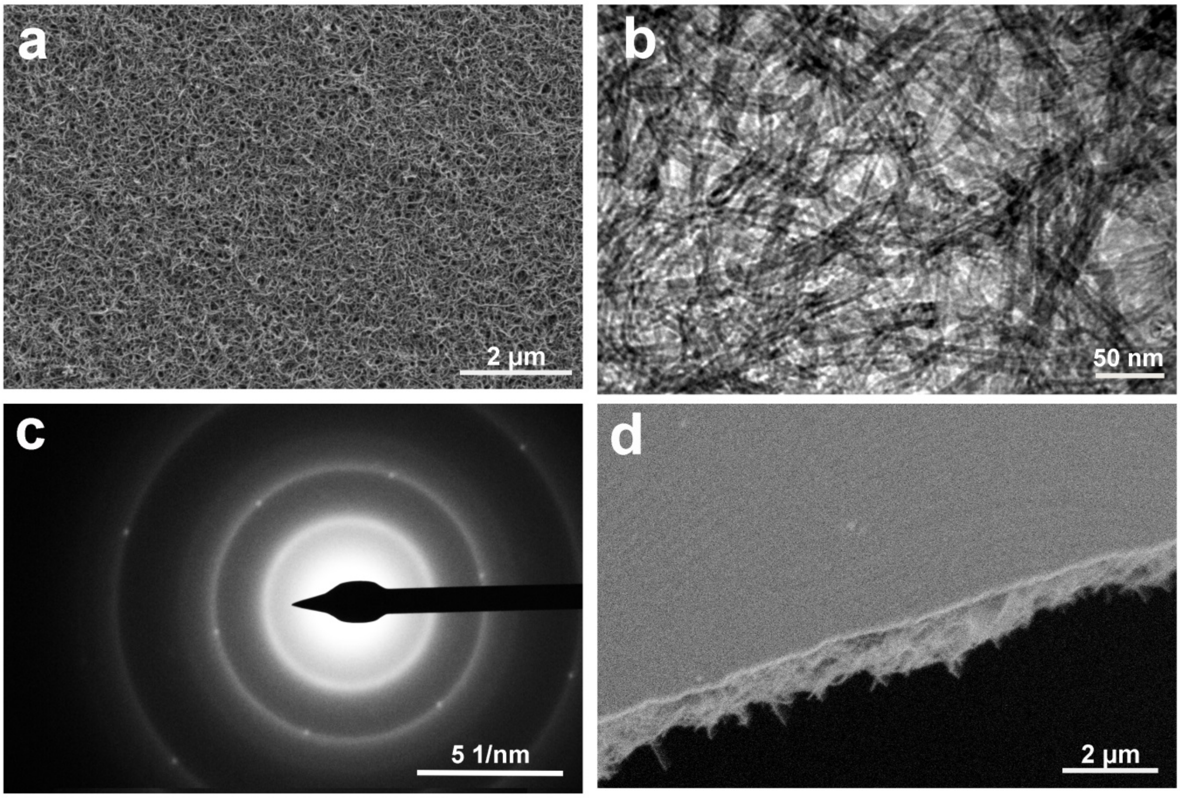

Figure 4.5. Morphology of the NSLG/NPC/MWNT film. (a) Top-view SEM image of the film revealing the uniform coating of the MWNT film on top of the NPC film. (b) TEM image revealing the mesh-like structure of the MWNT film. (c) A SAED pattern from the composite NSLG/NPC/MWNT film revealing the typical diffraction pattern of graphene. (d) Cross-sectional SEM image of the flipped NSLG/NPC/MWNT film with NSLG on top.

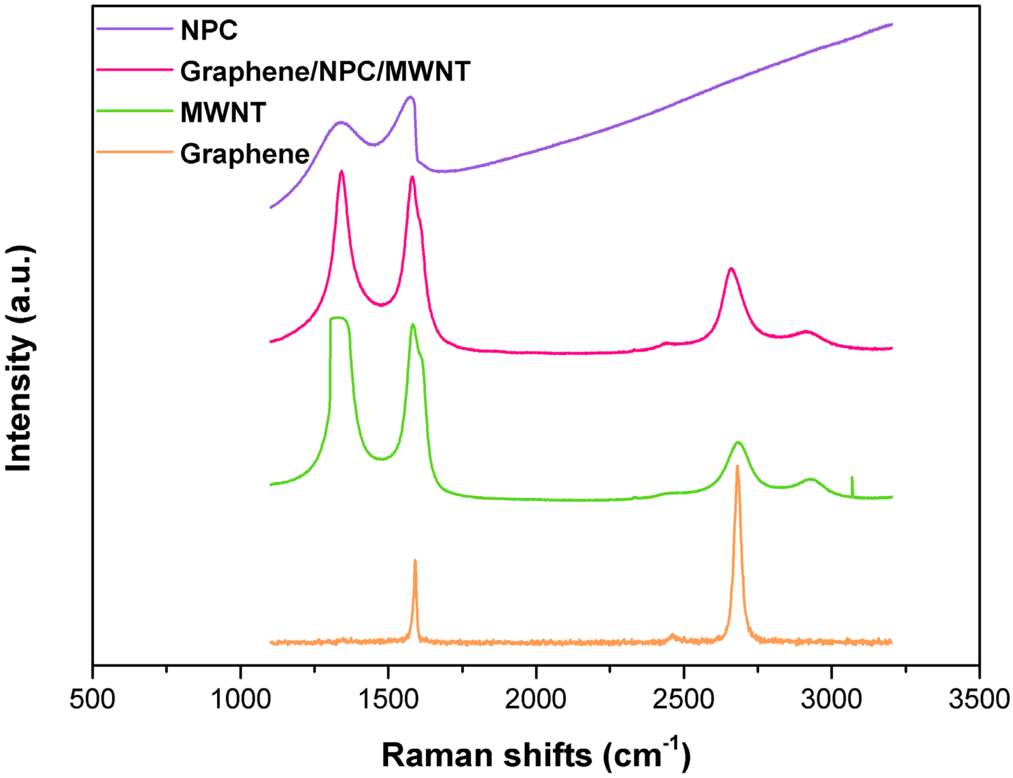

Figure 4.6. Raman spectra of CVD graphene, NPC, MWNT, and graphene/NPC/MWNT films transferred on a Si/SiO$_2$ wafer using a 532 nm excitation source.

4.3.2 Crack-free centimeter-scale membranes

The gas transport and separation properties of the fabricated membrane were investigated to understand the efficacy of NPC/MWNT reinforcing layer in suppressing difficult-to-observe nanoscale cracks in the centimeter-scale membranes. For this, we first investigated the membranes prepared using the as-synthesized SLG without any further incorporation of nanopores in the graphene lattice. SLG derived from low-pressure chemical vapor deposition (LPCVD) hosts a low density of intrinsic vacancy defects, which could be large enough to allow gas transport. For example, SLG synthesized by LPCVD at 1000 ºC using CH$_4$ as the carbon precursor could sieve H$_2$ from CH$_4$ with selectivity in the range of 5–13 and H$_2$ permeance of 5–80 × 10^{-9} mol m^{-2} s^{-1} Pa^{-1} at room temperature [234]. In this study, the as-synthesized SLG had I_D/I_G ratio of 0.08 ± 0.03, confirming that it hosted a low density of intrinsic defects (**Figure 4.7a** and **Figure 4.8**) [148,256].

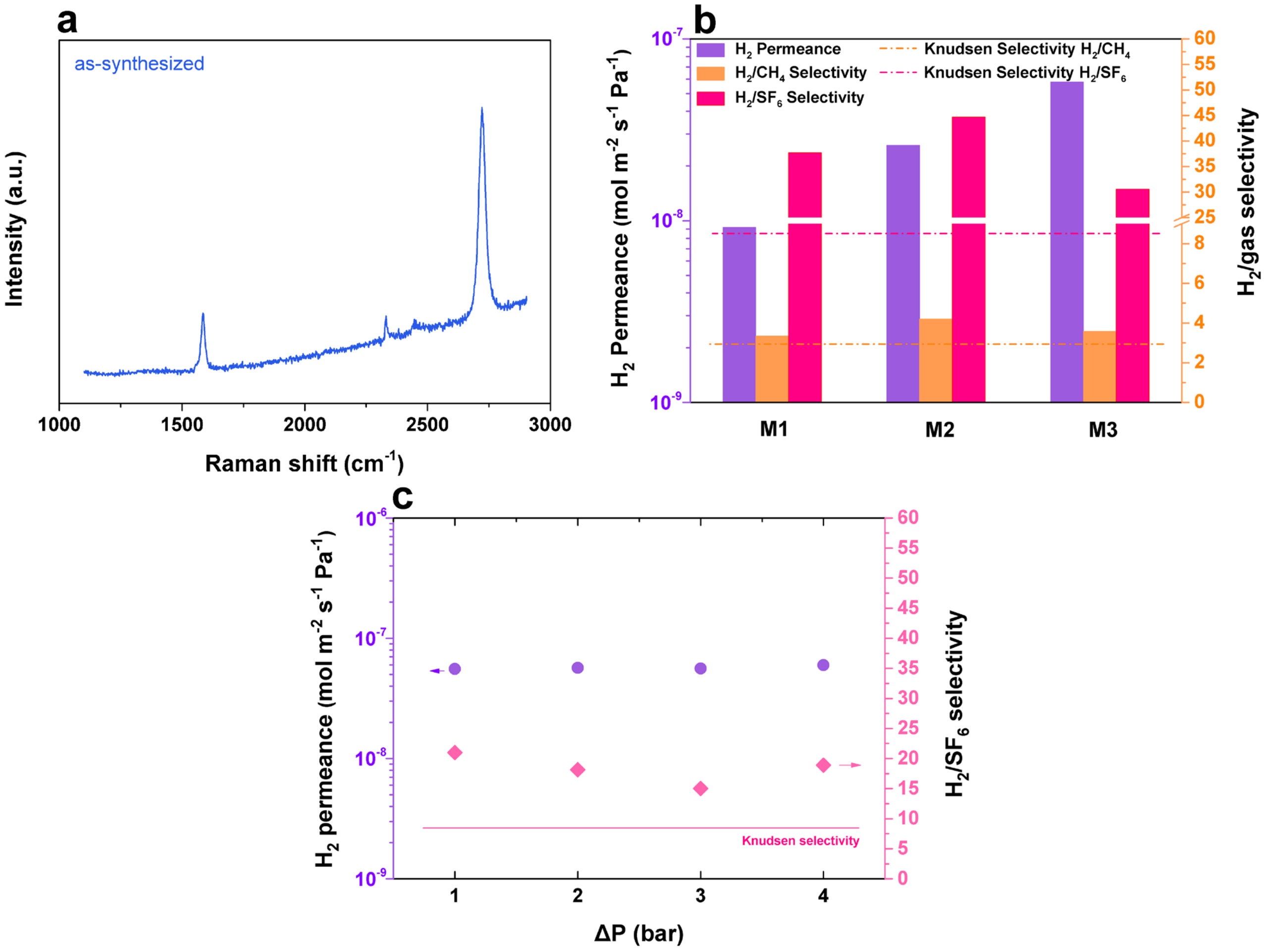

Figure 4.7. Characterization of the centimeter-scale reinforced membranes prepared using the as-synthesized SLG hosting intrinsic vacancy defects. (a) The Raman spectrum of SLG on Cu using a 457 nm excitation source. (b) H_2 permeance and ideal selectivities of H_2 with respect to CH_4 and SF_6 across three centimeter-scale graphene membranes (M1–M3) using a single-component feed. The horizontal dashed lines correspond to the expected Knudsen selectivity between the gas pairs when the effusive transport dominates the overall gas transport. (c) Pressure stability test of the graphene membrane (M7). H_2 permeance and H_2/SF_6 selectivity as a function of transmembrane pressure difference using a mixture feed at 25 °C.

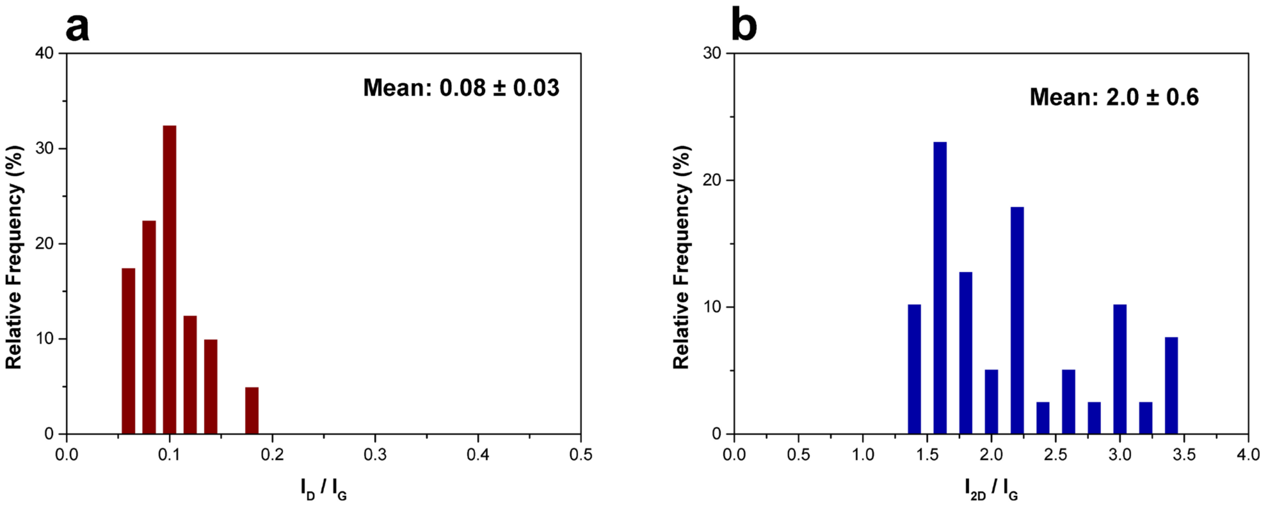

Figure 4.8. Raman analysis of graphene membrane. (a) Histogram of I_{2D}/I_G and (b) Histogram of I_D/I_G of as-synthesized graphene.

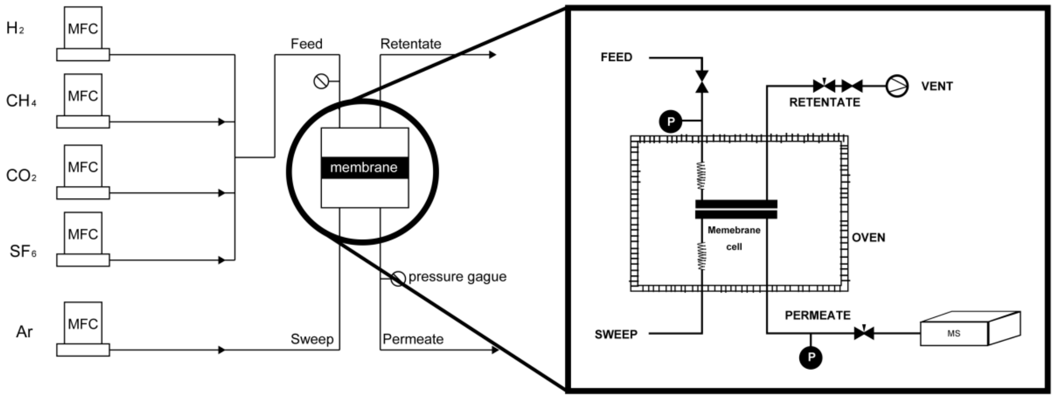
H₂
CH₄
CO₂
SF₆
Ar
MFC
MFC
MFC
MFC
MFC
Feed
Retentate
membrane
pressure gague
Sweep
Permeate
FEED
VENT
RETENTATE
P
Memebrane cell
OVEN
PERMEATE
SWEEP
MS
P

Figure 4.9. Schematic of the setup for gas permeation tests.

To confirm whether the large-area membranes in this study fabricated using the as-synthesized SLG were prepared in a crack-free manner, we sealed the membranes (**Figure 4.4d**) in a homemade module and subsequently loaded them in a gas permeation setup (**Figure 4.9**). The feed side was pressurized to 2–5 bar while the permeate side was swept with Ar at 1 bar. We observed gas separation performance that is characteristic of a crack-free SLG membranes hosting only intrinsic vacancy defects as gas transport apertures. Three separate membranes (M1, M2, M3, M stands for membrane) were tested which yielded H_2 permeance in the range of 9–58 × 10^{-9} mol m^{-2} s^{-1} Pa^{-1} at 25 °C, similar to that reported previously from mm^2-sized membranes [234]. The low gas permeance of such membranes supported on the ultrahigh-permeance macroporous metal mesh (ca. 10^{-3} mol m^{-2} s^{-1} Pa^{-1}) support confirmed that cracks were mitigated to a large extent. The variance in the gas permeance was attributed to the batch to batch variation in the density of intrinsic defects which is difficult to control [234]. The H_2/CH_4 ideal selectivity spanned from 3.3 to 4.2, higher than that expected from the Knudsen transport (~ 2.8). These selectivities are lower than those reported from millimeter-scale membranes [234], mainly attributing to the fact that the pore-size-distribution of intrinsic vacancy defects is difficult to control. The H_2/SF_6 selectivity was much higher, 30–44 (**Figure 4.7b** and Table 4.1), confirming that the membrane could efficiently sieve SF_6 from H_2 molecules, whose kinetic diameters are 0.55 nm and 0.29 nm, respectively. The high H_2/SF_6 selectivity established that cracks and tears were absent otherwise one would not observe the gas sieving behavior. The membranes were mechanically robust to sustain moderate transmembrane pressure of 4 bar. For example, another membrane, M7, deliberately tested for the pressure stability, could be pressurized to 5 bar on the feed side. We did not observe a change in the gas permeance as a function of pressure although a slight variation in the H_2/SF_6 selectivity (15–21) was observed (**Figure 4.7c**). Regardless, this proves that the reinforcement of SLG with the composite carbon film allows one to prepare membranes for gas separation applications where only moderate feed pressure is required, e.g., postcombustion carbon capture. The pressure loading capability of these membranes can be further increased, in principle, by choosing suitable underlying porous supports with smaller pore opening; e.g. 1–5 μm compared to 20 μm used in this study because the mechanical stress on a pressurized film scales as $D^{2/3}$ where D is the pore opening of the support [30].

4.3.3 Centimeter-scale NSLG membranes for H_2/CO_2 and H_2/CH_4 separation

The intrinsic defects in graphene are introduced during graphene crystallization, either as grain-boundary defects or vacancy defects resulting from the etching of graphene by the residual O_2 in the CVD reactor [257]. It is difficult to control the pore-size distribution (PSD) and the density of the intrinsic defects for a given separation. Luckily, one can incorporate nanopores into SLG lattice by post-synthetic etching technique, i.e., by the ozone-based controlled etching of the graphene lattice [50]. Herein, we demonstrate that the reinforcement used in this study allows one to successfully prepare centimeter-scale H_2/CO_2 and H_2/CH_4 selective membranes. We prepared NSLG by a controlled exposure of as-synthesized graphene to O_3 [50,234]. The etching of graphene resting on the Cu foil was confirmed by the Raman spectroscopy where I_D/I_G ratio of 0.92 could be observed (**Figure 4.10** and **Figure 4.11**) [258–260]. Three centimeter-scale membranes (M4, M5, M6) were prepared by reinforcing NSLG with the composite carbon film and suspending them on top of the metal mesh supports. All three membranes were stable up to 130 °C, the maximum working temperature for the epoxy-based sealant used in the membrane module (**Figure 4.12**), and yielded H_2 permeance in the range of 22–110 × 10^{-9} mol m^{-2} s^{-1} Pa^{-1} at 100°C. The H_2 permeance and gas selectivities were similar in the single-component and gas mixture measurements for both as-synthesized as well as etched graphene membranes (**Table 4.3–4.5**). Attractive H_2/CO_2 and H_2/CH_4 selectivities of 5–8 and 11.0–23.4, respectively, could be realized from these centimeter-scale membranes (**Figure 4.10b** and **Table 4.2**). We note that the observed H_2/CO_2 is lower than H_2/CH_4 selectivities. Since the difference between the kinetic diameters of H_2 and CO_2 is only 0.4 Å while that between H_2 and CH_4 is 0.9 Å, it is more challenging to sieve H_2 from CO_2 unless extremely precise pore-size-distribution is achieved. Despite that, H_2/CO_2 and H_2/CH_4 selectivities were much higher than the corresponding Knudsen selectivities of 4.7 and 2.8, respectively, confirming once again that centimeter-scale NSLG-based gas-sieving membranes could be prepared while avoiding cracks and tears. In comparison with other reported NSLG membranes, our approach exhibits promise for the further development of the gas separation membranes based on nanoporous single-layer graphene-based (**Table 4.6**).

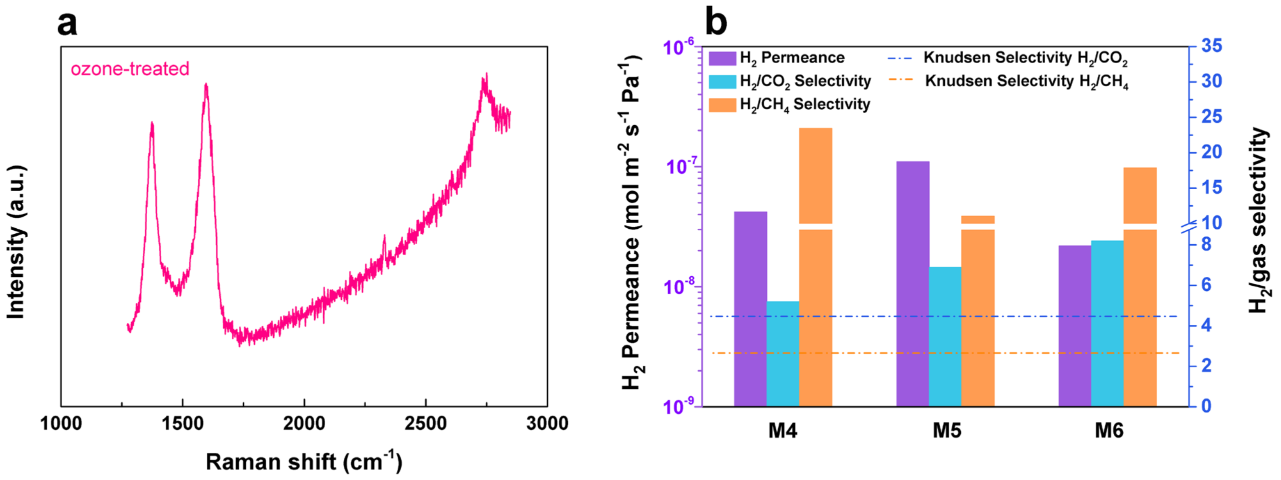

Figure 4.10. Characterization of the centimeter-scale reinforced graphene membranes prepared using the ozone-etched graphene. (a) The Raman spectrum of graphene on Cu etched by ozone using a 457 nm excitation source. (b) H_2 permeance and ideal selectivities of H_2 with respect to CH_4 and CO_2 across three graphene membranes (M4–M6) using a single-component feed at 100°C. The horizontal dashed lines correspond to the expected Knudsen selectivity between the gas pairs when the effusive transport dominates the overall gas transport.

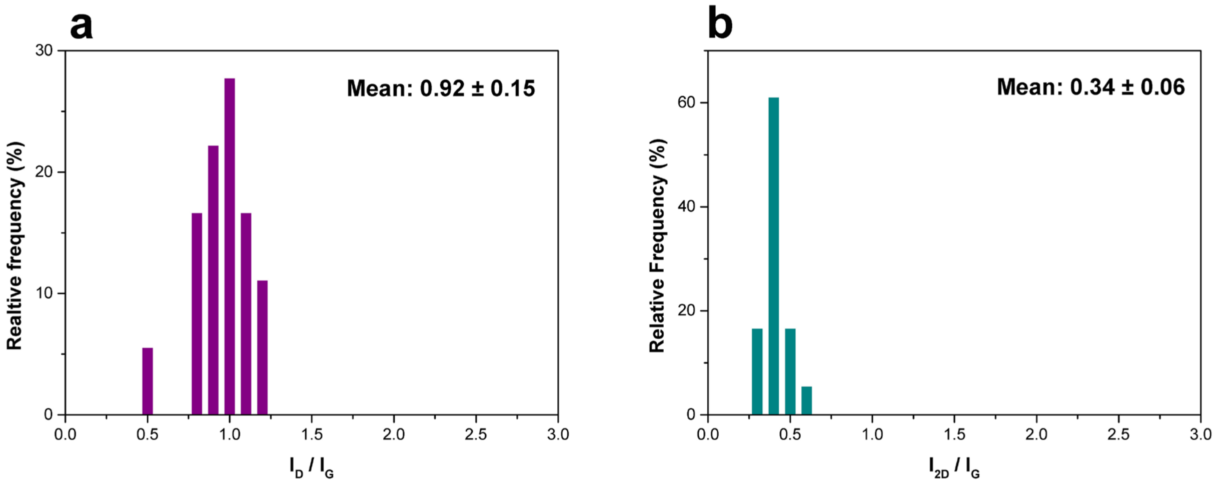

Figure 4.11. Raman analysis of ozone-etched graphene membrane. (a) Histogram of I_{2D}/I_G and (b) histogram of I_D/I_G of ozone-etched graphene.

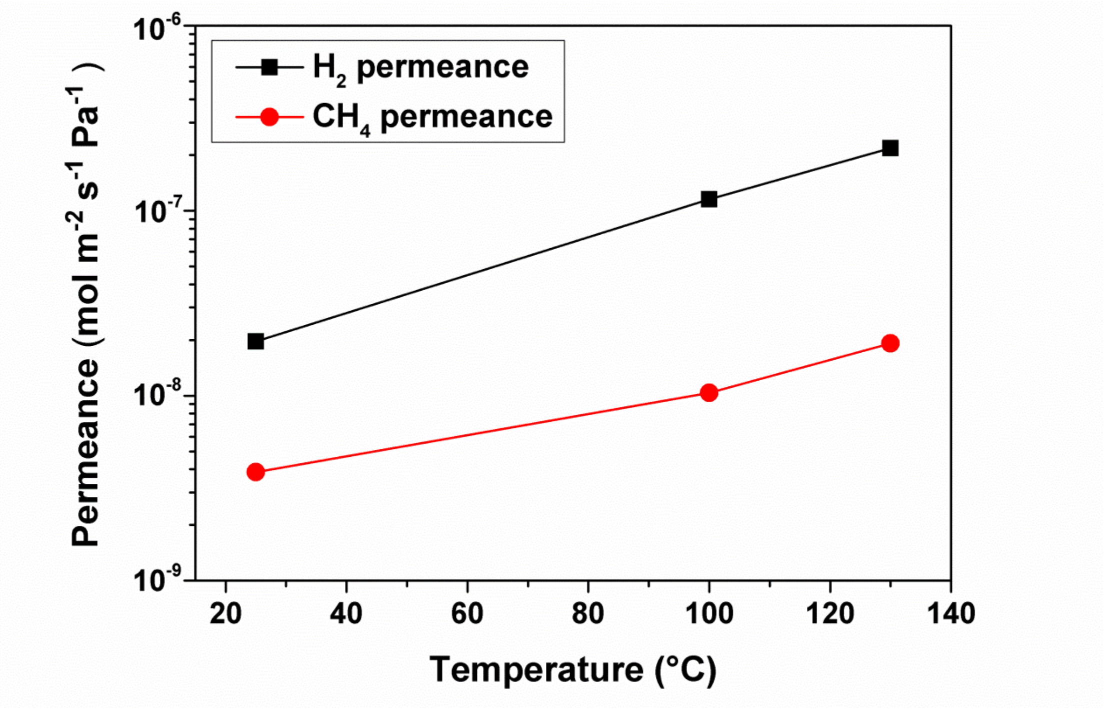

Figure 4.12. H_2 and CH_4 permeance of M5 as a function of temperature. Each point is taken after gases are stabilized at a certain temperature for at least 30 minutes.

4.3.4 Analysis of the concentration of non-selective pores

We analyzed the gas selectivity data to understand the relative concentration of non-selective pores in the graphene membranes reported in this study. The transport pathway of gas molecules across a two-dimensional nanopore can be classified according to the relative size of the nanopore with respect to the gas molecules. For nanopores that are slightly smaller or commensurate to the size of gas molecules, the molecules require to overcome an energy barrier, and therefore, the rate-limiting step in the overall transport is the thermal activation of gas molecules for the pore translocation. This transport regime is referred to as activated transport (**Figure 4.13b**). For relatively bigger nanopores, the energy barrier for pore translocation is negligible, and the gas molecules can translocate the nanopores directly from the gas phase. Therefore, the permeation rates through these pores are much higher, and gas molecules can directly cross the nanopores in the gas phase. This transport regime is referred to as effusive transport (**Figure 4.13a**). The transport rates across the graphene pores can be described by the permeation coefficient, N, which is essentially permeance per pore with the units of mol s^{-1} Pa^{-1}.

Let’s consider the current case of the transport of H_2 and CH_4 through the graphene nanopores. In our model, we assumed a bimodal pore-size-distribution (PSD) consisting of small H_2-selective pores operating in the activated transport regime and large pores that are not selective and operate in the effusive transport regime. For simplicity, we assigned the large pore to be 2 nm in size. Choosing a higher (e.g., 3 nm) or lower size (e.g., 1.5 nm) for the effusive pore in this analysis will simply increase/decrease the permeation coefficient and accordingly decrease/increase the density of effusive pores. However, it would not change the relative concentration of non-selective pores from one membrane to another. In this case, the overall gas permeance can be obtained as follows [50]:

$$Permeance = C_a N_a + C_e N_e \qquad \textbf{(Equation 4.3)}$$

where C_a and C_e correspond to the number of pores per unit area operating in the activated and the effusive transport regimes, respectively, and N_a and N_e are the corresponding permeation coefficients, respectively. For the effusive transport, the permeation coefficient can be obtained from the kinetic theory of gases [261]:

$$N_e = \frac{A_p}{\sqrt{2\pi m k_B T}} \qquad \textbf{(Equation 4.4)}$$

where A_p is the pore area, m is the mass of the gas molecule, k_B is the Boltzmann constant, and T is the temperature. Based on this, the computed permeation coefficients of H_2 and CH_4 from a 2-nm-sized pore are 5.6×10^{-19} and 2.0×10^{-19} mol s^{-1} Pa^{-1}, respectively. The ratio of the coefficient is 2.8, which corresponds to the inverse of the square root of the ratio of corresponding molecular weights, otherwise known as the Knudsen selectivity. For the activated transport, the permeation coefficient N_a could be estimated from the translocation probability of gas molecules. This, in turn, depends on the distribution of molecular kinetic energy (Maxwell-Boltzmann distribution), where the probability of translocation is determined by the kinetic energy exceeding the energy barrier for translocation [77]. The permeation coefficient can be expressed as follows:

$$N_a = \frac{A_{eff}}{\sqrt{2\pi m k_B T}} \qquad \textbf{(Equation 4.5)}$$

$$A_{eff} = \frac{1}{2} erfc(\sqrt{\frac{E_a}{k_B T}}) A_p \qquad \textbf{(Equation 4.6)}$$

where A_{eff} is the effective pore area, and E_a is the activation energy of the gas molecules translocating the nanopore. We used permeation coefficients from literature where $N_{a_{H_2}}$ and $N_{a_{CH_4}}$ are reported to be ca. 10^{-22} and 10^{-26} mol s^{-1} Pa^{-1}, respectively, from a H_2-sieving nanopore [77].

The ideal selectivity, α, is simply given by

$$\alpha = \frac{Permeance_{H_2}}{Permeance_{CH_4}} \qquad \textbf{(Equation 4.7)}$$

Based on this, we could calculate the ratio C_e/C_a which is given by

$$\frac{C_e}{C_a} = \frac{N_{a,H_2} - \alpha N_{a,CH_4}}{N_{e,H_2}(\alpha / 2.8 - 1)} \qquad \textbf{(Equation 4.8)}$$

The calculated concentration of nanopores operating in the effusive transport regime as a function of H_2/CH_4 selectivity is plotted in **Figure 4.13c**. The concentration of effusive nanopores appears to be inversely proportional to the gas selectivity for moderate selectivities (<100) mainly because of the large difference in $N_{a_{H_2}}$ and $N_{a_{CH_4}}$ which effectively makes **equation 4.9** as follows:

$$\frac{C_e}{C_a} = (\frac{N_{a,H_2}}{N_{e,H_2}}) \frac{1}{(\alpha / 2.8 - 1)} \qquad \textbf{(Equation 4.9)}$$

Overall, the analysis predicted that all membranes in this study, with the centimeter-scale area, comprised of only a small density of effusive pores (**Figure 4.13c**). The populations of effusive pores for membranes M1, M2, and M3 were 925, 500, and 356 ppm, respectively. The populations of effusive pores for M4, M5, M6, prepared by ozone-etched graphene were much lower (24, 60, and 32 ppm, respectively), attributing to the controlled etching of graphene by ozone [50]. This is because the introduction of new gas-sieving nanopores by the post-synthetic treatment dilutes the concentration of effusive pores with respect to the entire pore population. Nonetheless, a small concentration of effusive pores in this study validates the absence of cracks and tears in these membranes. Furthermore, the gas sieving performance from scaled-up membranes can be enhanced by diminishing the direct gas transport across graphene nanopores, e.g., using a nanoporous polymer-based masking strategy [45].

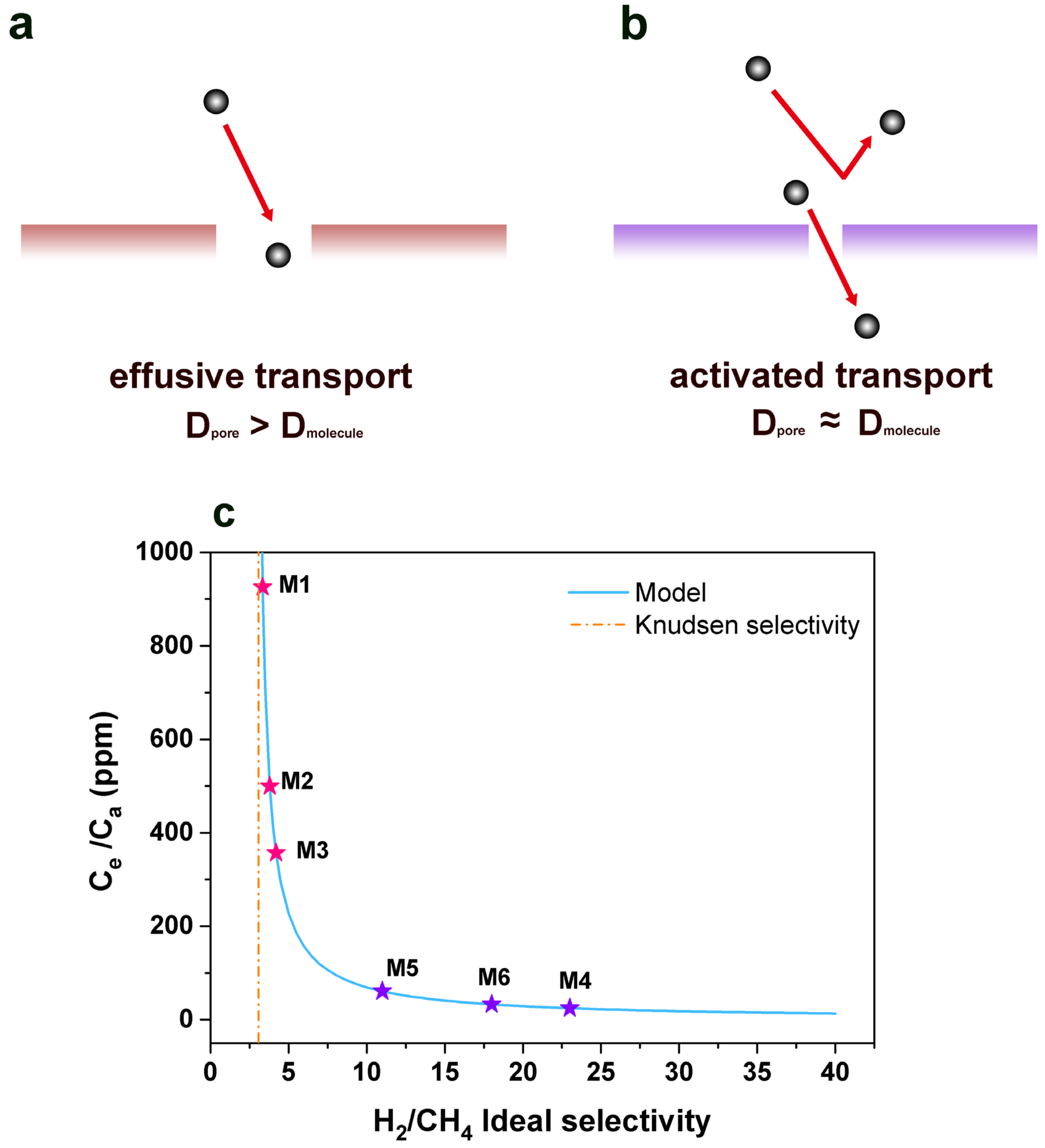

Figure 4.13. Modeling gas transport behavior in a graphene nanopore. (a) Illustration of the effusive transport taking place in a graphene nanopore, where the pore size is larger than the gas molecule, and of (b) the activated transport, where the pore size is slightly smaller or approximately equal to the gas molecules. (c) A model that predicts the concentration of the effusive pores as a function of the measured H_2/CH_4 selectivity. The data from membranes M1–M6 is overlaid on top of the model. The vertical dashed line corresponds to the expected Knudsen selectivity of H_2/CH_4.

4.3.5 Use of NPC-free MWNT layer to transfer graphene

Taking advantage of the potential π-π interactions between MWNT and graphene [262,263], we attempted to directly deposit the MWNT film on top of graphene for the fabrication of the reinforced NSLG membrane, avoiding the intermediate NPC layer. To understand the bonding between MWNT and NSLG, MWNT supported NSLG film was transferred to a TEM grid. Interestingly, we could also observe the characteristic SAED pattern of SLG in this case, indicating that the transfer of NSLG with MWNT was somewhat successful (**Figure 4.14**). However, the membranes fabricated from these films did not demonstrate gas sieving and gas selectivities were lower than the corresponding Knudsen selectivities (**Table 4.7**). The H_2 permeance of MWNT-supported NSLG hosting only intrinsic defects was extremely high, 2.0×10^{-5} mol m^2 s^{-1} Pa^{-1}, close to that from the bare MWNT mesh (4.1×10^{-4} mol m^2 s^{-1} Pa^{-1}). This indicated that difficult-to-observe nanoscale cracks were indeed present in the fabricated membranes when the intermediate NPC film was not used to transfer NSLG. Using SWNT mesh, the suspended NSLG is divided into 200–300-nm-sized domains with nanotube mesh as the boundary of these domains. However, the precise control of these domains is not possible by the current method, and we speculate that occasional micron-size domains may be present in the MWNT film. Micron-size suspended NSLG is highly susceptible to mechanical failure in the pressurized environment of membranes. As discussed in the previous section, the permeation coefficient in the effusive transport regime is much higher than that in the activated transport regime; therefore, even a ppm concentration of nanoscale cracks is sufficient to deteriorate the selectivity. This underlines the important role of NPC film in preventing the cracks in NSLG membranes where the suspended domains are limited to 20–30 nm.

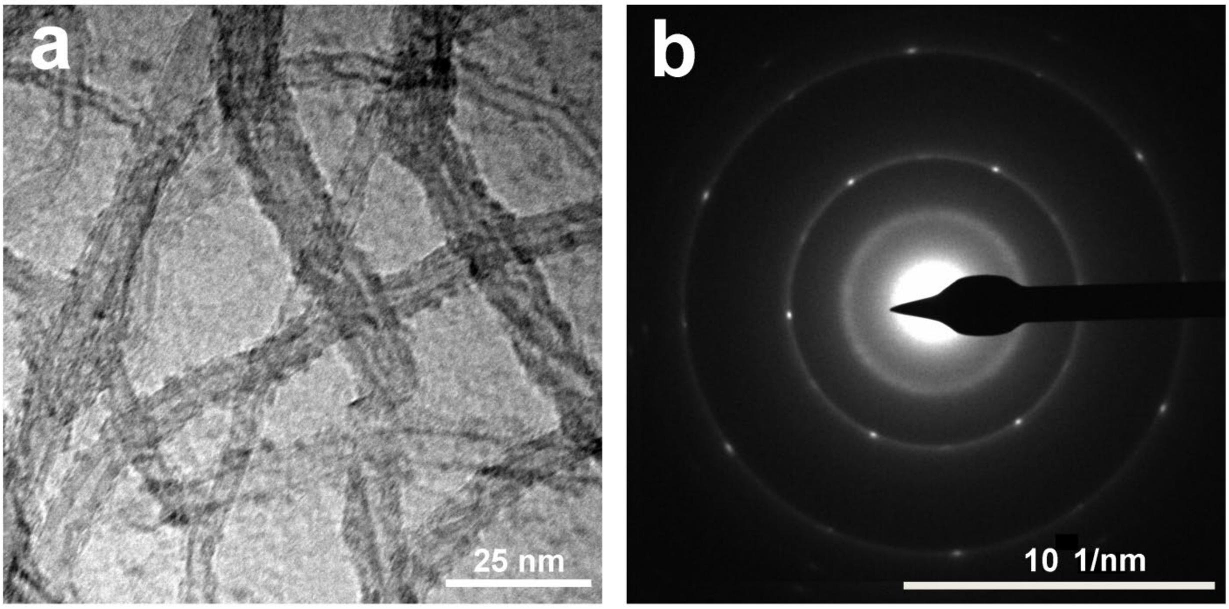

Figure 4.14. Characterization of NSLG/ MWNT film. (a) TEM image of the suspended NSLG film using only the MWNT film as the mechanical reinforcement (avoiding the NPC layer). (b) The SAED pattern from the film in (a).

4.4. Conclusion

We report a facile and scalable fabrication route for crack-free NSLG membranes on a low-cost macroporous support with an attractive gas-sieving performance from centimeter-scale membranes. We achieved this by mechanically reinforcing graphene with a composite carbon film using a facile solution-processing method. The top layer of the composite film (MWNT layer) hosts 200–300-nm-sized pores while the bottom layer (NPC film), that contacts NSLG, has a pore size of 20–30 nm. We show that the composite film is crucial for the successful fabrication of the membrane on a low-cost macroporous support at the centimeter-scale, while the use of standalone MWNT film does not lead to the realization of gas separation which we attribute to the presence of nanoscale cracks in such films. The H_2/CH_4 and H_2/CO_2 selectivities, when analyzed by a gas transport model, indicated that the population of nanopores operating in the nonselective effusive regime was restricted to only a few ppm. Overall, the method reported here could pave the way for the further development and eventual implementation of the gas-selective graphene membranes for gas separation.

4.5. Appendix I

Table 4.1. Gas permeation data of M2 at 25 and 100 °C, single-component measurement.

M2 (as-synthesized)	H_2 permeance (mol s^{-1} m^{-2} Pa^{-1})	CH_4 permeance (mol s^{-1} m^{-2} Pa^{-1})	H_2/CH_4
25 °C	4.2×10^{-8}	9.4×10^{-9}	4.47
100 °C	4.2×10^{-8}	1.0×10^{-8}	4.18

Table 4.2. Gas permeation data of M5 at 25 and 100 °C, single-component measurement.

M5 (ozone-etched)	**H_2 permeance (mol s^{-1} m^{-2} Pa^{-1})**	**CH_4 permeance (mol s^{-1} m^{-2} Pa^{-1})**	**H_2/CH_4**
25 °C	1.9×10^{-8}	3.9×10^{-9}	5.08
100 °C	1.1×10^{-7}	1.0×10^{-8}	11.1

Table 4.3. Comparison of the single-component versus mixture permeation data from M2.

M2 (as-synthesized)	**H_2 permeance (mol s^{-1} m^{-2} Pa^{-1})**	**CH_4 permeance (mol s^{-1} m^{-2} Pa^{-1})**	**H_2/CH_4**
Single-component	4.2×10^{-8}	9.4×10^{-9}	4.47
mixture	2.6×10^{-8}	6.1×10^{-9}	4.18

Table 4.4. Comparison of the single-component versus mixture permeation data from M5.

M5 (ozone-etched)	**H_2 permeance (mol s^{-1} m^{-2} Pa^{-1})**	**CH_4 permeance (mol s^{-1} m^{-2} Pa^{-1})**	**H_2/CH_4**
Single-component	1.1×10^{-7}	1.0×10^{-8}	11.1
mixture	9.9×10^{-8}	7.9×10^{-9}	12.5

Table 4.5. Comparison of the single-component versus mixture permeation data from M5.

M5 (ozone-etched)	**H_2 permeance (mol s^{-1} m^{-2} Pa^{-1})**	**CO_2 permeance (mol s^{-1} m^{-2} Pa^{-1})**	**H_2/CO_2**
Single-component	1.1×10^{-7}	1.6×10^{-8}	6.9
mixture	9.2×10^{-8}	1.5×10^{-8}	6.4

Table 4.6. Comparison of gas separation performance between our work and other CVD graphene-based membranes.

Membrane description	Area (cm^2)	Pore etching method	Gas permeance [mol m^{-2} s^{-1} Pa^{-1}]	Gas separation factor
Single-layer graphene [233]	2 $\times 10^{-7}$	Intrinsic defect	0.2–2.0 × 10^{-4} (He, 100 °C)	1.98 – 2.4 (He/CH_4)
Bilayer graphene [49]	6.2 $\times 10^{-6}$	Focus ion beam	1.5 (H_2, 25°C)	~ 2.7 (H_2/CH_4)
Bilayer graphene [64]	8 $\times 10^{-6}$	Intrinsic defect + high temperature O_2 etching	0.0005 – 7.5 × 10^{-4} (H_2, 25 °C)	3.8 – 9.3 (H_2/CH_4)
Single-layer graphene [234]	10^{-2}	Intrinsic defect	0.2–2.0 × 10^{-7} (H_2, 100 °C)	4.8 – 13.0 (H_2/CH_4)
Single-layer graphene [50]	10^{-2}	O_2 plasma	2.0–6.0 × 10^{-7} (H_2, 100 °C)	15.6 – 25.1 (H_2/CH_4)
Single-layer/bilayer graphene [56]	1	Nano patterning	3.64 × 10^{-4} (H_2, 25°C)	~ 2.86 (H_2/CH_4)
Single-layer graphene (this work)	1	Intrinsic defect + Ozone	0.05–1.1 × 10^{-7} (H_2, 100 °C)	3.3 – 23.4 (H_2/CH_4)

Table 4.7. Permeance and selectivity of MWNT film and graphene membrane prepared by using MWNT reinforcement (without NPC film) at a feed pressure 1.5 bar at 25 °C.

Film	H_2 Permeance [mol m^{2} s^{-1} Pa^{-1}]	H_2/CO_2 Selectivity	H_2/CH_4 Selectivity
MWNT film	4.1×10^{-4}	4.0	2.5
graphene/MWNT	2.0×10^{-5}	4.0	2.5

Chapter 5 Summary and Perspectives

5.1 Summary

In this thesis, I have discussed the background, potential applications, current understanding, and challenges of nanoscale hydrodynamics, molecular kinetics, and molecular sieving through graphene nanopores. Since detailed studies of the mass transport through angstrom-scale nanopores remain limited, this thesis aims at providing insights and new approaches for further exploration of graphene nanopores and related applications. Achievements covered in this thesis are summarized as follows:

1. The first experimental study of water evaporation from angstrom-scale graphene nanopores. The evaporation flux from nanopores showed an enhancement compared to the bare liquid–vapor interface. In addition, the evaporation flux decreased with increasing pore sizes. Molecular dynamics revealed that water–water hydrogen bonds at smaller pores are short-lived due to the water–pore interaction, which renders enhanced evaporation flux from graphene nanopores. This work helps to enrich the understanding of water evaporation at the nanoscale and pave the way to energy-efficient evaporation-based technologies.
2. The study of ion transport through sub-nanometer graphene nanopores showed high monovalent/divalent cation selectivity exceeding all other graphene nanopores reported in the literature. The high ion selectivity was achieved by tuning the pore size with a decoupled pore nucleation/expansion approach. Thus, we achieved a molecular cutoff allowing the permeation of small monovalent cations but rejecting larger divalent cations, resulting in an unprecedently high K^+/Mg^{2+} selectivity of up to 350 and Li^+/Mg^{2+} selectivity of up to 260. This work suggests a size-exclusion mechanism associated with ion-dependent dehydration for selective ion transport. This work demonstrates the potential of graphene nanopores for high-precision ion–ion separation applications.
3. The demonstration of gas-sieving centimeter-scale nanoporous graphene. The nanoporous graphene was reinforced by a two-layer carbon-based composite film. Due to the high affinity between the reinforcing layer and graphene, the resulting large-area nanoporous graphene was crack-free, showing H_2/CH_4 and H_2/CO_2 selectivities of 11–23 and 5–8, respectively. This work facilitates the implementation of promising commercial applications of graphene nanopores.

5.2 Perspectives

Graphene nanopores offer a versatile platform for various studies and applications, but there are still many properties to be explored. For instance, recent work by Kavokine et al. reported “quantum friction” in graphene and graphite that govern the hydrodynamic flows under nanoconfinement [1]. Therefore, developing a corresponding theory in the field is critical to obtaining a comprehensive picture of mass transport in angstrom-scale nanopores. Meanwhile, applications can benefit from the attractive transport efficiencies and selectivities observed in graphene nanopores. Below, I summarize some thoughts about the future directions.

Heat management using nanoporous graphene

Nowadays, chips and processors are made smaller and smaller while accommodating more and more components, and thus thermal management is crucial for a device to perform at its full capacity. Evaporation is an effective cooling method widely employed in nature and industries. Previous studies showed that microfabricated ultrathin nanoporous membrane evaporators [264,265] demonstrated potential in high flux thermal management ($q > 500$ W/cm^2) for high-performance electronics. The performance of the membrane evaporator can be further boosted by (1) minimizing the thickness of the membrane and (2) taking advantage of the new evaporation mechanism that shows enhanced evaporation compared to its counterpart in the bulk state. As shown in **Chapter 2,** single-layer graphene hosting angstrom-scale pores fulfills these requirements. Thus it is a promising material in the application of membrane evaporator as one of the thermal management solutions. However, the porosity of our current graphene membrane is still low (< 1.3%). A crucial step to realizing graphene’s potential in realistic applications is engineering the pore density, which I further discuss in the following sections.

Improvement in ion selectivity and beyond

The ultrahigh ion selectivity in biological channels results from not only the sub-nanometer-sized channel but also the presence of a selectivity filter, which offers complex electrostatic, dipole, and van der Waals interactions between the ions and the pore wall, leading to selective ion permeation. While we showed that graphene itself could give ion selectivity using only pore size/geometry, the separation performance can presumably be further enhanced by incorporating other selective mechanisms. For instance, Tan *et al.* [17] have demonstrated the use of a chemically modified polymer of intrinsic microporosity (PIM) for selective ion separation and flow-battery energy storage. Compared to graphene itself, PIM could provide rich surface charges across the heterogeneous pore channels that may further modulate ion transport. It has been shown that PIM has good adhesion with graphene [45], and the combination of graphene nanopores with PIMs may result in a synergetic effect for precise ion sieving.

Improvement in ion permeance: porosity engineering

Despite promising transport properties, graphene's typical porosity is less than 1%, and thus, the ion permeance through graphene nanopores is still relatively low compared to other highly porous materials. Enhanced porosity can make a step forward in the commercial applications of graphene. As shown in **Chapter 3**, the porosity is determined by the first O_3 etching step. O_3 indeed serves as a good tool to create small vacancy defects in graphene lattice, and the etching kinetic is influenced by temperature, exposure time, and concentration. Future studies could focus on revealing the scientific understanding of O_3 etching at slightly higher temperatures (> 43 °C) to explore a way to high defect density.

Voltage-gated ion transport through graphene nanopores

It has been reported that Coulomb blockade can be observed in a single sub-nanometer MoS_2 pore [22] as well as a graphene oxide laminate with angstrom-scale interlayer spacing [181]. Voltage-gated Coulomb blockade is ideal for the design of ion transistors. Wyss *et al.* [202] have demonstrated this concept using graphene hosting 20 nm pores; however, they did not observe Coulomb blockade due to the large pore size. Therefore, our angstrom-scale graphene nanopores may be an interesting platform for observing Coulomb blockade and for building an ion transistor

Studying ion transport using atomic simulation

Given such a small scale to enable effective ion–ion separation in our graphene nanopores, molecular dynamics (MD) may be a useful alternative to investigating molecular-level details of ions and fluids [79,81,84,92,96]. In particular, research on the metal cation selectivity using atomic simulation is limited, and the studies of the transport property of divalent cations such as Mg^{2+} and Ca^{2+} across nanopores are few. Insights into the atomic-scale details of ion transport under nanoconfinement are urgently needed to enrich our understanding, which will enable us to develop synthetic analogues of biological channels for highly efficient separation applications

References

[1] N. Kavokine, M.-L. Bocquet, L. Bocquet, Fluctuation-induced quantum friction in nanoscale water flows, *Nature* **602** (2022) 84–90.

[2] A. Siria, et al., Giant osmotic energy conversion measured in a single transmembrane boron nitride nanotube, *Nature* **494** (2013) 455–458.

[3] C. Duan, A. Majumdar, Anomalous ion transport in 2-nm hydrophilic nanochannels, *Nat. Nanotechnol.* **5** (2010) 848–852.

[4] R. Karnik, C. Duan, K. Castelino, H. Daiguji, A. Majumdar, Rectification of Ionic Current in a Nanofluidic Diode, *Nano Lett.* **7** (2007) 547–551.

[5] C. Wang, et al., Wafer-scale integration of sacrificial nanofluidic chips for detecting and manipulating single DNA molecules, *Nat. Commun.* **8** (2017) 14243.

[6] B. Radha, et al., Molecular transport through capillaries made with atomic-scale precision, *Nature* **538** (2016) 222–225.

[7] T. Jain, et al., Heterogeneous sub-continuum ionic transport in statistically isolated graphene nanopores, *Nat. Nanotechnol.* **10** (2015) 1053–1057.

[8] S. Faucher, et al., Critical Knowledge Gaps in Mass Transport through Single-Digit Nanopores: A Review and Perspective, *J. Phys. Chem. C* **123** (2019) 21309–21326.

[9] R. H. Tunuguntla, et al., Enhanced water permeability and tunable ion selectivity in subnanometer carbon nanotube porins, *Science* **357** (2017) 792–796.

[10] L. C. Young, C. Wonjoon, H. Jae-Hee, S. M. S., Coherence Resonance in a Single-Walled Carbon Nanotube Ion Channel, *Science* **329** (2010) 1320–1324.

[11] K. V. Agrawal, S. Shimizu, L. W. Drahushuk, D. Kilcoyne, M. S. Strano, Observation of extreme phase transition temperatures of water confined inside isolated carbon nanotubes, *Nat. Nanotechnol.* **12** (2017) 267–273.

[12] R. Nair, A. Wu, N. Jayaram, V. Grigorieva, A. K. Geim, Unimpeded Permeation of Water Through Helium-Leak–Tight Graphene-Based Membranes, *Science* **335** (2012) 442–444.

[13] J. Abraham, et al., Tunable sieving of ions using graphene oxide membranes, *Nat. Nanotechnol.* **12** (2017) 546–550.

[14] K.-G. Zhou, et al., Electrically controlled water permeation through graphene oxide membranes, *Nature* **559** (2018) 236–240.

[15] Y. Li, M. A. Alibakhshi, Y. Zhao, C. Duan, Exploring Ultimate Water Capillary Evaporation in Nanoscale Conduits, *Nano Lett.* **17** (2017) 4813–4819.

[16] Y. Li, et al., Ultrafast Diameter-Dependent Water Evaporation from Nanopores, *ACS Nano* **13** (2019) 3363–3372.

[17] R. Tan, et al., Hydrophilic microporous membranes for selective ion separation and flow-battery

energy storage, *Nat. Mater.* **19** (2020) 195–202.

[18] J. Lu, et al., Efficient metal ion sieving in rectifying subnanochannels enabled by metal–organic frameworks, *Nat. Mater.* **19** (2020) 767–774.

[19] B. Coasne, A. Galarneau, R. J. M. Pellenq, F. Di Renzo, Adsorption, intrusion and freezing in porous silica: the view from the nanoscale, *Chem. Soc. Rev.* **42** (2013) 4141–4171.

[20] M. Zhang, et al., Controllable ion transport by surface-charged graphene oxide membrane, *Nat. Commun.* **10** (2019) 1253.

[21] Q. Yang, et al., Ultrathin graphene-based membrane with precise molecular sieving and ultrafast solvent permeation, *Nat. Mater.* **16** (2017) 1198–1202.

[22] J. Feng, et al., Observation of ionic Coulomb blockade in nanopores, *Nat. Mater.* **15** (2016) 850–855.

[23] J. Feng, et al., Single-layer MoS2 nanopores as nanopower generators, *Nature* **536** (2016) 197–200.

[24] A. Esfandiar, et al., Size effect in ion transport through angstrom-scale slits, *Science* **358** (2017) 511–513.

[25] C. Duan, W. Wang, Q. Xie, Review article: Fabrication of nanofluidic devices, *Biomicrofluidics* **7** (2013) 26501.

[26] S. Garaj, et al., Graphene as a subnanometre trans-electrode membrane, *Nature* **467** (2010) 190–193.

[27] C. J. Russo, A. J. Golovchenko, Atom-by-atom nucleation and growth of graphene nanopores, *Proc. Natl. Acad. Sci.* **109** (2012) 5953–5957.

[28] S. C. O'Hern, et al., Selective Ionic Transport through Tunable Subnanometer Pores in Single-Layer Graphene Membranes, *Nano Lett.* **14** (2014) 1234–1241.

[29] K. S. Novoselov, et al., Two-dimensional gas of massless Dirac fermions in graphene, *Nature* **438** (2005) 197–200.

[30] D. Cohen-Tanugi, J. C. Grossman, Mechanical Strength of Nanoporous Graphene as a Desalination Membrane, *Nano Lett.* **14** (2014) 6171–6178.

[31] A. E. Galashev, O. R. Rakhmanova, Mechanical and thermal stability of graphene and graphene-based materials, *Physics-Uspekhi.* **57** (2014) 970–989.

[32] P. Ravi, Graphene Spreads the Heat, *Science* **328** (2010) 185–186.

[33] C. Lee, X. Wei, J. W. Kysar, J. Hone, Measurement of the Elastic Properties and Intrinsic Strength of Monolayer Graphene, *Science* **321** (2008) 385–388.

[34] K. Kim, et al., High-temperature stability of suspended single-layer graphene, *Phys. Status Solidi – Rapid Res. Lett.* **4** (2010) 302–304.

[35] J.-H. Chen, C. Jang, S. Xiao, M. Ishigami, M. S. Fuhrer, Intrinsic and extrinsic performance limits of graphene devices on SiO2, *Nat. Nanotechnol.* **3** (2008) 206–209.

[36] K. Parvez, et al., Exfoliation of Graphite into Graphene in Aqueous Solutions of Inorganic Salts, *J. Am. Chem. Soc.* **136** (2014) 6083–6091.

[37] C.-J. Shih, et al., Bi- and trilayer graphene solutions, *Nat. Nanotechnol.* **6** (2011) 439–445.

[38] T. C. Achee, et al., High-yield scalable graphene nanosheet production from compressed graphite using electrochemical exfoliation, *Sci. Rep.* **8** (2018) 14525.

[39] L. Xuesong, et al., Large-Area Synthesis of High-Quality and Uniform Graphene Films on Copper Foils, *Science* **324** (2009) 1312–1314.

[40] B. Deng, Z. Liu, H. Peng, Toward Mass Production of CVD Graphene Films, *Adv. Mater.* **31** (2019) 1800996.

[41] P. R. Kidambi, et al., A Scalable Route to Nanoporous Large-Area Atomically Thin Graphene Membranes by Roll-to-Roll Chemical Vapor Deposition and Polymer Support Casting, *ACS Appl. Mater. Interfaces* **10** (2018) 10369–10378.

[42] S. Bae, et al., Roll-to-roll production of 30-inch graphene films for transparent electrodes, *Nat. Nanotechnol.* **5** (2010) 574–578.

[43] B. N. Chandrashekar, et al., Roll-to-Roll Green Transfer of CVD Graphene onto Plastic for a Transparent and Flexible Triboelectric Nanogenerator, *Adv. Mater.* **27** (2015) 5210–5216.

[44] S. Huang, et al., Millisecond lattice gasification for high-density CO2 and O2-sieving nanopores in single-layer graphene, *Sci. Adv.* **7** (2021) eabf0116.

[45] G. He, et al., Synergistic CO2-Sieving from Polymer with Intrinsic Microporosity Masking Nanoporous Single-Layer Graphene, *Adv. Funct. Mater.* **30** (2020) 2003979.

[46] W.-C. Lee, et al., Centimeter-scale gas-sieving nanoporous single-layer graphene membrane, *J. Memb. Sci.* (2020) 118745.

[47] R. C. Rollings, A. T. Kuan, J. A. Golovchenko, Ion selectivity of graphene nanopores, *Nat. Commun.* **7** (2016) 11408.

[48] J. Buchheim, R. M. Wyss, I. Shorubalko, H. G. Park, Understanding the interaction between energetic ions and freestanding graphene towards practical 2D perforation, *Nanoscale* **8** (2016) 8345–8354.

[49] K. Celebi, et al., Ultimate Permeation Across Atomically Thin Porous Graphene, *Science* **344** (2014) 289–292.

[50] J. Zhao, et al., Etching gas-sieving nanopores in single-layer graphene with an angstrom precision for high-performance gas mixture separation, *Sci. Adv.* **5** (2019) eaav1851.

[51] S. P. Surwade, et al., Water desalination using nanoporous single-layer graphene, *Nat. Nanotechnol.* **10** (2015) 459–464.

[52] J. Bai, X. Zhong, S. Jiang, Y. Huang, X. Duan, Graphene nanomesh, *Nat. Nanotechnol.* **5** (2010) 190–194.

[53] S. P. Koenig, L. Wang, J. Pellegrino, J. S. Bunch, Selective molecular sieving through porous graphene, *Nat. Nanotechnol.* **7** (2012) 728–732.

[54] M. Rezaei, L. F. Villalobos, K.-J. Hsu, K. V. Agrawal, Demonstrating and Unraveling a Controlled Nanometer-Scale Expansion of the Vacancy Defects in Graphene by CO2, *Angew. Chemie Int. Ed.* **134** (2022).

[55] M. César, et al., Bottom-up synthesis of multifunctional nanoporous graphene, *Science* **360** (2018) 199–203.

[56] K. Choi, A. Droudian, R. M. Wyss, K.-P. Schlichting, H. G. Park, Multifunctional wafer-scale graphene membranes for fast ultrafiltration and high permeation gas separation, *Sci. Adv.* **4** (2018) eaau0476.

[57] J. Yi, D. H. Lee, W. W. Lee, W. Il Park, Direct Synthesis of Graphene Meshes and Semipermanent Electrical Doping, *J. Phys. Chem. Lett.* **4** (2013) 2099–2104.

[58] V. L. Francisco, et al., Bottom-up synthesis of graphene films hosting atom-thick molecular-sieving apertures, *Proc. Natl. Acad. Sci.* **118** (2021) e2022201118.

[59] P. R. Kidambi, et al., Facile Fabrication of Large-Area Atomically Thin Membranes by Direct Synthesis of Graphene with Nanoscale Porosity, *Adv. Mater.* **30** (2018) 1804977.

[60] G. F. Schneider, et al., DNA Translocation through Graphene Nanopores, *Nano Lett.* **10** (2010) 3163–3167.

[61] M. C. Prado, D. Jariwala, T. J. Marks, M. C. Hersam, Optimization of graphene dry etching conditions via combined microscopic and spectroscopic analysis, *Appl. Phys. Lett.* **102** (2013) 193111.

[62] A. Harpale, H. B. Chew, Hydrogen-plasma patterning of multilayer graphene: Mechanisms and modeling, *Carbon* **117** (2017) 82–91.

[63] K. Koizumi, M. Boero, Y. Shigeta, A. Oshiyama, Atom-Scale Reaction Pathways and Free-Energy Landscapes in Oxygen Plasma Etching of Graphene, *J. Phys. Chem. Lett.* **4** (2013) 1592–1596.

[64] K.-P. Schlichting, D. Poulikakos, Selective Etching of Graphene Membrane Nanopores: From Molecular Sieving to Extreme Permeance, *ACS Appl. Mater. Interfaces* **12** (2020) 36468–36477.

[65] X. Chu, L. D. Schmidt, Reactions of NO, O2, H2O, and CO2 with the basal plane of graphite, *Surf. Sci.* **268** (1992) 325–332.

[66] X. Chu, L. D. Schmidt, Intrinsic rates of nitrogen oxide (NOx)-carbon reactions, *Ind. Eng. Chem. Res.* **32** (1993) 1359–1366.

[67] H. Marsh, T. E. O'Hair, Lord Wynne-Jones, The carbon-atomic oxygen reaction—surface-oxide formation on paracrystalline carbon and graphite, *Carbon* **7** (1969) 555–566.

[68] A. Tracz, G. Wegner, J. P. Rabe, Scanning Tunneling Microscopy Study of Graphite Oxidation in Ozone−Air Mixtures, *Langmuir* **19** (2003) 6807–6812.

[69] Z. Yuan, et al., Mechanism and Prediction of Gas Permeation through Sub-Nanometer Graphene Pores: Comparison of Theory and Simulation, *ACS Nano* **11** (2017) 7974–7987.

[70] Z. Yuan, R. P. Misra, A. G. Rajan, M. S. Strano, D. Blankschtein, Analytical Prediction of Gas Permeation through Graphene Nanopores of Varying Sizes: Understanding Transitions across Multiple Transport Regimes, *ACS Nano* **13** (2019) 11809–11824.

[71] J. Schrier, Helium Separation Using Porous Graphene Membranes, *J. Phys. Chem. Lett.* **1** (2010) 2284–2287.

[72] S. Blankenburg, et al., Porous Graphene as an Atmospheric Nanofilter, *Small* **6** (2010) 2266–2271.

[73] C. Sun, et al., Mechanisms of Molecular Permeation through Nanoporous Graphene Membranes, *Langmuir* **30** (2014) 675–682.

[74] H. Liu, S. Dai, D. Jiang, Insights into CO2/N2 separation through nanoporous graphene from molecular dynamics, *Nanoscale* **5** (2013) 9984–9987.

[75] D. Jiang, V. R. Cooper, S. Dai, Porous Graphene as the Ultimate Membrane for Gas Separation, *Nano Lett.* **9** (2009) 4019–4024.

[76] L. Wang, et al., Molecular valves for controlling gas phase transport made from discrete ångström-sized pores in graphene, *Nat. Nanotechnol.* **10** (2015) 785–790.

[77] L. Wang, et al., Fundamental transport mechanisms, fabrication and potential applications of nanoporous atomically thin membranes, *Nat. Nanotechnol.* **12** (2017) 509–522.

[78] M. Bartolomei, et al., Penetration Barrier of Water through Graphynes' Pores: First-Principles Predictions and Force Field Optimization, *J. Phys. Chem. Lett.* **5** (2014) 751–755.

[79] D. Konatham, J. Yu, T. A. Ho, A. Striolo, Simulation Insights for Graphene-Based Water Desalination Membranes, *Langmuir* **29** (2013) 11884–11897.

[80] D. Cohen-Tanugi, J. C. Grossman, Water permeability of nanoporous graphene at realistic pressures for reverse osmosis desalination, *J. Chem. Phys.* **141** (2014) 74704.

[81] M. E. Suk, N. R. Aluru, Molecular and continuum hydrodynamics in graphene nanopores, *RSC Adv.* **3** (2013) 9365–9372.

[82] D. Cohen-Tanugi, J. C. Grossman, Water Desalination across Nanoporous Graphene, *Nano Lett.* **12** (2012) 3602–3608.

[83] S. Feng, Z. Xu, Edges facilitate water evaporation through nanoporous graphene, *Nanotechnology* **30** (2019) 165401.

[84] M. E. Suk, N. R. Aluru, Water Transport through Ultrathin Graphene, *J. Phys. Chem. Lett.* **1** (2010) 1590–1594.

[85] S. Lin, M. J. Buehler, Mechanics and molecular filtration performance of graphyne nanoweb membranes for selective water purification, *Nanoscale* **5** (2013) 11801–11807.

[86] C. Cheng, S. A. Iyengar, R. Karnik, Molecular size-dependent subcontinuum solvent permeation and ultrafast nanofiltration across nanoporous graphene membranes, *Nat. Nanotechnol.* **16** (2021) 989–995.

[87] Q. Shi, Z. He, K. M. Gupta, Y. Wang, R. Lu, Efficient ethanol/water separation via functionalized nanoporous graphene membranes: insights from molecular dynamics study, *J. Mater. Sci.* **52** (2017) 173–184.

[88] S. Liang, et al., Highly porous nanofiber-supported monolayer graphene membranes for ultrafast organic solvent nanofiltration, *Sci. Adv.* **7** (2022) eabg6263.

[89] L. Yanqiu, et al., Monolayer graphene membranes for molecular separation in high-temperature harsh organic solvents, *Proc. Natl. Acad. Sci.* **118** (2021) e2111360118.

[90] K. Sint, B. Wang, P. Král, Selective Ion Passage through Functionalized Graphene Nanopores, *J. Am. Chem. Soc.* **130** (2008) 16448–16449.

[91] M. E. Suk, N. R. Aluru, Ion transport in sub-5-nm graphene nanopores, *J. Chem. Phys.* **140** (2014) 84707.

[92] S. Zhao, J. Xue, W. Kang, Ion selection of charge-modified large nanopores in a graphene sheet, *J. Chem. Phys.* **139** (2013) 114702.

[93] R. Epsztein, R. M. DuChanois, C. L. Ritt, A. Noy, M. Elimelech, Towards single-species selectivity of membranes with subnanometre pores, *Nat. Nanotechnol.* **15** (2020) 426–436.

[94] A. Szymczyk, P. Fievet, Investigating transport properties of nanofiltration membranes by means of a steric, electric and dielectric exclusion model, *J. Memb. Sci.* **252** (2005) 77–88.

[95] Y. Li, Y. Yu, J. Qian, H. Wu, F. Wang, Anomalous ion transport through angstrom-scale pores: Effect of hydration shell exchange on ion mobility, *Appl. Surf. Sci.* **560** (2021) 150022.

[96] Y. Fu, et al., Dehydration-Determined Ion Selectivity of Graphene Subnanopores, *ACS Appl. Mater. Interfaces* **12** (2020) 24281–24288.

[97] S. Li, et al., Structure Evolution of Graphitic Surface upon Oxidation: Insights by Scanning Tunneling Microscopy, *JACS Au* **2** (2022) 723–730.

[98] R. M. DuChanois, et al., Designing polymeric membranes with coordination chemistry for high-precision ion separations, *Sci. Adv.* **8** (2022) eabm9436.

[99] S. Hu, et al., Transport of hydrogen isotopes through interlayer spacing in van der Waals crystals, *Nat. Nanotechnol.* **13** (2018) 468–472.

[100] S. Hu, et al., Proton transport through one-atom-thick crystals, *Nature* **516** (2014) 227–230.

[101] S. Bukola, Y. Liang, C. Korzeniewski, J. Harris, S. Creager, Selective Proton/Deuteron Transport through Nafion|Graphene|Nafion Sandwich Structures at High Current Density, *J. Am. Chem. Soc.* **140** (2018) 1743–1752.

[102] Z. Zeng, et al., Biomimetic N-Doped Graphene Membrane for Proton Exchange Membranes, *Nano Lett.* **21** (2021) 4314–4319.

[103] F. L., et al., Anomalously low dielectric constant of confined water, *Science* **360** (2018) 1339–1342.

[104] J. J. Gilijamse, A. J. Lock, H. Bakker, Dynamics of confined water molecules, *Proc. Natl. Acad. Sci.* **102** (2005) 3202–3207.

[105] S. Han, M. Y. Choi, P. Kumar, H. E. Stanley, Phase transitions in confined water nanofilms, *Nat. Phys.* **6** (2010) 685–689.

[106] S. Singh, J. Houston, F. van Swol, C. J. Brinker, Drying transition of confined water, *Nature* **442** (2006) 526.

[107] H. Hertz, Ueber die Verdunstung der Flüssigkeiten, insbesondere des Quecksilbers, im luftleeren Raume, *Ann. Phys.* **253** (1882) 177–193.

[108] A. H. Persad, C. A. Ward, Expressions for the Evaporation and Condensation Coefficients in the Hertz-Knudsen Relation, *Chem. Rev.* **116** (2016) 7727–7767.

[109] S. Sharma, P. G. Debenedetti, Evaporation rate of water in hydrophobic confinement, *Proc. Natl. Acad. Sci.* **109** (2012) 4365–4370.

[110] L. Zhao, et al., A Passive High-Temperature High-Pressure Solar Steam Generator for Medical Sterilization, *Joule* **4** (2020) 2733–2745.

[111] D. F. Hanks, et al., Nanoporous membrane device for ultra high heat flux thermal management, *Microsystems Nanoeng.* **4** (2018) 1.

[112] Y. Wang, J. Lee, J. R. Werber, M. Elimelech, Capillary-driven desalination in a synthetic mangrove, *Sci. Adv.* **6** (2020) eaax5253.

[113] A. Keerthi, et al., Water friction in nanofluidic channels made from two-dimensional crystals, *Nat. Commun.* **12** (2021) 3092.

[114] A. M. Rizzuto, E. S. Cheng, R. K. Lam, R. J. Saykally, Surprising Effects of Hydrochloric Acid on the Water Evaporation Coefficient Observed by Raman Thermometry, *J. Phys. Chem. C* **121** (2017) 4420–4425.

[115] S. Narayanan, A. G. Fedorov, Y. K. Joshi, Interfacial Transport of Evaporating Water Confined in Nanopores, *Langmuir* **27** (2011) 10666–10676.

[116] Y. Nagata, K. Usui, M. Bonn, Molecular Mechanism of Water Evaporation, *Phys. Rev. Lett.* **115** (2015) 236102.

[117] T. H. Yang, C. Pan, Molecular dynamics simulation of a thin water layer evaporation and evaporation coefficient, *Int. J. Heat Mass Transf.* **48** (2005) 3516–3526.

[118] N. Musolino, B. L. Trout, Insight into the molecular mechanism of water evaporation via the finite temperature string method, *J. Chem. Phys.* **138** (2013) 134707.

[119] P. Liu, E. Harder, B. J. Berne, Hydrogen-Bond Dynamics in the Air−Water Interface, *J. Phys. Chem. B* **109** (2005) 2949–2955.

[120] N. Yicun, G. S. M., S. J. L., Slow hydrogen-bond switching dynamics at the water surface revealed by theoretical two-dimensional sum-frequency spectroscopy, *Proc. Natl. Acad. Sci.* **110** (2013) 1992–1998.

[121] H. T. Kieu, B. Liu, H. Zhang, K. Zhou, A. W.-K. Law, Molecular dynamics study of water evaporation enhancement through a capillary graphene bilayer with tunable hydrophilicity, *Appl. Surf. Sci.* **452** (2018) 372–380.

[122] S. Sharma, P. G. Debenedetti, Free Energy Barriers to Evaporation of Water in Hydrophobic Confinement, *J. Phys. Chem. B* **116** (2012) 13282–13289.

[123] J. Fan, H. Wu, F. Wang, Evaporation-driven liquid flow through nanochannels, *Phys. Fluids.* **32** (2020) 12001.

[124] Q. Yang, et al., Capillary condensation under atomic-scale confinement, *Nature* **588** (2020) 250–253.

[125] K. Koga, G. T. Gao, H. Tanaka, X. C. Zeng, Formation of ordered ice nanotubes inside carbon nanotubes, *Nature* **412** (2001) 802–805.

[126] T. Daisuke, H. Itaru, K. Kenichiro, T. Hideki, Phase diagram of water in carbon nanotubes,

Proc. Natl. Acad. Sci. **105** (2008) 39–43.

[127] A. T. Pascal, W. A. Goddard, Y. Jung, Entropy and the driving force for the filling of carbon nanotubes with water, *Proc. Natl. Acad. Sci.* **108** (2011) 11794–11798.

[128] A. Noy, et al., Nanofluidics in carbon nanotubes, *Nano Today* **2** (2007) 22–29.

[129] J. A. Thomas, A. J. H. McGaughey, Water Flow in Carbon Nanotubes: Transition to Subcontinuum Transport, *Phys. Rev. Lett.* **102** (2009) 184502.

[130] M. Dakhchoune, et al., Rapid Gas Transport from Block-Copolymer Templated Nanoporous Carbon Films, *Ind. Eng. Chem. Res.* **60** (2021) 16100–16108.

[131] L. F. Villalobos, et al., Polybenzimidazole copolymer derived lacey carbon film for graphene transfer and contamination removal strategies for imaging graphene nanopores, *Carbon* **173** (2021) 980–988.

[132] F. H. Akhtar, et al., Highways for water molecules: Interplay between nanostructure and water vapor transport in block copolymer membranes, *J. Memb. Sci.* **572** (2019) 641–649.

[133] P. Giannozzi, et al., QUANTUM ESPRESSO: a modular and open-source software project for quantum simulations of materials, *J. Phys. Condens. Matter* **21** (2009) 395502.

[134] W. Kohn, L. J. Sham, Self-Consistent Equations Including Exchange and Correlation Effects, *Phys. Rev.* **140** (1965) A1133–A1138.

[135] P. Hohenberg, W. Kohn, Inhomogeneous Electron Gas, *Phys. Rev.* **136** (1964) B864–B871.

[136] J. P. Perdew, K. Burke, M. Ernzerhof, Generalized Gradient Approximation Made Simple, *Phys. Rev. Lett.* **77** (1996) 3865–3868.

[137] D. Vanderbilt, Soft self-consistent pseudopotentials in a generalized eigenvalue formalism, *Phys. Rev. B* **41** (1990) 7892–7895.

[138] S. Grimme, Semiempirical GGA-type density functional constructed with a long-range dispersion correction, *J. Comput. Chem.* **27** (2006) 1787–1799.

[139] C. M. Breneman, K. B. Wiberg, Determining atom-centered monopoles from molecular electrostatic potentials. The need for high sampling density in formamide conformational analysis, *J. Comput. Chem.* **11** (1990) 361–373.

[140] M. M. J. Frisch, G. W. Trucks, H. B. Schlegel, G. E. Scuseria, M. A. Robb, J. R. Cheeseman, J. A. Montgomery, Jr., T. Vreven, K. N. Kudin, J. C. Burant, J. M. Millam, S. S. Iyengar, J. Tomasi, V. Barone, B. Mennucci, M. Cossi, G. Scalmani, N. Rega, G. A. Pet, J. A. P. . W. Wong, C. Gonzalez, Gaussian 09, Revision d. 01, *Gaussian. Inc., Wallingford CT 201*. (2009).

[141] B. Hess, C. Kutzner, D. van der Spoel, E. Lindahl, GROMACS 4: Algorithms for Highly Efficient, Load-Balanced, and Scalable Molecular Simulation, *J. Chem. Theory Comput.* **4** (2008) 435–447.

[142] M. J. Abraham, et al., GROMACS: High performance molecular simulations through multi-level parallelism from laptops to supercomputers, *SoftwareX.* **1–2** (2015) 19–25.

[143] H. W. Horn, et al., Development of an improved four-site water model for biomolecular simulations: TIP4P-Ew, *J. Chem. Phys.* **120** (2004) 9665–9678.

[144] S. Miyamoto, P. A. Kollman, Settle: An analytical version of the SHAKE and RATTLE algorithm for rigid water models, *J. Comput. Chem.* **13** (1992) 952–962.

[145] W. L. Jorgensen, J. Tirado-Rives, The OPLS [optimized potentials for liquid simulations] potential functions for proteins, energy minimizations for crystals of cyclic peptides and crambin, *J. Am. Chem. Soc.* **110** (1988) 1657–1666.

[146] T. Werder, J. H. Walther, R. L. Jaffe, T. Halicioglu, P. Koumoutsakos, On the Water−Carbon Interaction for Use in Molecular Dynamics Simulations of Graphite and Carbon Nanotubes, *J. Phys. Chem. B* **107** (2003) 1345–1352.

[147] J. W. Eastwood, R. W. Hockney, D. N. Lawrence, P3M3DP—The three-dimensional periodic particle-particle/ particle-mesh program, *Comput. Phys. Commun.* **19** (1980) 215–261.

[148] A. C. Ferrari, D. M. Basko, Raman spectroscopy as a versatile tool for studying the properties of graphene, *Nat. Nanotechnol.* **8** (2013) 235–246.

[149] P. Z. Sun, et al., Limits on gas impermeability of graphene, *Nature*. **579** (2020) 229–232.

[150] H. Puliyalil, U. Cvelbar, Selective Plasma Etching of Polymeric Substrates for Advanced Applications, *Nanomaterials* **6** (2016) 108.

[151] A. S. Mayorov, et al., Micrometer-Scale Ballistic Transport in Encapsulated Graphene at Room Temperature, *Nano Lett.* **11** (2011) 2396–2399.

[152] R. Larciprete, et al., Dual Path Mechanism in the Thermal Reduction of Graphene Oxide, *J. Am. Chem. Soc.* **133** (2011) 17315–17321.

[153] R. Larciprete, P. Lacovig, S. Gardonio, A. Baraldi, S. Lizzit, Atomic Oxygen on Graphite: Chemical Characterization and Thermal Reduction, *J. Phys. Chem. C* **116** (2012) 9900–9908.

[154] A. Bagri, et al., Structural evolution during the reduction of chemically derived graphene oxide, *Nat. Chem.* **2** (2010) 581–587.

[155] T. Sun, S. Fabris, Mechanisms for Oxidative Unzipping and Cutting of Graphene, *Nano Lett.* **12** (2012) 17–21.

[156] A. F. Ismail, K. C. Khulbe, T. Matsuura, Fundamentals of Gas Permeation Through Membranes-Gas Separation Membranes: Polymeric and Inorganic, Springer International Publishing, Cham, 2015: pp. 11–35.

[157] Z. Yuan, et al., Predicting Gas Separation through Graphene Nanopore Ensembles with Realistic Pore Size Distributions, *ACS Nano*. **15** (2021) 1727–1740.

[158] Y. A. Cengel, M. A. Boles, M. Kanoğlu, Thermodynamics: an engineering approach, McGraw-hill New York, 2011.

[159] M. A. Kazemi, D. S. Nobes, J. A. W. Elliott, Experimental and Numerical Study of the Evaporation of Water at Low Pressures, *Langmuir* **33** (2017) 4578–4591.

[160] H. D. Young, R. A. Freedman, T. R. Sandin, A. L. Ford, University physics, Addison-Wesley Reading, MA, 1996.

[161] M. A. Kazemi, C. A. Ward, Contribution of thermocapillary convection to liquid evaporation, *Int. J. Heat Mass Transf.* **164** (2021) 120400.

[162] F. Duan, V. K. Badam, F. Durst, C. A. Ward, Thermocapillary transport of energy during water evaporation, *Phys. Rev. E* **72** (2005) 56303.

[163] F. Duan, C. A. Ward, Surface excess properties from energy transport measurements during water evaporation, *Phys. Rev. E* **72** (2005) 56302.

[164] C. A. Ward, F. Duan, Turbulent transition of thermocapillary flow induced by water evaporation, *Phys. Rev. E* **69** (2004) 56308.

[165] J. Winkelmann, H. Ted Davis: Statistical mechanics of phases, interfaces, and thin films, VCH publishers, New York 1996, 641–642.

[166] F. Vallejos-Burgos, F.-X. Coudert, K. Kaneko, Air separation with graphene mediated by nanowindow-rim concerted motion, *Nat. Commun.* **9** (2018) 1812.

[167] J. Julin, et al., Mass Accommodation of Water: Bridging the Gap Between Molecular Dynamics Simulations and Kinetic Condensation Models, *J. Phys. Chem. A* **117** (2013) 410–420.

[168] A. Malani, K. G. Ayappa, S. Murad, Influence of Hydrophilic Surface Specificity on the Structural Properties of Confined Water, *J. Phys. Chem. B* **113** (2009) 13825–13839.

[169] J. Martí, Analysis of the hydrogen bonding and vibrational spectra of supercritical model water by molecular dynamics simulations, *J. Chem. Phys.* **110** (1999) 6876–6886.

[170] T. A. Ho, A. Striolo, Molecular dynamics simulation of the graphene–water interface: comparing water models, *Mol. Simul.* **40** (2014) 1190–1200.

[171] A. Luzar, D. Chandler, Effect of Environment on Hydrogen Bond Dynamics in Liquid Water, *Phys. Rev. Lett.* **76** (1996) 928–931.

[172] E. Guàrdia, J. Martí, L. García-Tarrés, D. Laria, A molecular dynamics simulation study of hydrogen bonding in aqueous ionic solutions, *J. Mol. Liq.* **117** (2005) 63–67.

[173] A. Chandra, Structure and dynamics of hydrogen bonds in liquid water and aqueous solutions, *Proc. Indian Natl. Sci. Acad. Part A* **69** (2003) 49–60.

[174] S. Chowdhuri, A. Chandra, Molecular dynamics simulations of aqueous NaCl and KCl solutions: Effects of ion concentration on the single-particle, pair, and collective dynamical properties of ions and water molecules, *J. Chem. Phys.* **115** (2001) 3732–3741.

[175] J. G. Kirkwood, F. P. Buff, The Statistical Mechanical Theory of Surface Tension, *J. Chem. Phys.* **17** (1949) 338–343.

[176] M. Rajasekaran, K. G. Ayappa, Influence of the extent of hydrophobicity on water organization and dynamics on 2D graphene oxide surfaces, *Submitted*. (2022).

[177] X. Chen, et al., Ultrafast water evaporation through graphene membranes with subnanometer pores for desalination, *J. Memb. Sci.* **621** (2021) 118934.

[178] A. Siria, M.-L. Bocquet, L. Bocquet, New avenues for the large-scale harvesting of blue energy, *Nat. Rev. Chem.* **1** (2017) 91.

[179] M. E. Davis, Ordered porous materials for emerging applications, *Nature*. **417** (2002) 813–821.

[180] M. Skaug, C. Schwemmer, S. Fringes, C. D. Rawlings, A. W. Knoll, Nanofluidic rocking Brownian motors, *Science* **359** (2018) 1505–1508.

[181] X. Yahui, et al., Atomic-scale ion transistor with ultrahigh diffusivity, *Science* **372** (2021) 501–503.

[182] R. K. Joshi, et al., Precise and Ultrafast Molecular Sieving Through Graphene Oxide Membranes, *Science* **343** (2014) 752–754.

[183] S. C. O'Hern, et al., Nanofiltration across defect-sealed nanoporous monolayer graphene, *Nano Lett.* **15** (2015) 3254–3260.

[184] Y. Zhang, Y. Hu, L. Wang, W. Sun, Systematic review of lithium extraction from salt-lake brines via precipitation approaches, *Miner. Eng.* **139** (2019) 105868.

[185] A. Razmjou, M. Asadnia, E. Hosseini, A. Habibnejad Korayem, V. Chen, Design principles of ion selective nanostructured membranes for the extraction of lithium ions, *Nat. Commun.* **10** (2019) 5793.

[186] A. Kumar, H. Fukuda, T. A. Hatton, J. H. Lienhard, Lithium Recovery from Oil and Gas Produced Water: A Need for a Growing Energy Industry, *ACS Energy Lett.* **4** (2019) 1471–1474.

[187] J. D. Graham, J. A. Rupp, E. Brungard, Lithium in the Green Energy Transition: The Quest for Both Sustainability and Security, *Sustainability* **13** (2021) 11274.

[188] P. K. Choubey, M. Kim, R. R. Srivastava, J. Lee, J.-Y. Lee, Advance review on the exploitation of the prominent energy-storage element: Lithium. Part I: From mineral and brine resources, *Miner. Eng.* **89** (2016) 119–137.

[189] X. Li, et al., Membrane-based technologies for lithium recovery from water lithium resources: A review, *J. Memb. Sci.* **591** (2019) 117317.

[190] N. Nitta, F. Wu, J. T. Lee, G. Yushin, Li-ion battery materials: present and future, *Mater. Today* **18** (2015) 252–264.

[191] R. MacKinnon, Potassium Channels and the Atomic Basis of Selective Ion Conduction (Nobel Lecture), *Angew. Chemie Int. Ed.* **43** (2004) 4265–4277.

[192] W. A. Catterall, Structure and Function of Voltage-Sensitive Ion Channels, *Science* **242** (1988) 50–61.

[193] D. A. Doyle, et al., The Structure of the Potassium Channel: Molecular Basis of K+ Conduction and Selectivity, *Science* **280** (1998) 69–77.

[194] J. H. Morais-Cabral, Y. Zhou, R. MacKinnon, Energetic optimization of ion conduction rate by the K+ selectivity filter, *Nature* **414** (2001) 37–42.

[195] J. F. Cordero-Morales, et al., Molecular determinants of gating at the potassium-channel selectivity filter, *Nat. Struct. Mol. Biol.* **13** (2006) 311–318.

[196] L. Ding, et al., Effective ion sieving with Ti3C2Tx MXene membranes for production of drinking water from seawater, *Nat. Sustain.* **3** (2020) 296–302.

[197] C. E. Ren, et al., Charge- and Size-Selective Ion Sieving Through Ti3C2Tx MXene Membranes, *J. Phys. Chem. Lett.* **6** (2015) 4026–4031.

[198] J. Song, H.-W. Yu, M.-H. Ham, I. S. Kim, Tunable Ion Sieving of Graphene Membranes

through the Control of Nitrogen-Bonding Configuration, *Nano Lett.* **18** (2018) 5506–5513.

[199] Z. Zhou, et al., Flexible Ionic Conjugated Microporous Polymer Membranes for Fast and Selective Ion Transport, *Adv. Funct. Mater.* **32** (2022) 2108672.

[200] M. Abdollahzadeh, et al., Designing Angstrom-Scale Asymmetric MOF-on-MOF Cavities for High Monovalent Ion Selectivity, *Adv. Mater.* **34** (2022) 2107878.

[201] J. Meipeng, et al., Ultrathin water-stable metal-organic framework membranes for ion separation, *Sci. Adv.* **6** (2022) eaay3998.

[202] R. M. Wyss, T. Tian, K. Yazda, H. G. Park, C.-J. Shih, Macroscopic Salt Rejection through Electrostatically Gated Nanoporous Graphene, *Nano Lett.* **19** (2019) 6400–6409.

[203] Y. Yang, et al., Large-area graphene-nanomesh/carbon-nanotube hybrid membranes for ionic and molecular nanofiltration, *Science* **364** (2019) 1057–1062.

[204] I. Horcas, et al., WSXM: A software for scanning probe microscopy and a tool for nanotechnology, *Rev. Sci. Instrum.* **78** (2007) 13705.

[205] K.-J. Hsu, et al., Multipulsed Millisecond Ozone Gasification for Predictable Tuning of Nucleation and Nucleation-Decoupled Nanopore Expansion in Graphene for Carbon Capture, *ACS Nano* **15** (2021) 13230–13239.

[206] S. Huang, S. Li, K.-J. Hsu, L. F. Villalobos, K. V. Agrawal, Systematic design of millisecond gasification reactor for the incorporation of gas-sieving nanopores in single-layer graphene, *J. Memb. Sci.* **637** (2021) 119628.

[207] Y. Yu, et al., Dehydration impeding ionic conductance through two-dimensional angstrom-scale slits, *Nanoscale* **11** (2019) 8449–8457.

[208] E. R. Nightingale, Phenomenological Theory of Ion Solvation. Effective Radii of Hydrated Ions, *J. Phys. Chem.* **63** (1959) 1381–1387.

[209] X. Yang, et al., Insight into CO2 Etching Behavior for Efficiently Nanosizing Graphene, *Adv. Mater. Interfaces* **4** (2017) 1601065.

[210] D. L. Biederman, A. J. Miles, F. J. Vastola, P. L. Walker, Carbon-carbon dioxide reaction: Kinetics at low pressures and hydrogen inhibition, *Carbon* **14** (1976) 351–356.

[211] J. Zhang, et al., Large-Area Synthesis of Superclean Graphene via Selective Etching of Amorphous Carbon with Carbon Dioxide, *Angew. Chemie Int. Ed.* **58** (2019) 14446–14451.

[212] G. Zhang, M. Wen, S. Wang, J. Chen, J. Wang, Insights into thermal reduction of the oxidized graphite from the electro-oxidation processing of nuclear graphite matrix, *RSC Adv.* **8** (2018) 567–579.

[213] A. Ganguly, S. Sharma, P. Papakonstantinou, J. Hamilton, Probing the Thermal Deoxygenation of Graphene Oxide Using High-Resolution In Situ X-ray-Based Spectroscopies, *J. Phys. Chem. C* **115** (2011) 17009–17019.

[214] K. Friedel Ortega, R. Arrigo, B. Frank, R. Schlögl, A. Trunschke, Acid–Base Properties of N-Doped Carbon Nanotubes: A Combined Temperature-Programmed Desorption, X-ray Photoelectron Spectroscopy, and 2-Propanol Reaction Investigation, *Chem. Mater.* **28** (2016)

6826–6839.

[215] B. Zhao, L. Zhang, X. Wang, J. Yang, Surface functionalization of vertically-aligned carbon nanotube forests by radio-frequency Ar/O2 plasma, *Carbon* **50** (2012) 2710–2716.

[216] J. Chen, et al., Self healing of defected graphene, *Appl. Phys. Lett.* **102** (2013) 103107.

[217] K. Gopinadhan, et al., Complete steric exclusion of ions and proton transport through confined monolayer water, *Science* **363** (2019) 145–148.

[218] T. Ma, et al., Repeated Growth–Etching–Regrowth for Large-Area Defect-Free Single-Crystal Graphene by Chemical Vapor Deposition, *ACS Nano* **8** (2014) 12806–12813.

[219] M. Teng, et al., Edge-controlled growth and kinetics of single-crystal graphene domains by chemical vapor deposition, *Proc. Natl. Acad. Sci.* **110** (2013) 20386–20391.

[220] H. Wang, et al., Blue Energy Conversion from Holey-Graphene-like Membranes with a High Density of Subnanometer Pores, *Nano Lett.* **20** (2020) 8634–8639.

[221] L. Cantley, et al., Voltage gated inter-cation selective ion channels from graphene nanopores, *Nanoscale* **11** (2019) 9856–9861.

[222] J. P. Thiruraman, P. Masih Das, M. Drndić, Stochastic Ionic Transport in Single Atomic Zero-Dimensional Pores, *ACS Nano* **14** (2020) 11831–11845.

[223] S. B. Sigurdardottir, R. M. DuChanois, R. Epsztein, M. Pinelo, M. Elimelech, Energy barriers to anion transport in polyelectrolyte multilayer nanofiltration membranes: Role of intra-pore diffusion, *J. Memb. Sci.* **603** (2020) 117921.

[224] R. Epsztein, E. Shaulsky, M. Qin, M. Elimelech, Activation behavior for ion permeation in ion-exchange membranes: Role of ion dehydration in selective transport, *J. Memb. Sci.* **580** (2019) 316–326.

[225] B. Tansel, Significance of thermodynamic and physical characteristics on permeation of ions during membrane separation: Hydrated radius, hydration free energy and viscous effects, *Sep. Purif. Technol.* **86** (2012) 119–126.

[226] S. Sahu, M. Di Ventra, M. Zwolak, Dehydration as a Universal Mechanism for Ion Selectivity in Graphene and Other Atomically Thin Pores, *Nano Lett.* **17** (2017) 4719–4724.

[227] Y. Lu, L. Huang, Y. Guo, X. Yang, Theoretical insights into origin of graphene oxide acidity and relating behavior of oxygen-containing groups in water, *Carbon N. Y.* **183** (2021) 355–361.

[228] B. Konkena, S. Vasudevan, Understanding Aqueous Dispersibility of Graphene Oxide and Reduced Graphene Oxide through pKa Measurements, *J. Phys. Chem. Lett.* **3** (2012) 867–872.

[229] J. Clayden, N. Greeves, S. Warren, Organic chemistry, Oxford university press, 2012.

[230] K. H. Sippel, F. A. Quiocho, Ion–dipole interactions and their functions in proteins, *Protein Sci.* **24** (2015) 1040–1046.

[231] D. Jang, J.-C. Idrobo, T. Laoui, R. Karnik, Water and Solute Transport Governed by Tunable Pore Size Distributions in Nanoporous Graphene Membranes, *ACS Nano* **11** (2017) 10042–10052.

[232] G. He, et al., High-permeance polymer-functionalized single-layer graphene membranes that

surpass the postcombustion carbon capture target, *Energy Environ. Sci.* **12** (2019) 3305–3312.

[233] Z. Yuan, J. D. Benck, Y. Eatmon, D. Blankschtein, M. S. Strano, Stable, Temperature-Dependent Gas Mixture Permeation and Separation through Suspended Nanoporous Single-Layer Graphene Membranes, *Nano Lett.* **18** (2018) 5057–5069.

[234] S. Huang, et al., Single-layer graphene membranes by crack-free transfer for gas mixture separation, *Nat. Commun.* **9** (2018) 2632.

[235] J. Zhao, et al., Etching gas-sieving nanopores in single-layer graphene with an angstrom precision for high-performance gas mixture separation, *Sci. Adv.* **5** (2019) eaav1851.

[236] Y. Qin, et al., Ultrafast Nanofiltration through Large-Area Single-Layered Graphene Membranes, *ACS Appl. Mater. Interfaces* **9** (2017) 9239–9244.

[237] X. Lin, et al., Development of an ultra-thin film comprised of a graphene membrane and carbon nanotube vein support, *Nat. Commun.* **4** (2013) 2920.

[238] H. Du, et al., Separation of Hydrogen and Nitrogen Gases with Porous Graphene Membrane, *J. Phys. Chem. C* **115** (2011) 23261–23266.

[239] K. V. Agrawal, L. W. Drahushuk, M. S. Strano, Observation and analysis of the Coulter effect through carbon nanotube and graphene nanopores, *Philos. Trans. R. Soc. A Math. Phys. Eng. Sci.* **374** (2016).

[240] K. Celebi, et al., Atomically Thin Porous Graphene, *Science* **344** (2014) 289–293.

[241] H. Qi, et al., Fabrication of sub-nanometer pores on graphene membrane for ion selective transport, *Nanoscale* **10** (2018) 5350–5357.

[242] R. Rozada, et al., Controlled generation of atomic vacancies in chemical vapor deposited graphene by microwave oxygen plasma, *Carbon* **79** (2014) 664–669.

[243] C.-K. Lee, et al., Monatomic Chemical-Vapor-Deposited Graphene Membranes Bridge a Half-Millimeter-Scale Gap, *ACS Nano* **8** (2014) 2336–2344.

[244] P. R. Kidambi, et al., Facile Fabrication of Large-Area Atomically Thin Membranes by Direct Synthesis of Graphene with Nanoscale Porosity, *Adv. Mater.* **30** (2018) 1804977.

[245] L. Wang, C. M. Williams, M. S. H. Boutilier, P. R. Kidambi, R. Karnik, Single-Layer Graphene Membranes Withstand Ultrahigh Applied Pressure, *Nano Lett.* **17** (2017) 3081–3088.

[246] J. W. Suk, et al., Transfer of CVD-Grown Monolayer Graphene onto Arbitrary Substrates, *ACS Nano* **5** (2011) 6916–6924.

[247] A. K. Nath, Laser Drilling of Metallic and Nonmetallic Substrates, in: Compr. Mater. Process., Elsevier, Oxford, 2014: pp. 115–175.

[248] D. J. Babu, et al., Restricting Lattice Flexibility in Polycrystalline Metal–Organic Framework Membranes for Carbon Capture, *Adv. Mater.* **31** (2019) 1900855.

[249] R. S. Ruoff, J. Tersoff, D. C. Lorents, S. Subramoney, B. Chan, Radial deformation of carbon nanotubes by van der Waals forces, *Nature* **364** (1993) 514–516.

[250] I. Palaci, et al., Radial Elasticity of Multiwalled Carbon Nanotubes, *Phys. Rev. Lett.* **94** (2005) 175502.

[251] F. Fornasiero, et al., Ion exclusion by sub-2-nm carbon nanotube pores, *Proc. Natl. Acad. Sci.* **105** (2008) 17250–17255.

[252] J. K. Holt, et al., Fast Mass Transport Through Sub-2-Nanometer Carbon Nanotubes, *Science* **312** (2006) 1034–1037.

[253] L. Yu, C. Shearer, J. Shapter, Recent Development of Carbon Nanotube Transparent Conductive Films, *Chem. Rev.* **116** (2016) 13413–13453.

[254] A. Droudian, et al., Enhanced Chemical Separation by Freestanding CNT–Polyamide/Imide Nanofilm Synthesized at the Vapor–Liquid Interface, *ACS Appl. Mater. Interfaces* **10** (2018) 19305–19310.

[255] J. C. Meyer, et al., The structure of suspended graphene sheets, *Nature* **446** (2007) 60–63.

[256] Z. Yuan, J. D. Benck, Y. Eatmon, D. Blankschtein, M. S. Strano, Stable, Temperature-Dependent Gas Mixture Permeation and Separation through Suspended Nanoporous Single-Layer Graphene Membranes, *Nano Lett.* **18** (2018) 5057–5069.

[257] K. V. Agrawal, et al., Fabrication, Pressure Testing, and Nanopore Formation of Single-Layer Graphene Membranes, *J. Phys. Chem. C* **121** (2017) 14312–14321.

[258] L. G. Cançado, et al., Quantifying Defects in Graphene via Raman Spectroscopy at Different Excitation Energies, *Nano Lett.* **11** (2011) 3190–3196.

[259] A. Eckmann, et al., Probing the Nature of Defects in Graphene by Raman Spectroscopy, *Nano Lett.* **12** (2012) 3925–3930.

[260] R. Beams, L. Gustavo Cançado, L. Novotny, Raman characterization of defects and dopants in graphene, *J. Phys. Condens. Matter* **27** (2015) 83002.

[261] L. W. Drahushuk, M. S. Strano, Mechanisms of Gas Permeation through Single Layer Graphene Membranes, *Langmuir* **28** (2012) 16671–16678.

[262] R. Lv, E. Cruz-Silva, M. Terrones, Building Complex Hybrid Carbon Architectures by Covalent Interconnections: Graphene–Nanotube Hybrids and More, *ACS Nano* **8** (2014) 4061–4069.

[263] A. Saha, C. Jiang, A. A. Martí, Carbon nanotube networks on different platforms, *Carbon* **79** (2014) 1–18.

[264] Z. Lu, et al., An Ultrathin Nanoporous Membrane Evaporator, *Nano Lett.* **17** (2017) 6217–6220.

[265] Z. Lu, I. Kinefuchi, K. L. Wilke, G. Vaartstra, E. N. Wang, A unified relationship for evaporation kinetics at low Mach numbers, *Nat. Commun.* **10** (2019) 2368.

Curriculum Vitae

Wan-Chi Lee

Date of Birth: August 24th, 1993
E-mail: wan-chi.lee@epfl.ch

Education

Doctoral Student, Chemical Engineering 2018-2022
École Polytechnique Fédérale de Lausanne (EPFL), Switzerland
Advisor: Prof. Kumar Varoon Agrawal

M.S, Chemical and Bioengineering 2015-2017
Eidgenössische Technische Hochschule Zürich, (ETHZ), Switzerland

B.S., Chemical Engineering 2011-2015
National Taiwan University, Taiwan

Professional experience

Graduate Research Assistant Jan 2018- April 2018
Max-Planck Institute for Iron Research, Dusseldorf, Germany

Summer Internship June 2017- July 2017
Department of Material Engineering, University of Tokyo, Japan

Internship Feb 2016- Jun 2016
Laboratory of Food Process Engineering, ETHZ, Switzerland

Publication

1. **W. C. Lee**[†], A. Ronghe[†], L. F. Villalobos, S. Huang, M. Dakhchoune, M. Mensi, K. J. Hsu, K. G. Ayappa and K. V. Agrawal, "Enhanced water evaporation from Å-scale graphene nanopores", submitted **†equal contribution**
2. K. J. Hsu, L. F. Villalobos, S. Huang, H. Y. Chi, M. Dakhchoune, **W. C. Lee**, G. He, M. Mensi, K. V. Agrawal, "Multipulsed millisecond ozone gasification for predictable tuning of nucleation and nucleation-decoupled nanopore expansion in graphene for carbon capture", ACS Nano 15 (8)

(2021) 13230–1323

3. L.F. Villalobos, S. Huang, M. Dakhchoune, G. He, **W. C. Lee**, K.V. Agrawal, "Polybenzimidazole copolymer derived lacey carbon film for graphene transfer and contamination removal strategies for imaging graphene nanopores", Carbon, 173 (2021), pp. 980-988
4. **W. C. Lee**, L. Bondaz, S. Huang, G. He, M. Dakhchoune, K.V. Agrawal, "Centimeter-scale gas-sieving nanoporous single-layer graphene membrane", J. Membr. Sci., 618 (2021), p. 118745
5. G. He, S. Huang, L.F. Villalobos, M.T. Vahdat, M.D. Guiver, J. Zhao, **W. C. Lee**, M. Mensi, K.V. Agrawal, "Synergistic CO_2-sieving from polymer with intrinsic microporosity masking nanoporous single-layer graphene", Adv. Funct. Mater., 30 (2020), p. 2003979
6. S. Kumar, J. Jagielski, T. Tian, N. Kallikounis, **W. C. Lee**, C.J. Shih, "Mixing entropy-induced layering polydispersity enabling efficient and stable perovskite nanocrystal light-emitting diodes", ACS Energy Lett., 4 (2019), pp. 118-125
7. **W. C. Lee**, H.T. Chien, Y. Lo, H.C. Chiu, T.P. Wang, D.Y. Kang, "Synthesis of zeolitic imidazolate framework core–shell nanosheets using zinc-imidazole pseudopolymorphs", ACS Appl. Mater. Interfaces, 7 (2015), pp. 18353-18361

Conferences

1.	Oral presentation, Graphene conference, 2021	Oct. 2019 –Grenoble
2.	Poster presentation, NAMS (North American Membrane Society Meeting)	May 2020 – Online
3.	Poster presentation, SCS (Swiss Chemical Society)	Sep. 2020 – Online
4.	Poster presentation, SCS (Swiss Chemical Society)	Sep. 2019 – Zurich

Awards

1. Graduate student grant, Graphene conference (Grenoble, France), 2021
2. EPFL-Ministry of Education (MOE) Taiwan, Top 100 university scholarship, 2018
3. Student grant, research exchange program in University of Tokyo, 2017